University of Colorado, Boulder
CU Scholar

Aerospace Engineering Sciences Graduate Theses & Dissertations | Aerospace Engineering Sciences

Spring 1-1-2015

Levelset-XFEM Topology Optimization with Applications to Convective Heat Transfer

Peter B. Coffin
University of Colorado at Boulder, peter.coffin@colorado.edu

Follow this and additional works at: https://scholar.colorado.edu/asen_gradetds

Part of the Aerospace Engineering Commons, and the Mechanical Engineering Commons

Recommended Citation
Coffin, Peter B., "Levelset-XFEM Topology Optimization with Applications to Convective Heat Transfer" (2015). *Aerospace Engineering Sciences Graduate Theses & Dissertations*. 122.
https://scholar.colorado.edu/asen_gradetds/122

This Dissertation is brought to you for free and open access by Aerospace Engineering Sciences at CU Scholar. It has been accepted for inclusion in Aerospace Engineering Sciences Graduate Theses & Dissertations by an authorized administrator of CU Scholar. For more information, please contact cuscholaradmin@colorado.edu.

www.manaraa.com

Levelset-XFEM Topology Optimization with Applications to Convective Heat Transfer

by

Peter B. Coffin

B.S. Aeronautical Engineering, Clarkson University, 2009

M.S. Mechanical Engineering, Clarkson University, 2011

A thesis submitted to the

Faculty of the Graduate School of the

University of Colorado in partial fulfillment

of the requirements for the degree of

Doctor of Philosophy

Department of Aerospace Engineering Sciences

2015

www.manaraa.com

This thesis entitled:
Levelset-XFEM Topology Optimization with Applications to Convective Heat Transfer
written by Peter B. Coffin
has been approved for the Department of Aerospace Engineering Sciences

____

Prof. Kurt Maute

____

Prof. Alireza Doostan

Date ________________

The final copy of this thesis has been examined by the signatories, and we find that both the content and the form meet acceptable presentation standards of scholarly work in the above mentioned discipline.

www.manaraa.com

Coffin, Peter B. (Ph.D., Aerospace Engineering)

Levelset-XFEM Topology Optimization with Applications to Convective Heat Transfer

Thesis directed by Prof. Kurt Maute

Computational design optimization is a technique that provides designers with automated approaches to developing novel and non-intuitive optimal designs. Topology optimization is a subset of design optimization that seeks to determine the optimal geometry allowing for topologic changes during the design process. The thesis focuses on the design of devices whose performance is dominated by convective heat transfer. Convective heat transfer is a process that results from the coupling between thermal fields and fluid motion. Frequently benefitting from complicated geometries, convective design problems are an ideal case for computational design optimization. Commonly used simple engineering models of convection like Newton's Law of Cooling rely on design dependent boundary conditions that may lie along immersed design edges. These boundary conditions are difficult to represent accurately with traditional density approaches for topology optimization. In this thesis Level Set Method (LSM) and the eXtended Finite Element Methods (XFEM) are developed to handle convective design problems to ensure crisp resolution of design boundaries for accurate physical modeling. The LSM is used to provide a precise definition of geometric boundaries. Here the explicit LSM is used, which updates the parameterized Level Set Field (LSF) via Nonlinear Programming methods (NLP). The XFEM is incorporated to provide for crisp resolution of the LSM geometry within the discretization of the governing equations. With accurate resolution of simplified convection boundary conditions, complicated, potentially unphysical geometries are developed. To overcome this issue this thesis develops new regularization approaches for explicit LSMs. To enforce a minimum feature size a new measure is developed that identifies violations of the minimum feature size. To demonstrate the applicability of the LS-XFEM approach we study more complicated, coupled problems where the fluid motion is driven by buoyancy forces. The natural convection model is applied to both 2D and 3D steady-state design

المنارة للاستشارات

www.manaraa.com

problems and 2D transient problems.

www.manaraa.com

Acknowledgements

I would like to acknowledge the support of the National Science Foundation under grant EFRI-SEED 1038305 and CBET 1246854. The opinions and conclusions presented in this paper are those of the author and do not necessarily reflect the views of the sponsoring organization. I would like to thank my advisor, Professor Kurt Maute whose support and experience made this work possible.

I would also like to thank my friends who supported me through my studies, helping me maintain a healthy mind and body. I would like to thank my fellow students in Professor Maute's research group for their guidance and support during my studies. Finally, I would like to thank my family for their continued support of my education.

المنارة للاستشارات

www.manaraa.com

Contents

المنارة للاستشارات
www.manaraa.com

المنارة للاستشارات

www.manaraa.com

Figures

Figure

المنارة للاستشارات

www.manaraa.com

www.manaraa.com

Chapter 1

Introduction

With the advent of Computational Fluid Dynamics (CFD) and Finite Element Methods (FEM) in the past century, designers and engineers have been given the tools to simulate the response of mechanical systems with complex geometries. The goal of the designer is not to predict system behavior but to design those systems to produce some particular behavior. This fundamentally motivates the field of design optimization, a numerical approach to systematically manipulating design variables to yield an optimal design.

Convective heat transfer is an important factor in the design and operation of many devices, particularly modern, miniature electronics. An example heatsink is shown in Figure 1.1. Design variables for this type of geometry could include the fin thickness, fin height and number of fins. The goal of this work is to develop a computational design methodology for convective cooling and heating devices. The approach will incorporate the Level Set Method (LSM) and the eXtended Finite Element Method (XFEM) for topology optimization. These design problems yield challenges in controlling acceptable geometry, accurately computing the physical response, and accurately applying boundary conditions.

For simplified physical models the design problem is particularly prone to developing small geometric features, motivating the ability to directly control geometry feature size. Increasing physical model fidelity is another approach to discourage small, unphysical geometric features, however the approach is accompanied by additional numerical cost and complexity.

Convection is the transport of heat via fluid motion. Natural convection, where fluid motion is

المنارة للاستشارات
www.manaraa.com

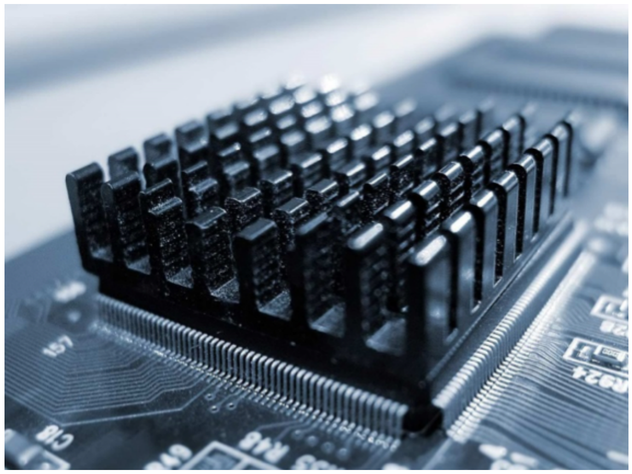

Figure 1.1: Example heatsink design.

driven by buoyancy forces, is important in enclosed, sealed or vented systems. Natural convection is also an attractive alternative to forced convection due to its robustness and simplicity (Baïri et al, 2014). Designing convective devices is challenging due to the complicated interplay of the fluid motion and temperature.

In this thesis we primarily consider design optimization tools that vary device geometry and material layout. To characterize these tools, two features should be considered: the physical model used to resolve the temperature and fluid fields and the form of geometry description. As in solid mechanics where it is necessary to specify plane-strain or plane-stress in 2D, for convection problems it is also important to note whether considering thick or thin configurations in 2D. Figure 1.2 outlines the possible geometric configurations for a solid material immersed in fluid. Thin (Figure 1.2 (b)) configurations result in convection primarily over the solid domain in 2D while thick (Figure 1.2 (c)) configurations primarily experience convection along the solid-fluid boundary in the 2D representation.

1.1 Geometry Descriptions

As this work considers optimization approaches that vary design geometry, we classify approaches based on their form of geometry description. Geometry descriptions can generally be

المنارة للاستشارات
www.manaraa.com

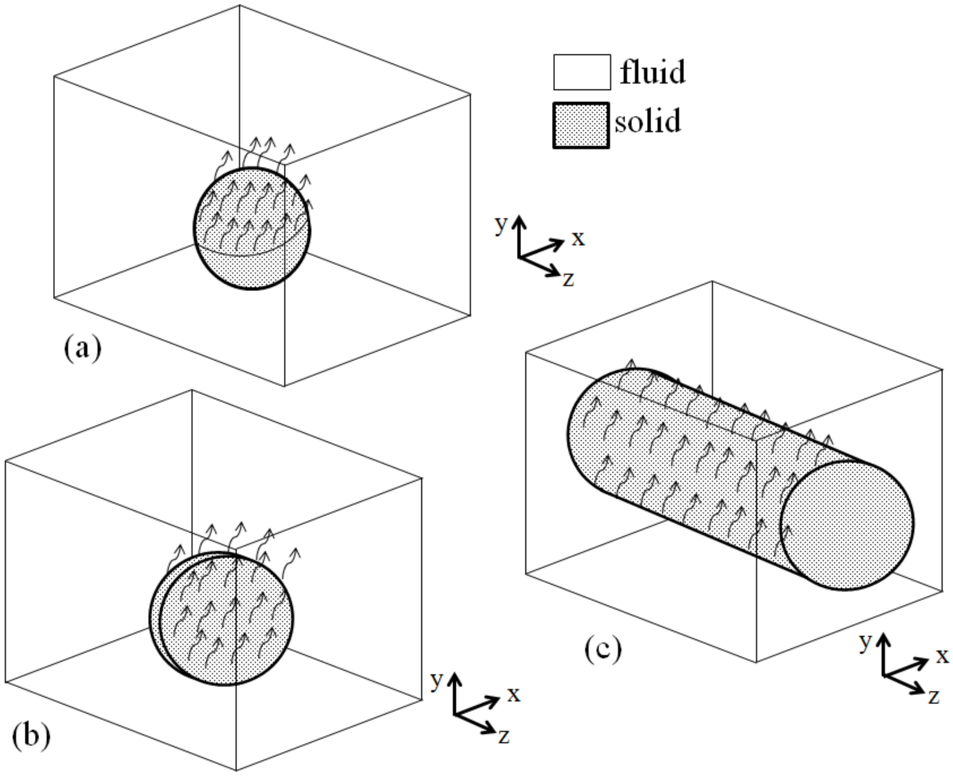

Figure 1.2: Example 3D (a), 2D thin (b) and 2D thick (c) design configurations.

classified as size, shape or topology optimization.

Size optimization relies on varying a simple set of parameters that govern the size of a geometry, such as the radius of a circle, Figure 1.3. The oldest and often simplest design tools incorporate geometry models that use only a few parameters to define the complete device geometry. For example, spacing of pins along with the thickness of pins and backplane were considered as variables in the work of Morrison (1992). Bahadur and Bar-Cohen (2005) vary pin-fin height and spacing in their model (Figure 1.4). Size optimizations benefit from simplicity but are limited by the predefined geometry. These methods are often used to fine-tune an already existing design.

Shape optimization methods define design variables that are parameters of a given shape. As in Figure 1.5, these parameters may define the positions of points that define a curve. Methods that use CAD parameterizations fall into this category (Häußler et al, 2006). These methods rely on modifying the characteristics of a geometry's boundary. The geometry variation that can be

المنارة للاستشارات
www.manaraa.com

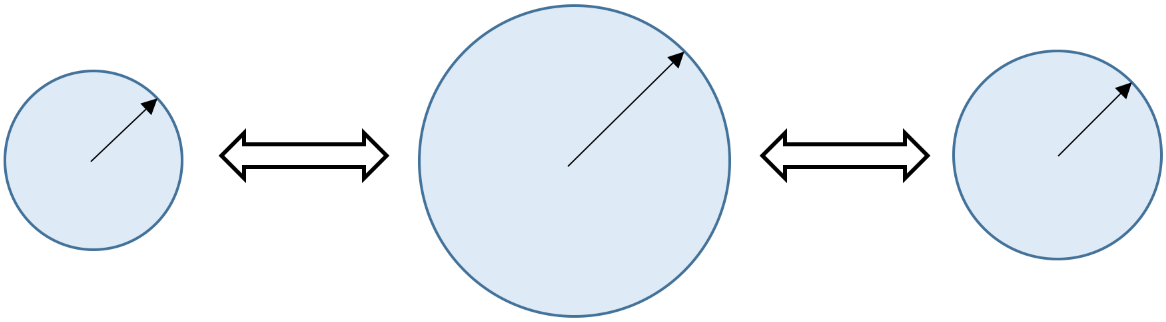

Figure 1.3: Example of size optimization, varying circle radius.

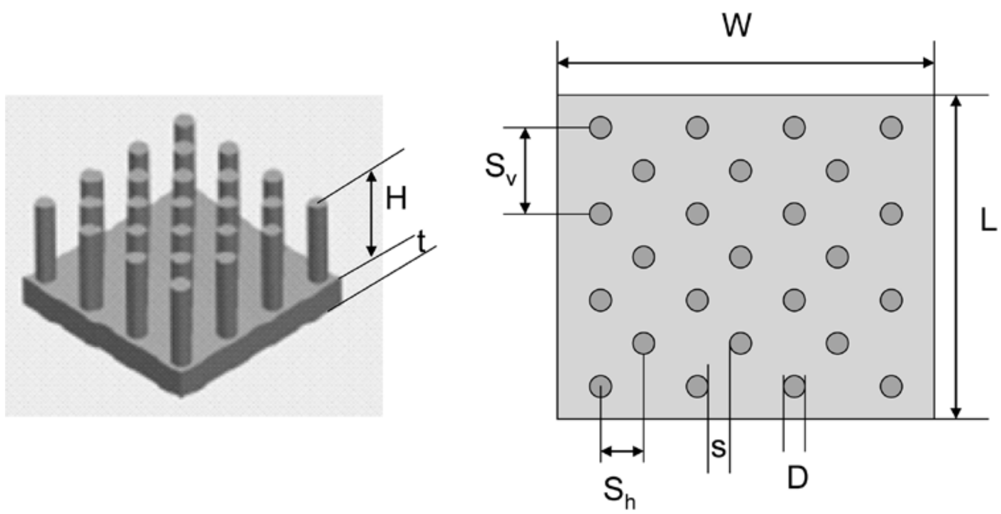

Figure 1.4: Example geometry definition of Bahadur and Bar-Cohen (2005).

achieved automatically is greater than size optimization approaches, better for finding optimal designs but more computationally expensive. It may also be difficult to ensure that the freely changing boundaries do not intersect each other or that intersections are handled in a sensible form.

Topology optimization is the most general form of geometry optimization. These methods seek to describe geometry so that any geometric changes can be made, boundaries merging or being created. Topology optimization methods can take the form of a pixel-like representation (Figure 1.6), pixel color representing the material make up of that pixel. A more detailed discussion of

www.manaraa.com

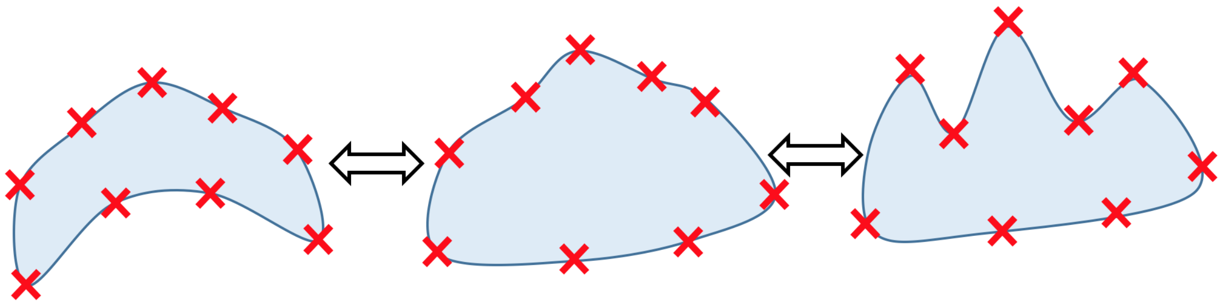

Figure 1.5: Example of shape optimization, varying point positions defining boundary.

the geometry descriptions within topology optimization is provided in Section 1.5.1. Topology optimization provides the broadest set of geometry variations for optimal designs to be chosen from. Different approaches exist to ensure that a "good" initial guess is not necessary to achieve a well-performing final design. The freedom in geometry is associated with additional complexity in predicting device behavior however. Finally, a fundamental conflict exists between the crisp representation of geometry changes and the smooth response of the system with respect to the design variables. Optimization algorithms generally perform best on smooth systems, however the underlying physics may not be smooth.

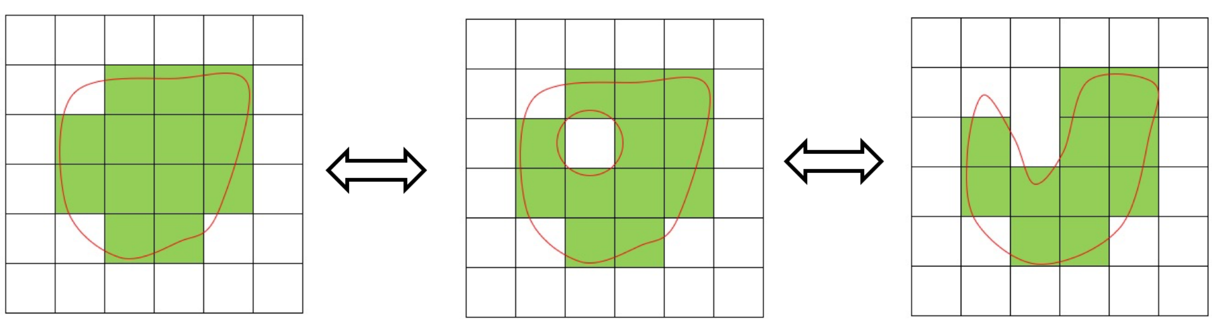

Figure 1.6: Example of topology optimization.

المنارة للاستشارات

www.manaraa.com

1.2 Objective Functions Features and Identifying Minima

Mathematically the optimization problem is written as:

$$
\begin{aligned}
&min_{\mathbf{s}} \quad Z(\mathbf{s},\mathbf{u}(\mathbf{s})) = \textstyle\int_{t_1}^{t_2} z\left(\mathbf{s},\mathbf{u}\left(t\right)\right)\ dt, \\
&\text{s.t.} \qquad g_i(\mathbf{s}) \leq 0 \quad i = 1\ldots N_g \ , \\
&\qquad\qquad \mathbf{s} \in \mathbf{S} = \left\{\mathbb{R}^{N_s} | s_i^L \leq s_i \leq s_i^U,\ i = 1....N_s\right\}\ ,
\end{aligned}
\tag{1.1}
$$

where one seeks to minimize an objective Z with respect to a set of N_s continuous variables, $\mathbf{s}$. The objective is a function of time-dependent values of the system states $\mathbf{u}$ and the design variables. The state variables are computed based on the governing equations and given the design variables, a form of coupling referred to as a Nested Analysis And Design (NAND). The problem is also subject to a set of N_g inequality constraints g_i and a set of box constraints on the design variables ($s_i^L \leq s_i \leq s_i^U$). We require that the objective $Z(\mathbf{s},\mathbf{u}(\mathbf{s}))$ its time derivative $z\left(\mathbf{s},\mathbf{u}\left(t\right)\right)$ are differentiable with respect to both the design variables $\mathbf{s}$ and state variables $\mathbf{u}$. Finally, the constraint functions $g_i(\mathbf{s})$, the state variables $\mathbf{u}$ and the governing equations should also be differentiable with respect to the design variables $\mathbf{s}$.

The convexity and continuity are important features of a problems objective function. Figure 1.7 demonstrates these features for a simple 1D function. Convex functions have one minima, the global minima, that is where:

$$
\frac{\partial Z}{\partial s} = 0.0 \ \ \frac{\partial^2 Z}{\partial^2 s} \geq 0.0, \tag{1.2}
$$

where Z representing the objective function and s the design variable. Functions that have multiple points that satisfy (1.2) are non-convex, having both local minima and a global minima. Given the function information at a single point one can only determine if the point is a local minima based on (1.2).

The first derivative information (sensitivities or gradients) is important for a number of reasons including identification of minima and identification of search directions by optimization

المنارة للاستشارات
www.manaraa.com

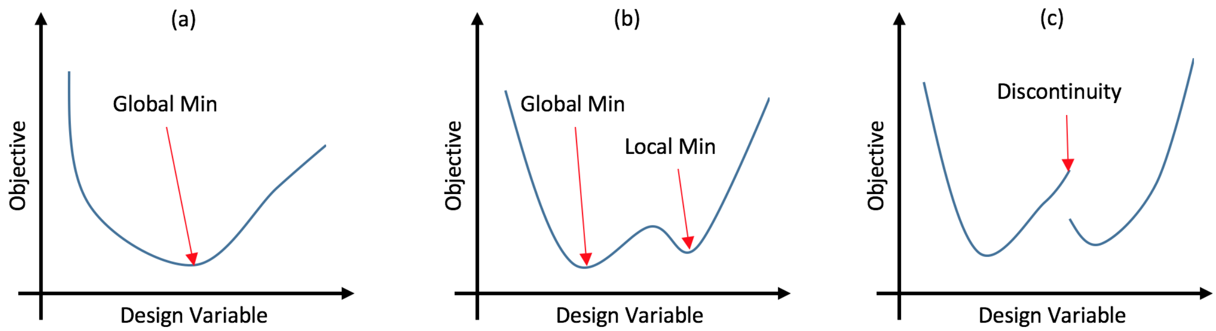

Figure 1.7: Characterization of functions: convex (a), non-convex (b), non-convex and discontinuous (c).

algorithms. Convex functions, Figure 1.7 (a), only have one minima, the global minima. Non-convex functions, Figure 1.7 (b), have multiple local minima. As objective functions become non-differentiable or discontinuous, Figure 1.7 (c), finding and identifying minima becomes difficult. For the methods discussed in this thesis, objective and constraint functions should be differentiable.

The solution to the optimization problem (1.1) can be expressed by the corresponding Lagrangian function:

$$L(\mathbf{s}, \mathbf{u}(\mathbf{s})) = Z(\mathbf{s}, \mathbf{u}(\mathbf{s})) + \sum_{i=1}^{N_g} \lambda_i \; g_i\left(\mathbf{s}\right), \tag{1.3}$$

$$\lambda_i \geq 0 \quad \forall \; i = 1, ..., N_g \;, \tag{1.4}$$

where λ_i are the Lagrange multipliers for the inequality constraints $g_i \leq 0$. The Lagrangian function formulates the constrained optimization problem (1.1) into an min-max problem. To minimize (1.1), the saddle point should be identified such that:

$$L(\mathbf{s}*, \lambda_\mathbf{i}) \leq L(\mathbf{s}*, \lambda_\mathbf{i}*) \leq L(\mathbf{s}, \lambda_\mathbf{i}*), \tag{1.5}$$

where $\mathbf{s}*$ and $\lambda_\mathbf{i}*$ are the values of the design variables and Lagrange multipliers at the saddle point. A visual depiction of the saddle point (1.5) is shown in Figure 1.8.

المنارة للاستشارات
www.manaraa.com

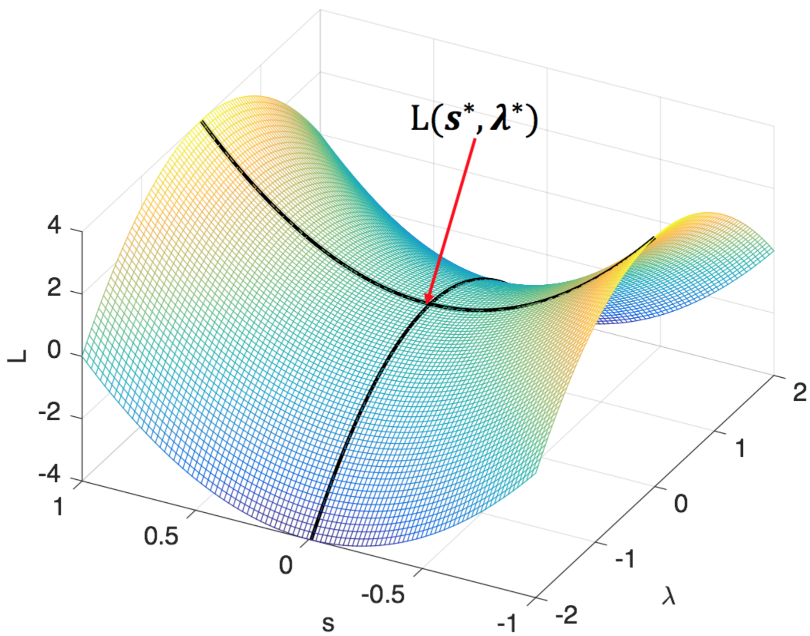

Figure 1.8: Visual representation of saddle point.

The Karush-Kuhn-Tucker (KKT) conditions are the necessary conditions for determining if a point, $\mathbf{s}*$ is an extrema for the constrained problem (1.1). The conditions, only considering inequality constraints, are (Nocedal and Wright, 2006):

$$\frac{\partial L(\mathbf{s}*, \mathbf{u}(\mathbf{s}*))}{\partial s_k} = 0, \tag{1.6}$$

$$g_i(\mathbf{s}*) \leq 0 \;\; \forall \; i = 1, ..., N_g \;, \tag{1.7}$$

$$\lambda_i * \geq 0 \;\; \forall \; i = 1, ..., N_g \;, \tag{1.8}$$

$$\lambda_i * \;\; g_i(\mathbf{s}*) = 0 \;\; \forall \; i = 1, ..., N_g \;. \tag{1.9}$$

Additionally, if the Hessian is positive definite, the KKT conditions are sufficient to identify a local

المنارة للاستشارات
www.manaraa.com

minima. That is that:

$$\mathbf{v}^T \left[\frac{\partial^2 L}{\partial s_i \, \partial s_j} \right] \mathbf{v} > 0, \tag{1.10}$$

for all non-zero $\mathbf{v}$ in $\mathbf{R}^n$. For convex problems, this point would also be a global minima.

The residual of a form of the KKT conditions can be used to identify convergence of an optimization algorithm (Fletcher and Johnson, 1997). Convergence criteria are also often formed by identifying that the design variables or optimization objective only exhibit small changes over a number of optimization iterations.

1.3 Optimization Algorithms

A variety of optimization algorithms exist from simple, like random walk and steepest descent to more complex, like the Globally Convergent Method of Moving Asymptotes (GCMMA) (Svanberg, 1995a). Optimization algorithms are also grouped by their use of gradient information. Gradient-free methods neglect gradient information and therefore do not require continuous, differentiable objective functions. Discrete problems, where design variables have a discrete set of possible values are also areas where gradient-free methods are well-suited.

Some common gradient-free algorithms are branch-and-bound methods (Land and Doig, 1960), simulated annealing (Shim and Manoochehri, 1997) and genetic algorithms (Balamurugan et al, 2008). The computational cost of these methods generally suffers when the number of design variables increases. Topology optimization problems generally require a large number of design variables (roughly equal to the number of nodes or elements) and for non-linear or transient analyses, the objective function can be quite expensive to compute. Sigmund (2011) showed that these methods quickly become impractical as meshes become finer.

Gradient-based methods address the scaling concerns of gradient-free methods, using the gradients to choose good search directions. Sigmund (2011) showed that gradient-based methods typically need an order of magnitude fewer objective evaluations as compared to gradient-free algorithms. While gradient-based methods become the only logical choice for topology optimization

المنارة للاستشارات
www.manaraa.com

methods the linearity of the problems becomes important. The more non-linear the object and constraint functions become the smaller the region for which the gradient information is a useful indicator of a "good" search direction. Depicted in [P1], Appendix A, certain physics models can lead to discontinuous response with topology change. Consider the meeting of two stiff structural features immersed in a soft material. The influence of each feature will be small until they become close. This non-linearity can hinder the optimization performance, its rate of convergence for example. Gradients also need to be computed in an efficient time. Simple finite difference approaches are not computationally efficient for a large number of design variables. Efficient calculation of sensitivities will be discussed in Section 1.4.

Interior point methods and sequential quadratic programming (SQP) are algorithms commonly used for solving nonlinear, constrained problems similar to those of topology optimization. The Method of Moving Asymptotes (MMA) (Svanberg, 1987) and Globally Convergent Method of Moving Asymptotes (GCMMA) (Svanberg, 1995b) are popular in topology optimization studies. GCMMA will be used for all problems in this thesis. Nocedal and Wright (2006) provide a more detailed discussion of the methods discussed above.

1.4 Sensitivity Analysis

The efficient calculation of sensitivities of the objective and constraint functions with respect to the design variables is an important component of a topology optimization approach. In this section the objective is used as an example, a function of both the design variables and the state variables. The calculation of the constraint function derivatives is follows the same approach.

As the objective may be a function of both the design ($\mathbf{s}$) and state ($\mathbf{u}$) variables, it is decomposed as follows:

$$\frac{dZ(\mathbf{s}, \mathbf{u}(\mathbf{s}))}{ds_i} = \frac{\partial Z}{\partial s_i} + \left(\frac{\partial Z}{\partial \mathbf{u}}\right)^T \frac{\partial \mathbf{u}}{\partial s_i}. \tag{1.11}$$

The state variables $\mathbf{u}$ are computed by solving a residual equation:

$$\mathbf{R}\left(\mathbf{s}, \mathbf{u}\left(\mathbf{s}\right)\right) = \mathbf{0}. \tag{1.12}$$

المنارة للاستشارات
www.manaraa.com

If the residual equation was well solved (equal to zero), the derivative $\partial\mathbf{u}/\partial s_i$ can be computed using:

$$\frac{\partial\mathbf{R}}{\partial s_i} = \frac{\partial\mathbf{R}}{\partial s_i} + \frac{\partial\mathbf{R}}{\partial\mathbf{u}}\frac{\partial\mathbf{u}}{\partial s_i}, \tag{1.13}$$

which, can be symbolically solved so that:

$$\frac{\partial\mathbf{u}}{\partial s_i} = -\left(\frac{\partial\mathbf{R}}{\partial\mathbf{u}}\right)^{-1}\frac{\partial\mathbf{R}}{\partial s_i}. \tag{1.14}$$

Inserting this into (1.11) results in the form:

$$\frac{dZ(\mathbf{s},\mathbf{u}(\mathbf{s}))}{ds_i} = \frac{\partial Z}{\partial s_i} - \left(\frac{\partial Z}{\partial\mathbf{u}}\right)^T\left(\frac{\partial\mathbf{R}}{\partial\mathbf{u}}\right)^{-1}\frac{\partial\mathbf{R}}{\partial s_i}. \tag{1.15}$$

This form contains the inverse of a matrix, $(\partial\mathbf{R}/\partial\mathbf{u})^{-1}$, that needs to be carefully handled to ensure efficiency. As these matrices may be large, the matrix inverse needs to be considered as a linear solve. The two methods that can be formed are the *direct method*:

$$\frac{dZ(\mathbf{s},\mathbf{u}(\mathbf{s}))}{ds_i} = \frac{\partial Z}{\partial s_i} - \left(\frac{\partial Z}{\partial\mathbf{u}}\right)^T\gamma \quad , \quad \frac{\partial\mathbf{R}}{\partial\mathbf{u}}\gamma = \frac{\partial\mathbf{R}}{\partial s_i}, \tag{1.16}$$

and *adjoint method*:

$$\frac{dZ(\mathbf{s},\mathbf{u}(\mathbf{s}))}{ds_i} = \frac{\partial Z}{\partial s_i} - \lambda^T\frac{\partial\mathbf{R}}{\partial s_i} \quad , \left(\frac{\partial Z}{\partial\mathbf{u}}\right)^T\lambda = \frac{\partial Z}{\partial\mathbf{u}}. \tag{1.17}$$

The direct method requires a number of linear solves that is equal to the number of design variables $\mathbf{s}$ while the adjoint method requires a number of solves equal to the number objective and constraint functions $(1 + N_g)$. If the number of design variables is small relative to the number of objective and constraints, the direct method is more efficient. If the number of design variables is large relative to the number of objectives and constraints, the adjoint method computationally less costly. As topology optimization problems typically have a large number of design variables, the adjoint method is generally preferred.

The calculation of time-dependent problems also requires careful consideration. The logic described above can be used, forming the time and space discretized residual equations in one large system. As the flow of information propagates forward in time, simplifications can be made so that the entire space-time system does not need to be solved at once. For more detail on this, see [P2].

المنارة للاستشارات
www.manaraa.com

1.5 Topology Optimization

This work considers topology optimization, a method where the design variables are capable of representing a generic material layout. This approach benefits from being able to pick designs from the broadest set of geometries, aiding in identification of the best performing design. The generic geometry description leads to more complexity however, typically requiring many design variables and possibly identifying geometries that are difficult to compute physical responses for.

1.5.1 Geometry Description

The oldest and most common way to describe geometry in topology optimization was developed by Bendsøe (1989) and Rozvany et al (1992). The density method describes geometry by defining material distribution in the design domain as a function of the design variables. As in Figure 1.9 a particular geometry (a) can be discretized element-by-element so that individual elements are considered as either solid or fluid (b). The density method relaxes this representation so that the material at any given point can be described as some mixture of either solid or fluid, a porous media (Figure 1.9 (c)). This variability is defined by a fictitious density, $0 \leq \rho \leq 1$, such that $\rho = 0$ represents fluid and $\rho = 1$ solid. In the simplest context the design variables may represent elemental densities, ρ. Bendsøe and Sigmund (2003), Sigmund and Maute (2013) and Deaton and Grandhi (2014) present reviews of density methods in topology optimization.

The relaxation (Figure 1.9 (c)) is an important step as it allows for smooth response of the system with respect to the design variables. This smooth response means that sensitivities of the design objectives with respect to the design variables exist and are well-formed. Without these, finding a path to an optimal solution would be much more difficult and computationally expensive.

An alternative class of methods for defining geometry is referred to as Level Set Methods (LSMs). In LSMs the material is defined by a higher order field, the level set field (LSF) ϕ, such that the boundary between materials is defined as a level set contour of the field. Often defined as

المنارة للاستشارات
www.manaraa.com

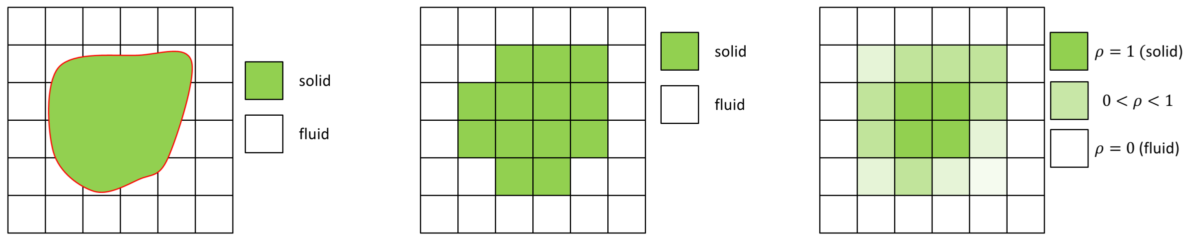

(a) Desired Geometry (b) Discretized Geometry (c) Relaxed, Discretized Geometry

Figure 1.9: Density approach to discretizing and relaxing geometry discription.

the zero-contour this is written as:

$$\begin{aligned} \phi(\mathbf{x}) &< 0, \quad \forall\ \mathbf{x} \in \Omega_S, \\ \phi(\mathbf{x}) &> 0, \quad \forall\ \mathbf{x} \in \Omega_F, \\ \phi(\mathbf{x}) &= 0, \quad \forall\ \mathbf{x} \in \Gamma_{FS}, \end{aligned} \tag{1.18}$$

where Ω_S is the domain of solid material, Ω_F the fluid domain and Γ_{FS} the boundary between the two. This concept is shown in Figure 1.10 where a geometry (a) can be described by a the field shown in (b). It is important to note that a particular geometry can be represented by an infinite number of LSFs, the description is not unique. This characteristic leads to a general need for regularization to retain well-behaved LSFs. A recent review of LSMs is provided by van Dijk et al (2013).

A bulk of LSMs, such as the work of Allaire et al (2004), can be referred to as implicit LSMs. These methods update the level set field by solving a Hamilton-Jacobi type equation where interface velocities are defined as functions of the design objective's shape sensitivity. This approach combines the LSM and optimization algorithm into one method. In this thesis an explicit LSM is used. As studied by Wang and Wang (2006), Luo et al (2007) and Pingen et al (2010) explicit methods simply prescribe the level set field as a parameterized function of design variables, computing design objective sensitivities with respect to the level set field parameters. The resulting problem is solved using a nonlinear programming (NLP) method. The optimization algorithm and the analysis (LS-

المنارة للاستشارات
www.manaraa.com

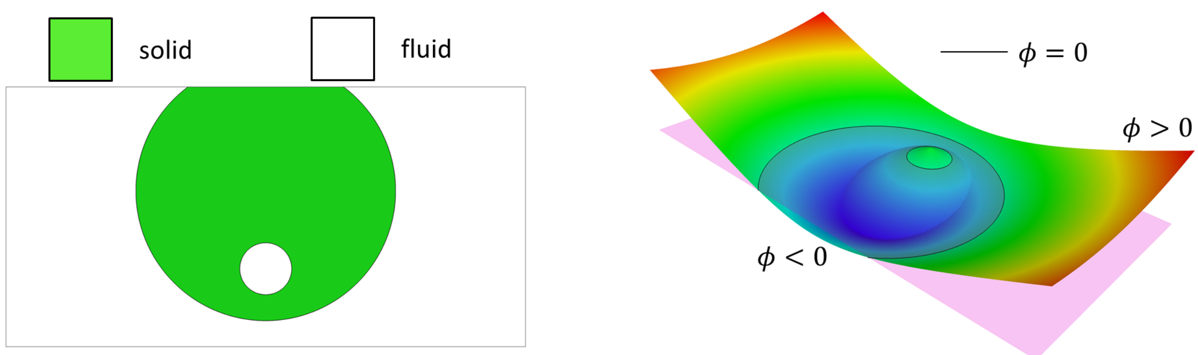

(a) Desired Geometry

(b) Example Levelset field

Figure 1.10: Approach to representing geometry with levelset field.

www.manaraa.com

XFEM) retain their separate functions. In explicit methods the level set field is often parameterized by radial basis functions or as used here, standard finite element interpolation functions.

1.5.2 Physics Model Discretization

How the solution of the physics' governing equations is coupled to the geometry definition is critical to understanding a topology optimization method. In the context of this work, finite element methods are used to discretize and solve the governing equations. Other methods may be used as exemplified by Marck et al (2013), who have studied forced convection problems using the finite volume method.

Density methods typically couple the geometry model to the finite element method by defining the material properties as explicit functions of the fictitious material density. For example, in structural mechanics the elastic modulus E can be defined as a product of the density and the actual modulus E_0 such that $E = \rho^p E_0$, where p is a penalization parameter. This will result in void material where $\rho = 0$ having a vanishing stiffness and a solid material where $\rho = 1$ having a stiffness such that $E = E_0$.

For fluid mechanics an extra term (Brinkmann penalization) is commonly added to the Navier-Stokes equation to penalize non-zero fluid velocities in solid material (Borrvall and Petersson, 2003). The parameter of this term is interpolated from the fictitious density. The approach can be viewed as considering the fluid domain as a porous material with varying porosity.

An often cited downside to density methods is difficulty with non-physical behavior, such as pressure diffusion through solid (Kreissl and Maute, 2012). Well behavedness of these methods is related to the proper choice of interpolation rules for material properties so that intermediate material is discouraged. This choice can become difficult as more coupled physics are considered (Alexandersen et al, 2014).

LSMs often use a similar approach to incorporate the geometry. Ersatz material methods treat elements that do not contain a zero iso-contour as either solid or fluid using traditional finite elements. Intersected elements (containing an iso-contour) are treated as intermediate materials

المنارة للاستشارات
www.manaraa.com

with fictitious densities based on the fluid-solid volume fraction of the element or point-wise level set field values. Smoothed Heaviside functions are often features of these methods, effectively turning on and off parts of the governing equations in certain regions. As these methods still rely on similar relaxations as do density methods, ersatz material methods can suffer from smeared interface phenomena (van Dijk et al, 2013).

In this work the eXtended Finite Element Method (XFEM) is used to incorporate the level set geometry. The XFEM allows for the crispness of the level set geometry to be retained and relies on the decomposition of intersected elements into their respective fluid and solid components. An introduction to the XFEM is provided by Fries and Belytschko (2006) and Khoei (2015).

The XFEM is composed of three parts: interpolation function enrichment, element decomposition for integration, and boundary condition enforcement. Interpolation function enrichment is the process of adding or modifying interpolation functions and corresponding degrees of freedom in intersected elements. The purpose of this enrichment is to allow the element's interpolation to represent discontinuities in the field or it's spatial derivative on boundaries that lie within an element, Figure 1.11. These discontinuities are critical to accurately representing the field near material interfaces that lie within elements.

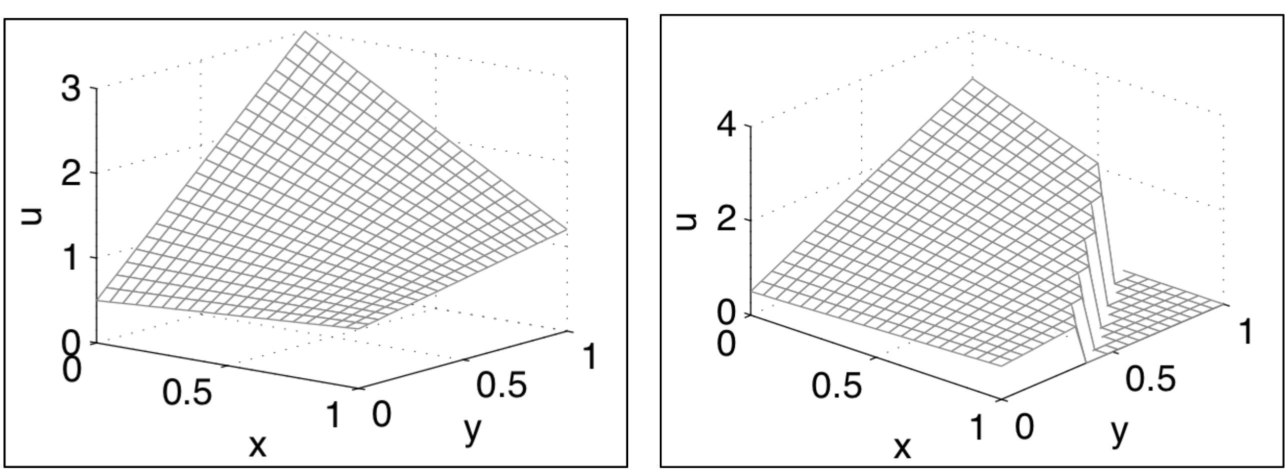

(a) Normal Finite Element (Continuous Field) (b) XFEM Element (Mid-Element Discontinuity)

Figure 1.11: Impact of interpolation function enrichment in XFEM elements.

www.manaraa.com

Element integration is also modified such that sets of numeric integration points are identified in the portions of the element corresponding to each material phase. In this work intersected elements are decomposed into triangles (2D) or tetrahedra (3D) where triangle or tetrahedra faces fall along the immersed material interface. Each triangle or tetrahedra is then identified as being in a particular material phase and the standard Gauss integration points for that subdomain are used to integrate it, Figure 1.12. Integration points are also defined on triangle edges or tetrahedra faces that lie along the immersed material interface for integration of that interface.

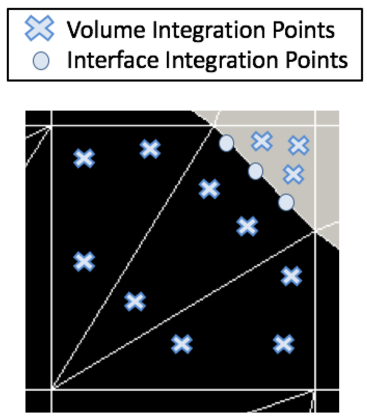

Figure 1.12: Example decomposition of 2D, intersected element for integration; showing both volume ($d\Omega$) and interface ($d\Gamma$) integration points.

A variety of boundary conditions may need to be enforced including: no-slip fluid, simplified convection, or pressure loads. Due to the more complicated relationship between nodal degrees of freedom and the interfaces upon which boundary conditions should be applied, strong enforcement is not used. Weak methods such as Nitsche's or Lagrange Multipliers are used. These techniques are also commonly used in Discontinuous Galerkin methods. A more detailed description the XFEM used in this work can be found in [P1] (Appendix A) and [P2] (Appendix B).

المنارة للاستشارات
www.manaraa.com

1.6 Physical Models

In this thesis two levels of fidelity are considered in modeling convective heat transfer. A simplified model (1.6.1) is studied in [P1] while the more advanced model (1.6.2) is studied in [P2].

1.6.1 Simplified Convection

A common engineering method is to lump convective heat fluxes into a simple temperature-dependent boundary condition, Newton's Law of Cooling (NLC), and only compute the temperature field in the solid material. The temperature field in the solid material is governed by the diffusion equation. Here isotropic materials are considered in steady-state such that:

$$\kappa \frac{\partial^2 T_S}{\partial x_i \partial x_i} + q = 0, \tag{1.19}$$

where the solid temperature T_S is governed by the conductivity κ and the applied flux q. The convective flux is written as:

$$q_c = h \; dA \; (T_S - T_\infty), \tag{1.20}$$

where the convective flux q_c is a product of the convection coefficient h, the infinitesimal surface area dA, the solid surface temperature T_S and the far-field fluid temperature T_∞. In this model the convection coefficient h needs to be estimated given the interface geometry, fluid motion, temperature and material properties (Cengel et al, 1998). In this thesis the convection coefficient is considered to be constant, a source of error in the model as the optimization will necessarily result in changing design geometry. Increasing fidelity in the estimation of the convection coefficient conflicts with the purpose of this model, it being computationally inexpensive.

Incorporation of this convection model for thin 2D problems is a relatively simple task for both density and LSMs and has been studied by Yin and Ananthasuresh (2002), Bruns (2007), Seo (2009), and Alexandersen (2011). Modeling thick 2D NLC convection is more difficult, requiring the incorporation of convective fluxes at the immersed fluid-solid interface in 2D. Density methods do

المنارة للاستشارات
www.manaraa.com

not explicitly define this boundary so it must be reconstructed based on characteristic density values or density gradients. Yin and Ananthasuresh (2002), Moon et al (2004), Yoon and Kim (2005), Iga et al (2009) and Alexandersen (2011) all incorporate NLC convection into density methods for thick 2D design problems. 3D problems require a similar approach as the convective surface is also an immersed material interface within the design domain. An ersatz material method for an LSM can also use a similar technique as shown in Yamada et al (2011).

Due to the decomposition of the design domain in the LS-XFEM as used in this thesis, integration can be directly performed along the fluid-solid interface. In this context the modeling of thick 2D NLC convection problems becomes a relatively straight-forward process. The relative accuracy of selected density, material interpolation and LS-XFEM approaches for thick NLC problems is studied in [P1] (Appendix A).

1.6.2 Natural Convection

To increase fidelity, a model of fluid motion and its heat transport are considered. The heat transport in both the fluid and the solid material is governed by the advection diffusion equation:

$$\rho c_p \left(\frac{\partial T}{\partial t} + u_i \frac{\partial T}{\partial x_i} \right) = \kappa \frac{\partial^2 T}{\partial x_i \partial x_i} + q. \tag{1.21}$$

An isotropic material with conductivity κ is again considered. The material density is ρ, the heat capacity c_p, the time t and material velocity u. For solid materials the velocity is prescribed to be zero. In the fluid material the velocity is described by the solution to the incompressible Navier-Stokes equations. The momentum equation is written as:

$$\rho \left(\frac{\partial u_i}{\partial t} + u_j \frac{\partial u_i}{\partial x_j} \right) = \frac{\partial \sigma_{ij}}{\partial x_j} + f_i^B, \tag{1.22}$$

where the fluid stress is written as:

$$\sigma_{ij} = -p\delta_{ij} + \mu \left(\frac{\partial u_i}{\partial x_j} + \frac{\partial u_j}{\partial x_i} \right), \tag{1.23}$$

www.manaraa.com

where μ is the dynamic viscosity, δ_{ij} the Kronecker delta function and p is the pressure. The incompressibility condition is written as:

$$\frac{\partial v_i}{\partial x_i} = 0. \tag{1.24}$$

The Boussinesq approximation is incorporated by defining the body force as:

$$f_i^B = -\rho g_i \alpha \left(T_F - T_0 \right), \tag{1.25}$$

where g_i is the gravitational acceleration vector, α the coefficient of thermal expansion, T_F the fluid temperature and T_0 the zero-expansion temperature. Forced convection models would ignore the buoyancy forces, that is: $f_i^B = 0.0$, resulting in a one way coupling.

A number of works have studied forced convection design problems, for example, Yoon (2010), Lee (2012), McConnell and Pingen (2012), Matsumori et al (2013), Kontoleontos et al (2013) and Koga et al (2013). LSMs have seen less focus for these problems, being studied by Marck et al (2013), Makhija and Maute (2015) and Yaji et al (2015). Makhija and Maute (2015) differ from the Navier-Stokes model presented here, using instead a Boltzman fluid model.

Topology optimization of natural convection systems is in its infancy. The two-way coupling of the fluid motion and thermal fields can lead to those fields exhibiting complicated behavior. As applied heat and temperature differences increase so will fluid velocities, leading to dynamic instabilities. Alexandersen et al (2014) and Alexandersen (2015) have been the sole examples of topology optimization of natural convection systems. These works utilize density methods to study 2D and 3D problems assuming steady-state flow solutions. The authors found convergence of the flow solution difficult, potentially indicating that transient flow behavior should be modeled. Additionally, for a micro-pump design problem the penalization of intermediate material was ineffective.

In [P2] (Appendix B) this thesis considers a natural convection design problem utilizing an explicit LS-XFEM. The goals of this work are to perform optimization of geometries in both 2D and 3D domains and to consider transient effects using LS-XFEM. Considering the models used here, this work is limited to low Mach and Reynolds numbers.

المنارة للاستشارات
www.manaraa.com

1.7 Regularization and Feature Size Control

LSFs are not a unique representation of a particular geometry. Implicit methods that propagate the field with the Hamilton-Jacobi equation often require reinitialization of the field periodically through the optimization process. Explicit methods do not perform this step and leave the propagation of the field to the optimization algorithm. To retain a well-formed LSF, regularization approaches are typically necessary (van Dijk et al, 2013). A number of measures are used to regularize explicit LSMs such as perimeter and measures of the LSF gradient (van Dijk et al, 2013).

Control of a geometry's minimum feature size is another useful form of regularization. It is useful to control feature size for two reasons, to ensure manufacturability and to ensure accurate representation on the chosen discretization. Design for manufacturability is a common concern due to the formation of thin, complicated geometries in structural optimizations (Sigmund, 2009). The representation of the discretized shape resulting from an LSF suffers from artifacts as a result of limitations in the element interpolation (Jenkins and Maute, 2015). In [P1] it was found that due to the shape-sensitivities of the LS-XFEM and the problem physics that some form of feature size control was necessary to ensure convergence to a design.

Feature size has been considered in density method topology optimization in a variety of contexts, including: manufacturing processes (Zhou et al, 2014), projection schemes (Guest et al, 2004), local density variation (Poulsen, 2003), robust design formulations (Schevenels et al, 2011), medial surface reconstruction (Zhang et al, 2014) and three-field-schemes (Zhou et al, 2015). A variety of approaches have also been demonstrated for LSMs. Guo et al (2014), Xia and Shi (2015), Allaire et al (2014) and Liu et al (2015) utilize the sign-distance or nearly-sign-distance form of the LSF to identify feature size. The use of these methods for explicit LSMs would require the reconstruction of such a field at every optimization iteration, something that is considered overly expensive. Chen et al (2008) and Luo et al (2008) compute a quadratic energy function of the geometry using the level set interface. These methods function in the context of explicit LSMs, however their construction makes their response unintuitive. Application to a general set of

www.manaraa.com

problems appears difficult with these methods.

To alleviate the issues discussed previously, the need for a sign-distance-like LSF and an unintuitive response motivated the work to develop a more general, straight forward measure, [M1]. The measure is demonstrated for both heat transfer and solid mechanics design problems in 2D. 3D implementation is only limited by the need to compute closest, tangent distances between points along a discretized surface.

1.8 Contributions

A summary of the novel contributions of this thesis:

- **Application of LS-XFEM topology optimization to simplified convection models.** Applying LS-XFEM to simplified convection was shown in this work ([P1]) to offer substantial gains in accuracy over a sample of existing methods for thick 2D problems. A survey of a broader set of design parameters also provided deeper insight into the behavior of the design problem than previous works.

- **Application of LS-XFEM topology optimization to natural convection models.** The challenges with the application of the LS-XFEM to natural convection problems were explored ([P2]). These challenges include the development of thin solid features and robust enforcement of boundary conditions on immersed interfaces.

- **Optimization of natural convection systems considering transient behavior.** In [P2] transient behavior was considered for a 2D design problem, something not demonstrated in other works.

- **Development of LSF gradient-based measure.** In [P1] a new, simple, LSF gradient-based measure was developed and demonstrated that was able to control sub-element size geometric features.

- **Development of general feature size identification measure.** In [M1] a measure

المنارة للاستشارات
www.manaraa.com

was developed to identify features smaller than a prescribed value. The measure is only a function of the discretized XFEM material interface, ensuring geometric consistency between the analysis for the physical system response and feature size identification. It is demonstrated on a selection of problems in 2D and the influence of its parameters are explored.

www.manaraa.com

Chapter 2

Summary of Publications and Manuscripts

This chapter gives a summary of the peer reviewed articles resulting from this dissertation ([P1],[P2]) and manuscript prepared for submission ([M1]). These papers and manuscripts are included in the appendix of this document.

This work begins ([P1]) with a study of LS-XFEM applied to simplified convection models, showcasing the accuracy advantages of LS-XFEM and demonstrated a need for regularization beyond perimeter and volume control. [P2] applies LS-XFEM to a more detailed convection model, studying the influence of the physical model on designs and also performing optimization on a problem with transient flow behavior. [M1] addresses a recurring need for a general feature size control in the context of explicit LSMs

2.1 [P1]: Level Set Topology Optimization of Cooling and Heating Devices using a Simplified Convection Model

This paper outlines a novel application of LS-XFEM topology optimization to design problems utilizing a simplified convection model. The LS-XFEM is shown to produce an accurate representation of the simplified convection boundary condition, converging with mesh refinement to the same characteristic value as a traditional body-fitted finite element method. This is compared to two examples of existing material interpolation approaches. The existing methods converge to values far from that of the body-fitted finite element method, Figure 2.1. The LS-XFEM is then demonstrated on both 2D and 3D convection design problems for both topology optimization and

المنارة للاستشارات
www.manaraa.com

parameter optimization with geometric primitives. The form of the geometric primitives allows for petal-like shapes around a semi-circular base of variable radius. The correlation of resulting designs with each geometry discretization reinforces insights into the behavior of the design problem.

With application to design problems it is shown that regularization is necessary to prevent non-physical designs and ensure convergence to an optimal design. For low Biot numbers, thin features develop both in the fluid and solid domains. The development of the thin solid features is problematic as their construction and the breaking of them leads the designs to not converge. Features grow, become thinly connected to the primary body, disconnect and are removed, at which point new features begin to grow.

A novel, regularization measure is demonstrated based on the level set field gradient that is able to deter sub-element size features. This measure is not mesh independent however, motivating the future development of a mesh-independent regularization based on feature size. The development of this measure is presented in [M1], Appendix C. The development of non-physical geometric features is fundamentally a result of the overly simple convection model. The influence of additional model fidelity by modeling motion and thermal fields in the fluid is explored in [P2], Appendix B.

2.2 [P2]: A Level-set Method for Steady-State and Transient Natural Convection Problems

This paper attempts to resolve the non-physical feature development exhibited in [P1] by increasing the fidelity of the convection model. In this work natural convection systems are considered. The thermal field is governed by the advection-diffusion equation while the fluid motion is governed by the incompressible Navier-Stokes equations with the Boussinesq approximation. The LS-XFEM is used to approximate the physical model.

The natural convection model is demonstrated for both 2D and 3D steady-state and 2D transient design problems. For 2D steady-state problems a geometric primitive geometry discretization was demonstrated in addition to the topology optimization discretization. The increased model

المنارة للاستشارات
www.manaraa.com

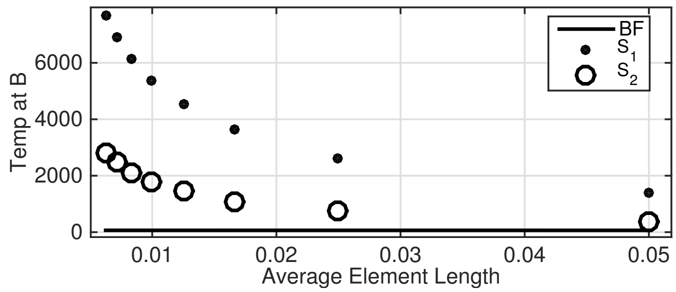

(a) SIMP mesh convergence

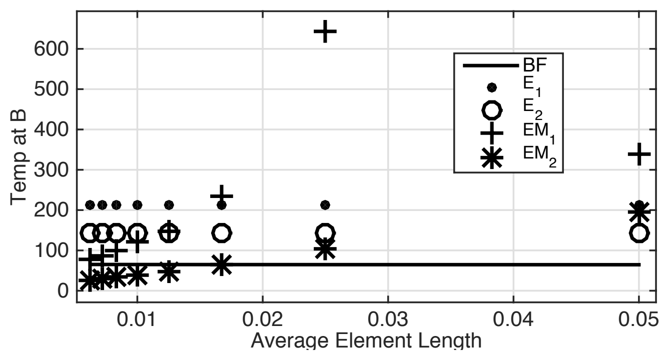

(b) Ersatz material mesh convergence

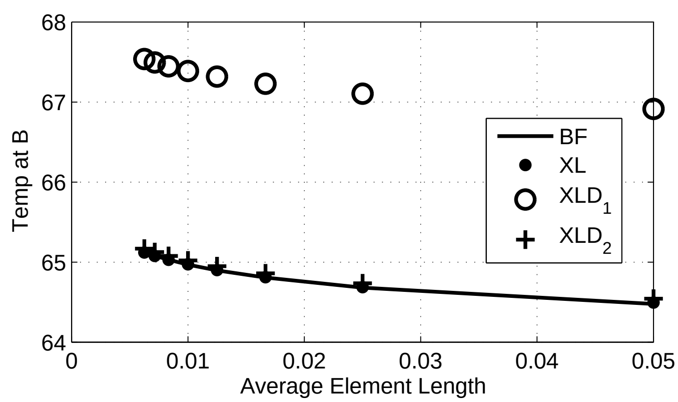

(c) XFEM mesh convergence

Figure 2.1: Convergence of topology optimization methods for simplified convection. XFEM approaches showing significantly closer agreement to reference body-fitted FEM.

fidelity is shown to alleviate the development of non-physical, thin fluid features. Thin features do continue to develop in the solid material phase however, necessitating the use of the LSF gradient-based measure developed in [P1]. For low Rayleigh and Grashof numbers, which indicate low flow

www.manaraa.com

velocities, symmetric flow solutions were unstable for certain shapes. Asymmetric designs were found to be beneficial to the performance of the design, Figure 2.2. These results were exhibited in both the geometric primitive and topology optimization discretizations. The sequential time solution approach used in the transient analysis led to substantial computation time, motivating the incorporation of more advanced time discretization methods.

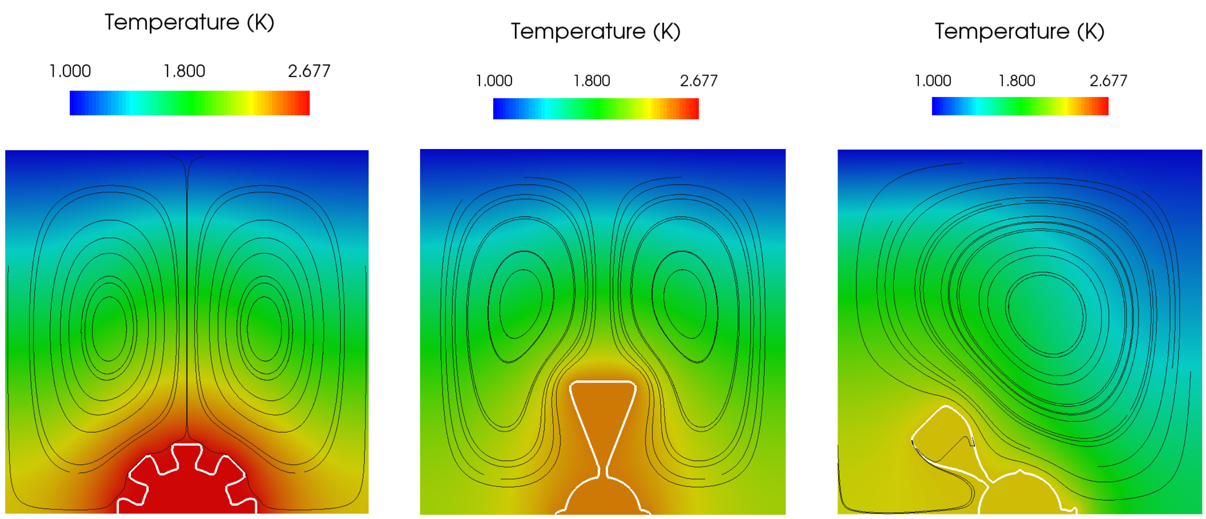

Figure 2.2: Designs resulting from 2D steady-state natural convection design problem using constant petal parameters (a), symmetric petal parameters (b) or free petal parameters (c).

2.3 [M1]: A Measure for Feature Size Control in Explicit Level Set eXtended Finite Element Method Topology Optimization

This manuscript presents the development of a minimum feature-size measure for the regularization of explicit LS-XFEMs. The measure is developed to identify violations of a minimum feature-size in either a single or both material phases. It is a function only of the discretized XFEM surface geometry, minimizing differences between the regularized geometry and that which the physical model is being analyzed upon. The form of the measure is a double integral over the material interface. The integral is a product of Heaviside functions that consider the Euclidean distance between integration points and the relative value of tangent to Euclidean distance. The

www.manaraa.com

measure is demonstrated for two design problems: the MBB beam of Sigmund (2009) and the convective design of [P1].

For strict enforcement of a minimum feature size, which limits topology change, an inequality constraint is used. To enforce a minimum feature size that is substantially different than the initial design's minimum feature size, a continuation approach is necessary, Figure 2.3. In the continuation approach the feature size measure is incorporated as a penalty on the objective. After applying a sequence of larger feature sizes via penalty, the approach switches to a strict constraint on the violation of the feature size measure for the final stage.

The influence of a tuning parameter r_{tx} in the measure is also demonstrated on the convective design problem, the parameter influencing the surface roughness of the design geometry, Figure 2.4. The measure is shown to be an effective approach to limiting feature size for LS-XFEMs in 2D. The measure is not demonstrated in 3D but the extension should require little additional work and is left for future study.

www.manaraa.com

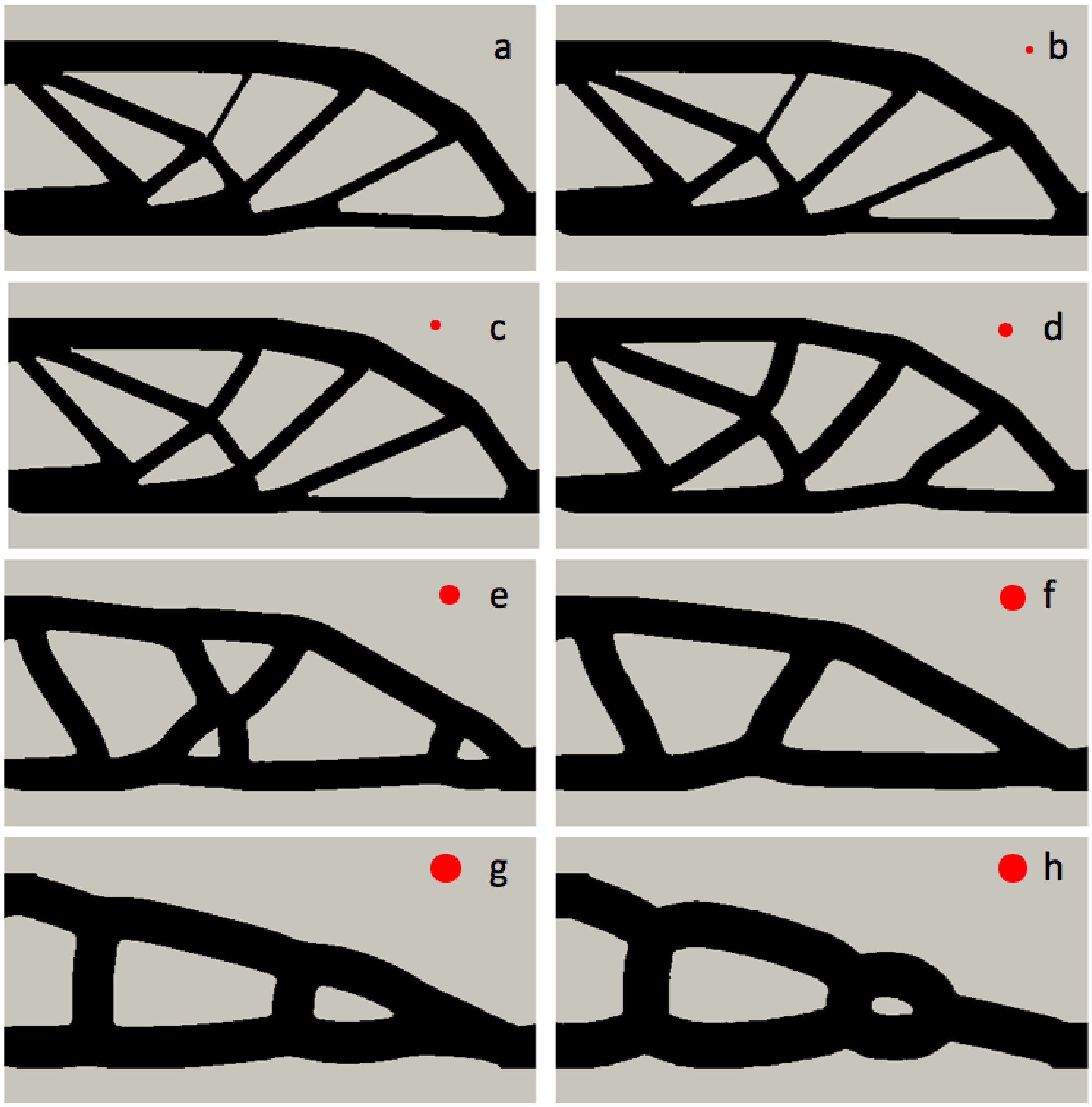

Figure 2.3: MBB beam designs resulting from the application of feature size control through a continuation approach, initial stage (a), final stage (h). Prescribed feature size shown with red circle.

المنارة للاستشارات
www.manaraa.com

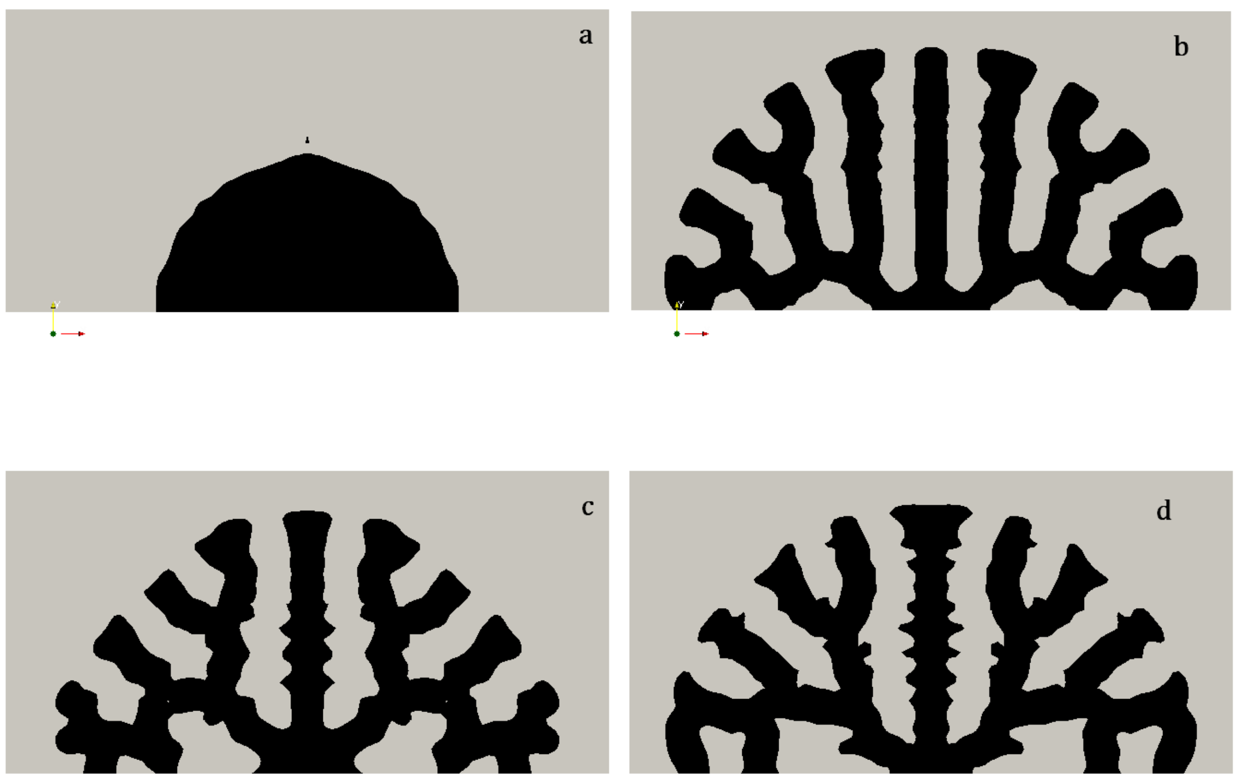

Figure 2.4: Convective device designs resulting from variation in feature size parameter r_{tx}, from smallest (a) to largest (b).

www.manaraa.com

Chapter 3

Conclusions

3.1 Concluding Remarks

This thesis primarily aimed to study convective design problems using the Level Set (LS) eXtended Finite Element Method (XFEM). Both simplified ([P1]) and more advanced ([P2]) models of convection were incorporated. The application of LS-XFEM to simplified convection models was shown to result in an approach that accurately computed the system states when referencing traditional body-fitted finite element methods and comparing against existing material interpolation methods. For particular problem parameters (low Biot number), the simplified convection model drives towards geometries that are unphysical in their development of very thin fluid channels. In ([P1]) a simple level set field (LSF) gradient-based measure was developed and demonstrated to deter sub-element size features. A more advanced, mesh independent measure of minimum feature size was motivated and then developed and studied in ([M1]). This measure was demonstrated in 2D for a selection of design problems, illustrating important considerations for its application. In ([P2]) the natural convection model governed by the advection-diffusion and incompressible Navier-Stokes equations was studied for steady-state 2D and 3D and transient 2D problems. The model was limited in this work to low Mach and Reynolds numbers. The more advanced model was shown to alleviate the development of unphysical, thin fluid channels but not the development of thin solid material features. Thin, solid material features necessitated the use of the LSF gradient-based measure of ([P1]).

The LS-XFEM is a promising approach for convective heat transfer problems, alleviating

المنارة للاستشارات
www.manaraa.com

accuracy and robustness issues due to intermediate density materials. The method was shown to be particularly adept at providing accurate state solutions in problems where Neumann-like, design dependent boundary conditions are applied on the immersed material interfaces, as in thick, simplified convection models. The application of Dirichlet-like boundary conditions on immersed material interfaces for non-linear physical models (Navier-Stokes) was found to require more care. Current approaches need further study, particularly in 3D to understand the relationship between the solution robustness (with respect to geometry changes) and accuracy. Regularization of the explicit LS-XFEM was addressed with two measures: one, LSF gradient-based measure that can deter sub-element-size features with careful application and two, a mesh-independent, identification of minimum feature size violation, demonstrated on multiple design problems in 2D.

The work in this study has significantly broadened the understanding of the application of topology optimization to convective design problems. Further study is still necessary to confidently approach a wide range of natural convection design problems efficiently however. Finally, a byproduct of this study was the need and development of a set of new geometry-based regularization methods for use in LSMs, a future work goal stated in a number of recent LS-XFEM studies.

3.2 Future Work

This thesis represents the initial steps in studying the class of natural convection design problems with LS-XFEM topology optimization and the development of a new feature-size measure. As such, there are a number of both short term (shown first) and more long term questions and avenues of further research, summarized here:

- *Demonstrate feature-size measure regularization for wider variety of problems:* in [M1] the measure is demonstrated for heat transfer (simplified convection) and solid mechanics design problems. Primary focuses include: better verification of sensible values for allowable constraint violations and the influence of parameter r_{tx} on a wider variety of problems.

المنارة للاستشارات
www.manaraa.com

- *Implement and demonstrate feature-size measure in 3D:* currently the implementation of the measure ([M1]) can only compute tangent surface distances for 2D shapes. An efficient and reliable implementation of this distance function is necessary to demonstrate the measure in 3D and verify that it performs properly.

- *More efficient time integration approaches for transient analysis:* in 2D natural convection, transient problems ([P2]) the sequential nature of the time integration was shown to lead to long computational times for each optimization iteration. With the constant time-step scheme many small steps were necessary to resolve to long-period heating of the device and the short-period fluid motion. The use of a variable time-step scheme would be an initial step to shorten the required computational time. Alternative problem definitions that utilize different system initial conditions are also a promising area of research.

- *Further study of scaling difficulties for 3D fluid-solid interfaces:* in 3D problems ([P2]) it was found that the linear system could become difficult to solve as geometry varied. In addition to the geometric XFEM preconditioner (Lang et al, 2014), ghost-penalty methods (Schott et al, 2014) should be studied for a variety of problems and geometries to gain a better understanding of their influence on solution robustness and accuracy.

المنارة للاستشارات
www.manaraa.com

Bibliography

Alexandersen J (2011) Topology optimization for convection problems. Bachelor thesis, DTU Mekanik

Alexandersen J (2015) Topology optimisation of passive coolers for light-emitting diode lamps. In: Proceedings of the 11th World Congress of Structural and Multidisciplinary Optimisation

Alexandersen J, Aage N, Andreasen CS, Sigmund O (2014) Topology optimisation for natural convection problems. International Journal for Numerical Methods in Fluids 76(10):699–721

Allaire G, Jouve F, Toader AM (2004) Structural optimization using sensitivity analysis and a level-set method. Journal of Computational Physics 194(1):363–393, DOI 10.1016/j.jcp.2003.09.032

Allaire G, Jouve F, Michailidis G (2014) Thickness control in structural optimization via a level set method

Bahadur R, Bar-Cohen A (2005) Thermal design and optimization of natural convection polymer pin fin heat sinks. Components and Packaging Technologies, IEEE Transactions on 28(2):238–246

Baïri A, Zarco-Pernia E, de María JMG (2014) A review on natural convection in enclosures for engineering applications. the particular case of the parallelogrammic diode cavity. Applied Thermal Engineering 63(1):304–322

Balamurugan R, Ramakrishnan C, Singh N (2008) Performance evaluation of a two stage adaptive genetic algorithm (tsaga) in structural topology optimization. Applied Soft Computing 8(4):1607–1624

Bendsøe M (1989) Optimal shape design as a material distribution problem. Structural and Multidisciplinary Optimization 1(4):193–202, DOI 10.1007/BF01650949

Bendsøe MP, Sigmund O (2003) Topology Optimization: Theory, Methods and Applications. Springer

Borrvall T, Petersson J (2003) Topology optimization of fluids in Stokes flow. International Journal for Numerical Methods in Fluids 41(1):77–107, DOI 10.1002/fld.426

Bruns T (2007) Topology optimization of convection-dominated, steady-state heat transfer problems. International Journal of Heat and Mass Transfer 50(15-16):2859 – 2873, DOI 10.1016/j.ijheatmasstransfer.2007.01.039

المنارة للاستشارات

www.manaraa.com

Cengel YA, Klein S, Beckman W (1998) Heat transfer: a practical approach. WBC McGraw-Hill Boston

Chen S, Wang M, Liu A (2008) Shape feature control in structural topology optimization. Computer-Aided Design 40(9):951–962

Deaton JD, Grandhi RV (2014) A survey of structural and multidisciplinary continuum topology optimization: post 2000. Structural and Multidisciplinary Optimization 49(1):1–38

van Dijk N, Maute K, Langelaar M, Keulen F (2013) Level-set methods for structural topology optimization: a review. Structural and Multidisciplinary Optimization 48(3):437–472, DOI 10.1007/s00158-013-0912-y

Fletcher R, Johnson T (1997) On the stability of null-space methods for kkt systems. SIAM Journal on Matrix Analysis and Applications 18(4):938–958

Fries TP, Belytschko T (2006) The intrinsic XFEM: A method for arbitrary discontinuities without additional unkowns. International Journal for Numerical Methods in Engineering 68:1358–1385, DOI 10.1002/nme.1761

Guest J, Prévost J, Belytschko T (2004) Achieving minimum length scale in topology optimization using nodal design variables and projection functions. International Journal for Numerical Methods in Engineering 61(2):238–254

Guo X, Zhang W, Zhong W (2014) Explicit feature control in structural topology optimization via level set method. Computer Methods in Applied Mechanics and Engineering 272:354–378

Häußler P, Nitsopoulos I, Sauter J, Stephan M (2006) Topology and shape optimization methods for cfd problems. In: 24th CADFEM Users' Meeting 2006, International Congress on FEM Technology with 2006 German ANSYS Conference

Iga A, Nishiwaki S, Izui K, Yoshimura M (2009) Topology optimization for thermal conductors considering design-dependent effects, including heat conduction and convection. International Journal of Heat and Mass Transfer 52(11-12):2721–2732

Jenkins N, Maute K (2015) Level set topology optimization of stationary fluid-structure interaction problems. Structural and Multidisciplinary Optimization pp 1–17, DOI 10.1007/s00158-015-1229-9, URL http://dx.doi.org/10.1007/s00158-015-1229-9

Khoei AR (2015) Extended finite element method: Theory and applications. Wiley

Koga AA, Lopes ECC, Villa Nova HF, Lima CRd, Silva ECN (2013) Development of heat sink device by using topology optimization. International Journal of Heat and Mass Transfer 64:759–772

Kontoleontos E, Papoutsis-Kiachagias E, Zymaris A, Papadimitriou D, Giannakoglou K (2013) Adjoint-based constrained topology optimization for viscous flows, including heat transfer. Engineering Optimization 45(8):941–961

Kreissl S, Maute K (2012) Levelset based fluid topology optimization using the extended finite element method. Structural and Multidisciplinary Optimization 46(3):311–326

المنارة للاستشارات
www.manaraa.com

Land AH, Doig AG (1960) An automatic method of solving discrete programming problems. Econometrica: Journal of the Econometric Society pp 497–520

Lang C, Makhija D, Doostan A, Maute K (2014) A simple and efficient preconditioning scheme for heaviside enriched XFEM. Computational Mechanics 54(5):1357–1374, DOI 10.1007/s00466-014-1063-8

Lee K (2012) Topology optimization of convective cooling system designs. PhD thesis, The University of Michigan

Liu J, Ma Y, Fu J, Duke K (2015) A novel cacd/cad/cae integrated design framework for fiber-reinforced plastic parts. Advances in Engineering Software 87:13 – 29, DOI http://dx.doi.org/10.1016/j.advengsoft.2015.04.013

Luo J, Luo Z, Chen S, Tong L, Wang M (2008) A new level set method for systematic design of hinge-free compliant mechanisms. Computer Methods in Applied Mechanics and Engineering 198(2):318–331

Luo Z, Tong L, Wang MY, Wang S (2007) Shape and topology optimization of compliant mechanisms using a parameterization level set method. Journal of Computational Physics 227(1):680–705, DOI 10.1016/j.jcp.2007.08.011

Makhija D, Maute K (2015) Level set topology optimization of scalar transport problems. Structural and Multidisciplinary Optimization 51(2):267–285

Marck G, Nemer M, Harion JL (2013) Topology optimization of heat and mass transfer problems: laminar flow. Numerical Heat Transfer, Part B: Fundamentals 63(6):508–539

Matsumori T, Kondoh T, Kawamoto A, Nomura T (2013) Topology optimization for fluid–thermal interaction problems under constant input power. Structural and Multidisciplinary Optimization 47(4):571–581

McConnell C, Pingen G (2012) Multi-layer, pseudo 3d thermal topology optimization of heat sinks. In: ASME 2012 International Mechanical Engineering Congress and Exposition, American Society of Mechanical Engineers, pp 2381–2392

Moon H, Kim C, Wang S (2004) Reliability-based topology optimization of thermal systems considering convection heat transfer. In: Tenth AIAA/ISSMO multidisciplinary analysis and optimization conference. Albany, New York, DOI 10.2514/6.2004-4410

Morrison AT (1992) Optimization of heat sink fin geometries for heat sinks in natural convection. In: Thermal Phenomena in Electronic Systems, 1992. I-THERM III, InterSociety Conference on, IEEE, pp 145–148

Nocedal J, Wright S (2006) Numerical optimization. Springer Science & Business Media

Pingen G, Waidmann M, Evgrafov A, Maute K (2010) A parametric level-set approach for topology optimization of flow domains. Structural and Multidisciplinary Optimization 41(1):117–131, DOI 10.1007/s00158-009-0405-1

Poulsen TA (2003) A new scheme for imposing a minimum length scale in topology optimization. International Journal for Numerical Methods in Engineering 57(6):741–760, DOI 10.1002/nme.694

www.manaraa.com

Rozvany G, Zhou M, Birker T (1992) Generalized shape optimization without homogenization. Structural and Multidisciplinary Optimization 4(3):250–252

Schevenels M, Lazarov BS, Sigmund O (2011) Robust topology optimization accounting for spatially varying manufacturing errors. Computer Methods in Applied Mechanics and Engineering 200(49):3613–3627

Schott B, Rasthofer U, Gravemeier V, Wall W (2014) A face-oriented stabilized nitsche-type extended variational multiscale method for incompressible two-phase flow. International Journal for Numerical Methods in Engineering pp n/a–n/a, DOI 10.1002/nme.4789, URL `http://dx.doi.org/10.1002/nme.4789`

Seo JH (2009) Optimal design of material microstructure for convective heat transfer in a solid-fluid mixture. PhD thesis, University of Michigan at Ann Arbor

Shim PY, Manoochehri S (1997) Generating optimal configurations in structural design using simulated annealing. International journal for numerical methods in engineering 40(6):1053–1069

Sigmund O (2009) Manufacturing tolerant topology optimization. Acta Mechanica Sinica/Lixue Xuebao 25(2):227–239

Sigmund O (2011) On the usefulness of non-gradient approaches in topology optimization. Structural and Multidisciplinary Optimization 43(5):589–596

Sigmund O, Maute K (2013) Topology optimization approaches: A comparative review. Structural and Multidisciplinary Optimization 48(6):1031–1055

Svanberg K (1987) The method of moving asymptotes - a new method for structural optimization. International Journal for Numerical Methods in Engineering 24(2):359–373

Svanberg K (1995a) A globally convergent version of MMA without linesearch. In: Proceedings of the First World Congress of Structural and Multidisciplinary Optimization, 28 May - 2 June 1995, Goslar, Germany, pp 9–16

Svanberg K (1995b) A globally convergent version of mma without linesearch. In: Proceedings of the first world congress of structural and multidisciplinary optimization, Goslar, Germany, vol 28, pp 9–16

Wang S, Wang M (2006) Radial basis functions and level set method for structural topology optimization. International journal for numerical methods in engineering 65(12):2060–2090

Xia Q, Shi T (2015) Constraints of distance from boundary to skeleton: For the control of length scale in level set based structural topology optimization. Computer Methods in Applied Mechanics and Engineering 295:525–542

Yaji K, Yamada T, Kubo S, Izui K, Nishiwaki S (2015) A topology optimization method for a coupled thermal–fluid problem using level set boundary expressions. International Journal of Heat and Mass Transfer 81:878–888

Yamada T, Izui K, Nishiwaki S (2011) A level set-based topology optimization method for maximizing thermal diffusivity in problems including design-dependent effects. Journal of Mechanical Design 133:031,011–1–031,011–9

المنارة للاستشارات

www.manaraa.com

Yin L, Ananthasuresh G (2002) A novel topology design scheme for the multi-physics problems of electro-thermally actuated compliant micromechanisms. Sensors and Actuators A: Physical 97:599–609

Yoon G, Kim Y (2005) The element connectivity parameterization formulation for the topology design optimization of multiphysics systems. International journal for numerical methods in engineering 64(12):1649–1677

Yoon GH (2010) Topological design of heat dissipating structure with forced convective heat transfer. Journal of Mechanical Science and Technology 24:1225–1233

Zhang W, Zhong W, Guo X (2014) An explicit length scale control approach in simp-based topology optimization. Computer Methods in Applied Mechanics and Engineering 282:71 – 86, DOI http://dx.doi.org/10.1016/j.cma.2014.08.027

Zhou M, Lazarov BS, Sigmund O (2014) Topology optimization for optical projection lithography with manufacturing uncertainties. Appl Opt 53(12):2720–2729, DOI 10.1364/AO.53.002720

Zhou M, Lazarov BS, Wang F, Sigmund O (2015) Minimum length scale in topology optimization by geometric constraints. Computer Methods in Applied Mechanics and Engineering 293:266–282

المنارة للاستشارات

www.manaraa.com

Appendix A

Publication [P1]: Level Set Topology Optimization of Cooling and Heating Devices using a Simplified Convection Model

www.manaraa.com

Structural and Multidisciplinary Optimization manuscript No.
(will be inserted by the editor)

Level Set Topology Optimization of Cooling and Heating Devices using a Simplified Convection Model

Peter Coffin · Kurt Maute

Received: date / Accepted: date

Abstract This paper studies topology optimization of convective heat transfer problems in two and three dimensions. The convective fluxes are approximated by Newton's Law of Cooling (NLC). The geometry is described by a Level Set Method (LSM) and the temperature field is predicted by the eXtended Finite Element Method (XFEM). A constraint on the spatial gradient of the level set field is introduced to penalize small, sub-element-size geometric features. Numerical studies show that the LSM-XFEM provides improved accuracy over previously studied density methods and LSMs using Ersatz material models. It is shown that the NLC model with an iso-thermal fluid phase may over predict the convective heat flux and thus promote the formation of very thin fluid channels, depending on the Biot number characterizing the heat transfer problem. Approximating the temperature field in the fluid phase by a diffusive model mitigates this issue but an explicit feature size control is still necessary to prevent the formation of small solid members, in particular at low Biot numbers. The proposed constraint on the gradient of the level set field is shown to suppress sub-element-size features but necessitates a continuation strategy to prevent the optimization process from stagnating as geometric features merge.

Keywords Topology Optimization · Level Set Method · Extended Finite Element Method · Convection · Regularization · Feature Size Control

P. Coffin · K. Maute
Department of Aerospace Engineering and Sciences
University of Colorado at Boulder
Boulder, CO 80309-0429, USA

1 Introduction

Convection is the process of heat transfer due to the motion of fluid. This process is used for thermal management in many devices, for example to cool processors in consumer electronics or to transport energy in heat exchangers. Optimizing the geometry of the cooling and heating modules plays an important role in enhancing the energy transport across material interfaces and improving the volumetric and/or gravimetric energy efficiency of such devices. This work investigates the use of topology optimization to design convective cooling and heating devices.

Convection is typically divided into two categories: natural convection, where temperature dependent buoyancy forces drive the fluid flow, and forced convection, where an external force drives the flow. Yoon (2010), Lee (2012), McConnell and Pingen (2012), Matsumori et al (2013), Marck et al (2013), Koga et al (2013), Makhija and Maute (2014a), and Yaji et al (2014) have studied topology optimization of forced convection problems, resolving flow and temperature fields. Fully-coupled natural convection problems have seen substantially less attention and to date has been studied only by Alexandersen et al (2014). In the studies above, the flow is predicted by the incompressible Navier-Stokes or the hydrodynamic Boltzmann transport equations and the thermal energy transport is described by an advection-diffusion model. While this approach accurately captures the relevant physical phenomena in the fluid, it is burdened a large computational cost. To bypass this issue, a common engineering approach is to approximate the convective heat flux by a simple model for the flux on the fluid-solid interface, which does not require the resolution of the flow field and thus reduces the computational cost. In this study, we consider Newton's Law

www.manaraa.com

of Cooling (NLC) which approximates the interface flux as follows:

$$q = \int_{\Gamma_{FS}} h \left(T - T_F\right) \, d\Gamma, \tag{1}$$

where q is the flux, h the convection coefficient, T the temperature at the fluid-solid interface, Γ_{FS}, and T_F the fluid temperature. The value of convection coefficient, h, depends on the interface geometry, the fluid motion, the temperature, and the material properties of the solid and fluid (Cengel et al, 1998). Here, we consider h being constant. NLC typically assumes a constant fluid temperature along the surface which is often set to the fluid far-field (ambient) temperature: $T_F = T_\infty$. This work considers NLC-type models where the value of T_F is either constant or varies along the interface.

For integrating NLC-type models into topology optimization it is convenient to distinguish between the following geometric configurations: Consider a three dimensional solid body immersed in a fluid, as shown in Figure 1(a). The body convects heat at the fluid-solid interface that is marked in gray. This general three dimensional configuration can be simplified to a two dimensional problem by considering either a thin or thick body. In both cases the design domain is assumed to be in the x-y plane. In Figure 1(b) a thin body is depicted that convects heat primarily at two surfaces with normals in the z-direction, i.e. normal to the design domain. Convection at the remaining surface, whose normal is in the x-y plane, is negligible and therefore ignored. A thick body is shown in Figure 1(c). Here the surfaces with a normal in the x-y plane convect heat. The convection on surfaces with normals orthogonal to the design domain may or may not be considered.

The majority of topology optimization methods considering heat convection via NLC are based on the density or SIMP (Solid Isotropic Microstructure with Penalization) approach, which was originally developed by Bendsøe (1989) and Rozvany et al (1992) for structural topology optimization. The geometry of the body is described by its material distribution within the design domain. A fictitious porous material with continuously varying density, ρ, is introduced to allow for the continuous transition between fluid and solid material, i.e. $0 \leq \rho \leq 1$ where $\rho = 0$ represents fluid and $\rho = 1$ solid. The material properties are interpolated as functions of the density. For an introduction to density methods, the reader is referred to Bendsøe and Sigmund (2003); Sigmund and Maute (2013) and Deaton and Grandhi (2014) review recent developments.

The NLC model has been integrated into SIMP topology optimization methods considering the thin 2-D configuration, for example, by Yin and Ananthasuresh (2002),

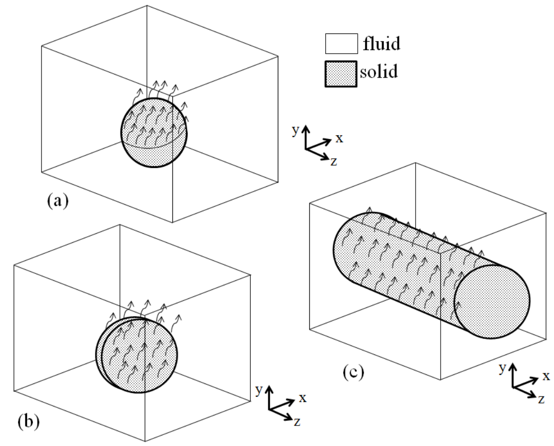

Fig. 1: General three dimensional (a) convection problem and two dimensional simplifications: thin configuration (b), thick configuration (c).

Bruns (2007), Seo (2009), and Alexandersen (2011). For this configuration, the NLC model can be conveniently embedded into density topology methods, as the convection coefficient can be interpolated as function of the density, similarly to the bulk material properties. For example, by setting the convection coefficient to zero in the fluid phase the integration of the heat flux over the entire design domain is equivalent to integrating the heat flux over just the solid domain.

Considering the thick 2-D or the general 3-D configurations in density topology optimization methods is more challenging as for these configurations the geometry of the fluid-solid interface is not explicitly defined via the material distribution. To approximate the location of the fluid-structure interface and to apply a convective heat flux, Yin and Ananthasuresh (2002) and Iga et al (2009) interpolate the convection coefficient such that the convection coefficient is maximum for an intermediate density value and vanishes at extreme density values, i.e. $\rho = 0$ and $\rho = 1$. Alexandersen (2011) follow the method suggested in Bruns (2007) and approximate the location of the interface via the spatial gradients of the density distribution; the convection coefficient is defined as a function of the density difference between neighboring elements. A similar approach is adopted by Yoon and Kim (2005) using the element connectivity parameterization method. Moon et al (2004) approximate the convective flux by surrounding the solid with a fictitious fluid phase of low diffusivity at ambient temperature.

Level set methods (LSMs) provide an interesting alternative to density topology optimization methods, in particular for problems with heat convection. The fluid-

المنارة للاستشارات
www.manaraa.com

solid interface is defined explicitly via the iso-contour of the level set function, ϕ, of a given value, typically $\phi = 0$. The reader is referred to van Dijk et al (2013) for an introduction and a review of recent developments of LSMs. Yamada et al (2011) apply an LSM to thick 2-D convection problem. The design is advanced in the optimization process via the solution of the Hamilton-Jacobi equation and an Ersatz material approach is used to project the geometry onto the finite element heat transport model. Following the boundary integration approach of Osher and Fedkiw (2002), the convection coefficient is defined as a function of the level set function and its spatial gradient, such that convection is confined to the vicinity of the fluid-solid interface.

The Ersatz material approach requires the interpolation of physical properties as functions of the level set function. Similarly to density methods, this may lead to the formation of geometric artifacts and smeared interface phenomena, affecting the resolution and accuracy of the finite element predictions (van Dijk et al, 2013). The latter issue can be overcome by adaptive mesh approaches; see, for example, Yamasaki et al (2011). In this work, we introduce the eXtended Finite Element Method (XFEM) for level set topology optimization of heat transport problems and study convection problems approximating the interface flux by NLC-type models. The XFEM interpolates the state variables and integrates the weak form of the governing equations such that the geometry of immersed material interfaces is explicitly captured. The XFEM was originally developed to describe the propagation of cracks in solids and since then has been applied to a broad range of problems with moving interfaces. The reader is referred to Fries and Belytschko (2006) for a survey of the XFEM. In the context of topology optimization, the XFEM bypasses the need for material interpolation schemes and does not smear interface phenomena. These features are particularly promising for convection problems as the NLC flux can be integrated along the immersed fluid-solid boundary conveniently. In this work, we will compare the resolution and accuracy of the XFEM formulation of NLC-type boundary conditions against SIMP and Ersatz material approaches used in previous studies.

We embed the XFEM into an explicit formulation of the LSM where the parameters of the discretized level set functions are defined as explicit functions of the optimization variables and the parameter optimization problem is solved by a nonlinear programming method. This level set approach is often referred to as the explicit LSM (van Dijk et al, 2013) and has been studied, for example, by Wang and Wang (2006), Luo et al (2007), and Pingen et al (2010). The specific approach used here is discussed in detail by Kreissl and Maute (2011). A new regularization measure will be introduced and used in concert with a perimeter measure to ensure a well-posed optimization problem. We will study the proposed combination of LSM and XFEM for both two and three dimensional problems and illustrate the influence of regularization methods on the optimized geometry.

The remainder of this paper is organized as follows: In Section 2, we outline the formulation of the optimization problems and the geometry models of density and LSMs considered in this study. In Section 3, the finite element formulations of the governing equations for both material interpolation schemes and the XFEM are presented. In the Section 4, we compare the temperature predictions for a thick 2D problem using density, Ersatz material and XFEM approaches, and we present optimization results obtained with proposed LSM-XFEM approach. The insight gained from the numerical studies are summarized in Section 5.

2 Optimization and Geometry Models

In this section, we first present the formulation of the class of optimization problems considered in this study. This is followed by a brief discussion of the geometry models of density and LSMs that are compared in Section 4.

2.1 Optimization Problem

In this study we consider two-phase design problems in two and three dimensions, which can be represented by the model configurations shown in Figure 2. In both configurations a heat flux, q_B, is applied at point B, which is located at the bottom center of the design domain. We seek to minimize the temperature, T_B, at point B over the set of designs defined by the optimization variables, $\mathbf{s}$. The design domain is limited to within a radius r_d of point B as shown in Figure 2. This restriction prevents solid material from directly interacting with boundaries of the computational domain. To regularize the optimization problem, measures of the perimeter, P, and the spatial gradient of the level set function, G, are introduced as constraints. These measures will be discussed in detail in Section 2.3. In addition, we constrain the ratio of volumes occupied by the solid and fluid phases. The optimization problem is

المنارة للاستشارات
www.manaraa.com

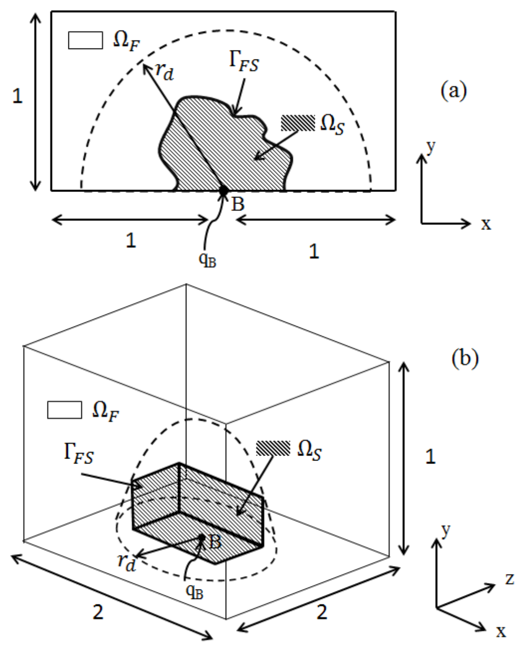

Fig. 2: Model configurations and design domains in 2D (a) and 3D (b).

defined as:

$$
\begin{aligned}
&min_{\mathbf{s}}\; p_o\; T_B(\mathbf{s})\\
&\text{s.t.}\quad (1-c_v)\,V_S(\mathbf{s}) - c_v V_F(\mathbf{s}) \leq 0,\\
&\qquad\; P(\mathbf{s}) - c_p \leq 0,\\
&\qquad\; G(\mathbf{s}) - c_g \leq 0,
\end{aligned}
\tag{2}
$$

where p_o is a scaling of the temperature in the objective. The solid volume is denoted by V_S, the fluid volume by V_F, the constrained volume ratio by c_v, the perimeter constraint value by c_p, and the gradient constraint value by c_g. The temperature field, T, is considered to be dependent on the optimization variables, $\mathbf{s}$, and is governed by the discretized state equation described in Section 3. The optimization problem (2) is solved by a nonlinear programming (NLP) method. The design sensitivities are computed by the adjoint method.

2.2 Geometry Modeling

In this work we consider density and explicit LSMs. In both methods, the geometry of a body is defined as a function of the optimization variables $\mathbf{s}$.

The density methods studied below discretize the material distribution by finite elements. We define an independent optimization variable, s_i, at each node as:

$$s_i \in \{\mathbb{R}; s_{min} \leq s_i \leq 1\}, \quad \text{for } i = 1....N_n, \tag{3}$$

where s_{min} is a lower bound of the optimization variables and N_n is the total number of nodes. The lower bound, s_{min}, is set to a small positive value to avoid ill-condition of the discretized state equations. In the thermal finite element analysis, the material properties are assumed to be element-wise constant. The elemental density, ρ_i, of the i^{th} element is computed as follows:

$$\rho_i = \rho_s \left(\sum_{j=1}^{N_n} w_{ij}\right)^{-1} \sum_{j=1}^{N_n} w_{ij} s_j \tag{4}$$

with

$$w_{ij} = max\left(0, (r - |\mathbf{x}_i^e - \mathbf{x}_j|)\right), \tag{5}$$

where ρ_s is the solid material density, $\mathbf{x}_i^e$ is position vector of the center of the i^{th} element, $\mathbf{x}_j$ the coordinates of the j^{th} node, and r the filter radius. The filter (4) prevents numerical instabilities, such as checker boarding, and mitigates the dependence of the optimization results on the mesh refinement level (Bourdin, 2001; Bruns and Tortorelli, 2001; Maute, 2014). The interpolation of thermal material properties as function of the density will be discussed in Section 3.2.

The level set function, ϕ, defines the geometry of the body as follows:

$$
\begin{aligned}
&\phi(\mathbf{x}) < 0,\, \forall\, \mathbf{x} \in \Omega_S,\\
&\phi(\mathbf{x}) > 0,\, \forall\, \mathbf{x} \in \Omega_F,\\
&\phi(\mathbf{x}) = 0,\, \forall\, \mathbf{x} \in \Gamma_{FS},
\end{aligned}
\tag{6}
$$

where $\mathbf{x}$ denotes the vector of spatial coordinates. The level set function is greater than zero in the fluid phase, Ω_F, less than zero in the solid phase, Ω_S, and equal to zero at the fluid-solid interface, Γ_{FS}.

The level set function can be parameterized to constrain variations of the geometry of the body. For example, van Miegroet and Duysinx (2007) parameterize the level set function such that the shape of an inclusion is elliptical. This approach will be used in the example of Section 4.2 to gain insight into some fundamental properties of the design problems considered in this work. In topology optimization, however, one is typically interested in finding the optimum design over a large set of possible designs. To this end, we discretize the level set function by bi-linear (2D) and tri-linear (3D) finite elements and we define an independent optimization variable, s_i, at each node as:

$$s_i \in \{\mathbb{R}; s_{min} \leq s_i \leq s_{max}\}, \quad \text{for } i = 1....N_n, \tag{7}$$

المنارة للاستشارات
www.manaraa.com

where s_{min} and s_{max} are lower and upper bounds of the optimization variables. The approach for choosing these bounds will be discussed in Section 2.3. Similarly to the density filter (4), the nodal values, ϕ_i, of the level set function are computed as follows:

$$\phi_i = \left(\sum_{j=1}^{N_n} w_{ij} \right)^{-1} \sum_{j=1}^{N_n} w_{ij} s_j, \qquad (8)$$

with

$$w_{ij} = max\left(0, (r - |\mathbf{x}_i - \mathbf{x}_j|)\right). \qquad (9)$$

The level set filter (8) widens the zone of influence of the optimization variables on the level set field and thus enhances the convergence of the optimization process (Kreissl and Maute, 2012).

2.3 LSM Regularization

Similar to density methods, LSMs also require regularization to guarantee convergence of the optimized geometry with mesh refinement and to control the size of geometric features. In addition, the spatial gradients of the level set field need to be constrained to avoid excessively flat or steep level set fields at the material interfaces which lead to poorly scaled sensitivities; see, for example, Burger and Osher (2005) and van Dijk et al (2012). In contrast to density methods, filters that either smooth the level set field or the design sensitivity fields do not regularize LSMs; see, for example, the discussions in van Dijk et al (2013) and Sigmund and Maute (2013). Therefore, the level set filter (8) does not provide regularization. In this work, we study the effectiveness of constraining the perimeter and the level set gradient measure to regularize the optimization problem.

Perimeter constraints have been studied, for example, by Maute et al (2011) and van Dijk et al (2012). While the numerical results in these studies suggest that constraining the perimeter provides effective shape control, the example in Figure 3 illustrates that imposing a perimeter constraint is insufficient to prevent the emergence of thin members. Whether or not such thin members are present in the optimized design depends on both the formulation of the optimization problem and the underlying physics. In Section 4, we will study this issue for the design of convective heating and cooling problems. Note the perimeter can be conveniently computed by integrating the area along the XFEM interface.

To simultaneously control the minimum feature size and the spatial gradients of the level set field along the fluid-solid interface we introduce the following gradient measure:

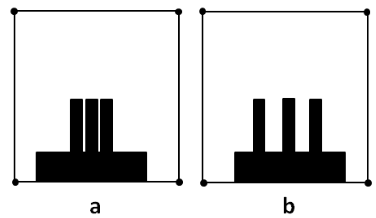

Fig. 3: Two designs with identical perimeter but different gap sizes between the solid fins.

$$G = \int e^{-\alpha^2} \left(|\nabla \phi| - d\phi_p \right)^2 d\Omega \quad \text{with } \alpha = e_p \, \frac{\phi}{\Delta\phi}, \qquad (10)$$

where e_p is a penalization parameter, $d\phi_p$ is a prescribed level set gradient and $\Delta\phi$ is the range of the level set values ϕ, here defined as:

$$\Delta\phi = \phi_{max} - \phi_{min}. \qquad (11)$$

The measure is composed of two terms: the first exponential term approaches zero away from the zero level set and unity nearby. The second term is a measure of closeness to the desired level set gradient. Constraining this measure therefore penalizes level set fields that have gradient magnitudes differing from the desired value near the interface. Setting $d\phi_p = 1.0$ promotes a signed-distance like level set field near the interface.

Constraining the gradient measure, G, bypasses the need to reinitialize the level set field throughout the optimization to ensure well scaled gradients. This reinitialization approach has been used by, for example, Wang et al (2003), Allaire et al (2004) and others. Similar to the penalization of intermediate level set values proposed by Wang and Zhou (2004), Luo et al (2009), Mohamadian and Shojaee (2012) and Zhu et al (2015), the formulation of G prevents excessively flat or steep level set fields along the fluid-solid interface. In addition, it also provides a minimum feature size control when the nodal level set values are bounded by half the element size, $s_{min} = -0.5\, h_e$ and $s_{max} = 0.5\, h_e$, noting that by construction of (8):

$$s_{min} \leq \phi_{min} \quad \text{and} \quad s_{max} \geq \phi_{max}. \qquad (12)$$

By imposing these bounds the gradient filter penalizes the occurrence of features with a size smaller than the element size. This is illustrated in Figure 4 considering two 1D elements of length h_e. The smallest feature is created by setting the level set values of the outer nodes to the lower bound, ϕ_{min}, and the value of the middle

المنارة للاستشارات
www.manaraa.com

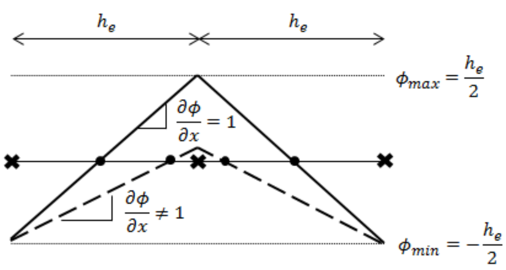

Fig. 4: Influence of gradient measure on small features, dashed line showing small feature with unsatisfied gradient, solid line with valid gradient.

node to a small positive number. To maintain a prescribed gradient of unity the smallest feature is limited to the width of an element. In general, smaller features violate the prescribed gradient and are penalized by the gradient measure. Note that the feature size control of the gradient measure (10) is tied to the interpolation of the level set function within neighboring elements and thus it cannot be directly applied to limiting features of larger or arbitrary size.

3 Thermal Analysis Model

In this section, we introduce the governing equations, summarize two material interpolation approaches to account for convective fluxes at the fluid-solid interface, and outline the XFEM used in this study.

3.1 Governing Equations

This work considers a simplified thermal model where the temperature field in the design domain is described by a linear diffusion model. Assuming steady-state conditions, the residual, $\tilde{R}_T$, of the weak form of the non-dimensional governing equation is:

$$\tilde{R}_T = \int_{\tilde{\Omega}_S} \frac{\partial \delta \tilde{T}_S}{\partial \tilde{x}_i} \, \tilde{C}_{ij,S} \, \frac{\partial \tilde{T}_S}{\partial \tilde{x}_j} \, d\Omega + \int_{\tilde{\Omega}_F} \frac{\partial \delta \tilde{T}_F}{\partial \tilde{x}_i} \, \tilde{C}_{ij,F} \, \frac{\partial \tilde{T}_F}{\partial \tilde{x}_j} \, d\Omega - \int_{\tilde{\Gamma}_q} \delta \tilde{T}_S \tilde{q}_q \, d\Gamma + \tilde{R}_\Omega - \tilde{R}_{FS} = 0, \quad (13)$$

and

$$\tilde{T}_F = \tilde{T}_\infty \quad \text{on } \in \tilde{\Gamma}_\infty. \quad (14)$$

Non-dimensional quantities are marked by $\tilde{(\cdot)}$. The non-dimensional temperature in phase $k = [F, S]$ is denoted by $\tilde{T}_k$; $\delta \tilde{T}_k$ is the associated test function, $\tilde{x}_j$ the j-th non-dimensional spatial coordinate, $\tilde{C}_{ij,k}$ the non-dimensional diffusivity tensor in phase k, and $\tilde{q}_q$ the applied non-dimensional heat flux at $\tilde{\Gamma}_q$. The reference quantities are the reference temperature, T_{ref}, the characteristic length, L_c, and the reference conductivity, κ_{ref}.

Assuming isotropic diffusion and setting the reference conductivity equal to the conductivity of the solid phase yields the following definition of the non-dimensional diffusivity tensor:

$$\tilde{C}_{ij,k} = \tilde{\kappa}_k \delta_{ij}, \quad (15)$$

where the non-dimensional diffusivity $\tilde{\kappa}_k$ is defined as:

$$\tilde{\kappa}_k = \frac{\kappa_k}{\kappa_S}. \quad (16)$$

The diffusivity of phase k is denoted by κ_k and the diffusivity of the solid phase by κ_S. The applied non-dimensional heat flux $\tilde{q}_q$ is defined as:

$$\tilde{q}_q = \frac{L_c \; q_q}{\kappa_S \; T_{ref}}, \quad (17)$$

where q_q is the dimensional heat flux. The non-dimensional ambient fluid temperature, $\tilde{T}_\infty$, is imposed at the far walls, $\tilde{\Gamma}_\infty$.

The contribution of the convective fluxes are broken into two parts: contributions integrated over the volume, R_Ω, and those integrated over the interface, R_{FS}. These contributions, which will be defined below, depend on the Biot number:

$$B = \frac{hL_c}{\kappa_S} \; . \quad (18)$$

The Biot number characterizes the ratio of convective versus diffusive fluxes. As the Biot number decreases the heat transport is convection limited and the temperature distribution in the solid becomes more uniform. For large Biot numbers the convection dominates and the heat transport is diffusion limited.

In this work, the Biot number is introduced to allow for a systematic cross comparison of the different design configurations. The Biot number defined above is design independent, as the design domain height is used as reference length, L_c, and the convection coefficient is assumed constant. Therefore, the absolute values of the Biot number likely differ from the ones derived by standard engineering practice where the Biot number is typically defined with respect to a particular geometry and temperature.

المنارة للاستشارات
www.manaraa.com

3.2 Material Interpolation Approaches

In Section 4 we will compare for thick 2-D problems the proposed LSM-XFEM approach against two approaches that rely on material interpolation schemes. The approach of Moon et al (2004) uses a SIMP method to define the geometry. Yamada et al (2011) use an LSM in combination with an Ersatz material approach. Common to both methods is that the convective surface flux is approximated via an equivalent volumetric flux and the governing equations are solved in the entire design domain, assuming a continuous temperature field. Both Moon et al (2004) and Yamada et al (2011) effectively set the value of diffusivity in the fluid domain to near-zero, but they differ in the interpolation of convection coefficient h. These differences will be discussed in the following subsections.

3.2.1 SIMP Interpolation

Moon et al (2004) present a SIMP interpolation for the thick 2-D configuration. The non-dimensional diffusion coefficient, $\tilde{\kappa}$ and the effective Biot number, B_{eff}, are interpolated as follows:

$$\tilde{\kappa} = \rho^p, \tag{19}$$

$$B_{eff} = \left(1 - \rho^{1/p}\right) B, \tag{20}$$

where p is a penalization factor. Note we dropped the subscript k in the definition of $\tilde{\kappa}$ as material interpolation schemes do not explicitly distinguish between the fluid and solid phase.

The convective flux is integrated over the entire design domain. The contribution, $\tilde{R}_\Omega$, in governing equation (13) is:

$$\tilde{R}_\Omega = \int_{\tilde{\Omega}_S \cup \tilde{\Omega}_F} \delta\tilde{T}\; B_{eff}\; \left(\tilde{T} - \tilde{T}_\infty\right)\; d\Omega. \tag{21}$$

No additional convective surface fluxes along the fluid-solid interface are modeled, i.e. $\tilde{R}_{FS} = 0$.

The diffusivity is maximum in the solid phase and vanishes in the fluid phase while the convection is maximum in the fluid phase and zero in the solid phase. Moon et al (2004) argue that embedding these two interpolation schemes into the governing equations (13) creates a model where the temperature field in the solid is only influenced by the convective flux in elements with intermediate densities along the interface. The convective flux applied in fluid phase has no influence on the solid temperature due to the vanishing diffusivity in the fluid. The interplay of diffusivity and convection in the fluid phase results in fluid temperature that is approximately equal to the ambient temperature. Therefore, the convection term (20) can be interpreted as a penalty method to weakly enforce the ambient temperature in the fluid domain.

3.2.2 Ersatz Material Approach

Yamada et al (2011) presents a level set topology optimization approach where the material parameters are interpolated based on a signed-distance function. The parameters of the Ersatz material approach are interpolated from the level set field, ϕ, by a smoothed Heaviside function, $\tilde{H}$ as follows:

$$\tilde{H}(\phi) = \begin{cases} \tilde{H}_{min} \;\forall\; \phi \leq -w_\phi \\ \hat{H}(\phi) \;\forall\; -w_\phi < \phi < w_\phi \\ 1 \quad\;\; \forall\; w \leq \phi \end{cases}, \tag{22}$$

where the parameter w_ϕ controls the width of the transition region and $\tilde{H}_{min}$ is the minimum value of the Heaviside function. The term $\hat{H}$ is defined as:

$$\hat{H}(\phi) = \tilde{H}_{min} + \left\{\frac{1}{2} + \frac{\phi}{w_\phi}\left[\frac{15}{16} + \frac{\phi^2}{w_\phi^2}\left(\frac{5}{8} - \frac{3}{16}\frac{\phi^2}{w_\phi^2}\right)\right]\right\}\left(1 - \tilde{H}_{min}\right). \tag{23}$$

This function interpolates the non-dimensional diffusivity and the effective Biot number as follows:

$$\tilde{\kappa}_k = \tilde{H}(\phi), \tag{24}$$

$$B_{eff} = \frac{\partial \tilde{H}(\phi)}{\partial \phi}\,|\nabla\phi|\;\; B, \tag{25}$$

where $\nabla\phi$ is the spatial gradient of the level set field.

As in the interpolation approach of Moon et al (2004), the contributions of the convective fluxes to the residual (13) are integrated over the entire domain using (21) with the convection coefficient being defined by (25). Again, the contribution of the convective fluxes along the fluid-solid interface, R_{FS}, vanishes.

3.3 XFEM

This work uses the XFEM formulation described in detail by Lang et al (2014). In this subsection, we summarize the basic concepts and formulations. The XFEM augments the space of test and trial functions by additional enrichment functions to capture weak or strong discontinuities within elements intersected by an interface, which is defined here by the zero level set isocontour. In this work we exclusively use Heaviside enrichment functions to resolve NLC-type flux models which allow for a jump in the temperature field at fluid-solid interface.

المنارة للاستشارات
www.manaraa.com

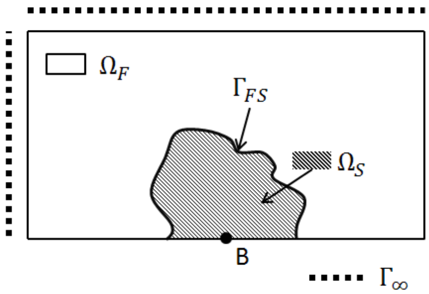

Fig. 5: Integration domains for XFEM.

Considering a two-phase problem, the temperature field, $\hat{T}$, is approximated as follows:

$$\hat{T}(\mathbf{x}) = \sum_{m=1}^{M} \left(H(-\phi(\mathbf{x})) \sum_{i}^{N_N} N_i(\mathbf{x})\ \delta_{mr}^{F,i}(\mathbf{x})\ T_{F,m}^{i} + H(\phi(\mathbf{x})) \sum_{i}^{N_N} N_i(\mathbf{x})\ \delta_{ms}^{S,i}(\mathbf{x})\ T_{S,m}^{i} \right), \quad (26)$$

where $N_i(\mathbf{x})$ are the nodal basis functions, M the number of enrichment levels, $T_{k,m}^i$ the degree of freedom at node i for phase k. The Heaviside function, H, turns on/off the sets of interpolation functions in the fluid and solid phases, and is defined as follows:

$$H(\phi) = \begin{cases} 1 & \phi > 0 \\ 0 & \phi \leq 0 \end{cases} . \quad (27)$$

The Kronecker delta, $\delta_{mr}^{k,i}$, selects the enrichment level r that interpolates the temperature in phase k at a point $\mathbf{x}$ using the degree of freedom defined at node i. Multiple enrichment levels are necessary if the degrees of freedom defined at a particular node interpolate the temperature field in multiple, physically disconnected regions. This prevents spurious coupling of the temperature fields in disconnected regions of the same phase. A detailed explanation of this phenomenon is provided by Makhija and Maute (2014b).

This work considers two different XFEM models to account for convective heat fluxes. The first model assumes an isothermal fluid phase:

$$\tilde{T}_F = \tilde{T}_\infty \quad \forall\ \mathbf{x}\ \in \Omega_F\ . \quad (28)$$

This simplification allows omitting the fluid phase in the thermal analysis. The NLC flux (1) is applied along the fluid-solid interface with $\tilde{T}_F = \tilde{T}_\infty$. The contribution to the governing equation (13) is:

$$\tilde{R}_{FS} = \int_{\Gamma_{FS}} \delta\tilde{T}_S\ B\ \left(\tilde{T}_S - \tilde{T}_\infty\right)\ d\Gamma. \quad (29)$$

No additional volume contribution, $\tilde{R}_\Omega$, exists.

Alternatively, the model can be relaxed and a spatially varying fluid temperature permitted. To this end, we model the fluid phase via a fictitious diffusive material and enforce the ambient temperature in the fluid by applying Dirichlet boundary conditions at the far walls, i.e. the design domain boundaries, Γ_∞; see Figure 5. Note that the larger the diffusivity in the fluid, the smaller is the difference between fluid temperature at the fluid-solid interface and the ambient temperature. The flux at the fluid-solid interface yields the following contribution, R_{FS}, to the governing equation (13):

$$\tilde{R}_{FS} = \int_{\tilde{\Gamma}_{FS}} \delta\tilde{T}_S\ B\left(\tilde{T}_S - \tilde{T}_F\right)\ d\Gamma - \int_{\tilde{\Gamma}_{FS}} \delta\tilde{T}_F\ B\left(\tilde{T}_S - \tilde{T}_F\right)\ d\Gamma. \quad (30)$$

As we will show below, relaxing the assumption on the fluid temperature along the fluid-solid interface mitigate the emergence of geometric artifacts for the proposed LSM-XFEM approach.

4 Numeric Results

In the following, we will first compare the accuracy of the material interpolation and XFEM schemes and then illustrate the key features of the proposed LSM-XFEM optimization approach for thick 2D and 3D problems. To gain insight into the main characteristics of the class of optimization problems considered in this work, we will initially restrict the design freedom to simple geometry variations which are defined by four optimization variables. The influence of the proposed regularization approaches will be studied with examples where the level set field is parameterized by finite element mesh.

In all examples the thermal field is discretized by bi-linear (2D) or tri-linear (3D) elements, using either a standard finite element discretization or the XFEM scheme outlined above. The design sensitivities of the objective and constraints are computed by the adjoint method. The partial derivatives of objective and constraints and of the element residuals with respect to the optimization variables are evaluated by a finite difference scheme. The optimization problems are solved by the Globally Convergent Method of Moving Asymptotes (GCMMA) of Svanberg (1995). The relative step size is 0.008 and the initial, the parameters controlling the adaptation of the lower and upper asymptotes are $0.5, 0.7$, and 1.22, respectively. The GCMMA constraint penalty is set to 50. The linear systems for both the forward and sensitivity analysis are solved by a direct solver. All problem parameters and results are given in non-dimensional form.

المنارة للاستشارات
www.manaraa.com

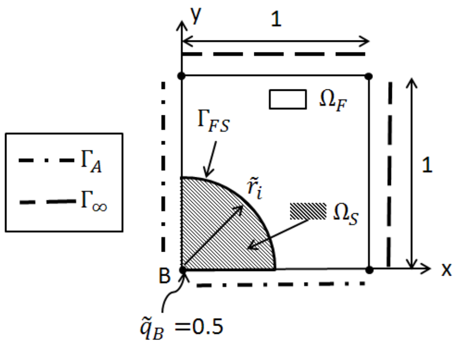

Fig. 6: Test problem for comparing temperature predictions of material interpolation methods and the XFEM.

4.1 Comparison of Convection Models

As discussed previously, the models for including the NLC flux in the topology optimization of thick 2D and 3D problems vary substantially in the literature. Here, we compare the interpolation schemes summarized in Section 3.2 to the proposed LSM-XFEM approach for the thick two dimensional problem shown in Figure 6.

The width and height of the computational domain are set to 1. The solid material forms a quarter circle of radius $\tilde{r} = 0.505$ around point B where a non-dimensional flux of $\tilde{q}_B = 0.5$ is applied. The non-dimensional diffusivity of the solid is $\tilde{\kappa}_S = 1.0$, the Biot number is $B = 0.01$, and the non-dimensional ambient fluid temperature is $\tilde{T}_\infty = 0.0$. Adiabatic boundary conditions are applied along the lower and left edges, Γ_A. For LSM-XFEM approaches the temperature at the far wall, Γ_∞, is prescribed to $\tilde{T}_F = \tilde{T}_\infty$. For the SIMP material approach, the far wall, Γ_∞, is considered adiabatic. In the Ersatz material approach we consider the far wall, Γ_∞, to be either adiabatic, as described by Yamada et al (2011), or unconstrained.

First, we consider the 10 different options of convective flux models which are summarized in Table 1. The result of a body fitted mesh (BF) serves as reference solution; here the surface flux along the fluid-solid interface is described by the NLC model with $\tilde{T}_F = \tilde{T}_\infty$. Option XL presents the LSM-XFEM approach also assuming $\tilde{T}_F = \tilde{T}_\infty$ for the fluid phase; see (29). Options XLD_1 and XLD_2 present the LSM-XFEM approach assuming a diffusive fluid as in (30). In option XLD_1 the diffusivity in the fluid, $\tilde{\kappa}_F$, is lower than the solid diffusivity; in option XLD_2 the fluid diffusivity is five times that of the solid. The level set field is initialized by a signed-distance function which describes the material layout in Figure 6.

Table 1: Methods for predicting temperature field of problem depicted in Figure 6.

Option	Approach
BF	Traditional Body Fitted Mesh Finite Element Analysis
XL	XFEM with $T_F = T_\infty$
XLD_1	XFEM with diffusive fluid phase, $\tilde{\kappa}_F = 0.1$
XLD_2	XFEM with diffusive fluid phase, $\tilde{\kappa}_F = 5.0$
S_1	SIMP interpolation scheme of Moon et al (2004), $r = 1.2$
S_2	SIMP interpolation scheme of Moon et al (2004), $r = 6.4$
E_1	Ersatz material interpolation scheme of Yamada et al (2011), $w_\phi = 0.6$, adiabatic far wall
E_2	Ersatz material interpolation scheme of Yamada et al (2011), $w_\phi = 1$, adiabatic far wall
EM_1	Ersatz material interpolation scheme of Yamada et al (2011), $w_\phi = 0.005$, unconstrained far wall
EM_2	Ersatz material interpolation scheme of Yamada et al (2011), $w_\phi = 0.016$ unconstrained far wall

Option S_1 and S_2 are the SIMP interpolation of Moon et al (2004) with different smoothing radii to vary the width of the transition zone between fluid and solid phase; see (4). At nodes within a radius $\tilde{r}_i = 0.505$ around point B the nodal densities are set to 1.0, otherwise to 10^{-9}. The penalty factor is set to $p = 3.0$. Options E_1 and E_2 are the Ersatz material interpolation of Yamada et al (2011) for different w_ϕ-parameter to vary the sharpness of the smoothed Heaviside function; see (25). The level set field is initialized by a signed-distance function. For the material interpolation schemes, the maximum diffusivity is $\tilde{\kappa} = \tilde{\kappa}_S = 1.0$ and the minimum diffusivity is set to $\tilde{\kappa}_{min} = 10^{-8}$.

We study the model options of Table 1 for different mesh refinement levels. For the material interpolation and XFEM schemes, the computational domain is discretized by uniform meshes of size:

$$N \times N \quad \text{with } N = [20, 40, 60, 80, 100, 120, 140, 160]\,. \tag{31}$$

Unstructured, body-fitted meshes with approximately the same average element length are used to compute reference solutions at these different mesh refinement levels. In Figure 7 we first plot the temperature solution of the SIMP material models with mesh refinement. Figure 7 shows significant differences between the SIMP and reference temperature solutions, ranging from $500 - 10,000\%$. The SIMP results do not appear to converge to the reference solution with mesh refinement. The proper choice of the nodal smoothing radius or penalty factor is neither known a priori nor obvious from the numerical results reported above.

المنارة للاستشارات
www.manaraa.com

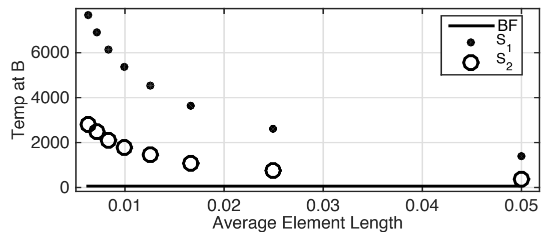

Fig. 7: Comparison of temperature at point B for SIMP material approach at different mesh refinement levels.

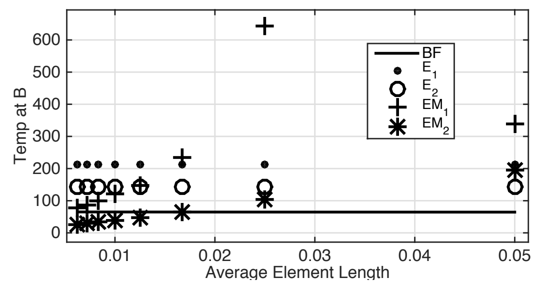

Fig. 8: Comparison of temperature at point B for Ersatz material approach at different mesh refinement levels.

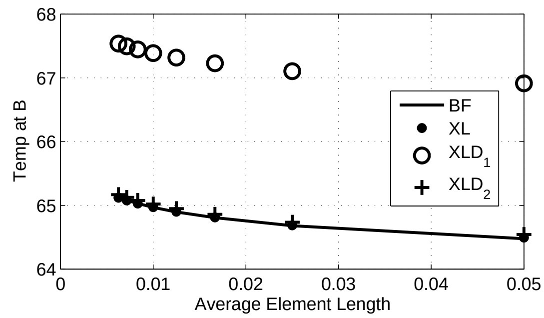

Fig. 9: Comparison of temperature at point B highlighting differences between LSM-XFEM approaches and reference solution.

The results of the Ersatz material approach of Yamada et al (2011) are plotted in Figure 8. Applying adiabatic boundary conditions along all boundaries, as suggested by Yamada et al (2011), an overly large value of transition width w_ϕ is necessary to approach the reference solution. Note that option E_2 uses a width $w_\phi = 1.0$ that covers the entire domain. For a smaller transition width, the NLC flux is significantly underestimated. Considering the far walls as unconstrained, the opposite problem is found. Choosing widths corresponding to one quarter (EM_1) and one half (EM_2) of an element width on a 50×50 mesh, the method underestimates and then overestimates the NLC flux. Again, choosing an appropriate value for topology optimization appears difficult at best. The Ersatz material approach does however provide an improvement over the SIMP approach, differences from the reference solution varying from $20 - 200\%$.

Figure 9 compares only the XFEM results to the reference solutions obtained with a body-fitted mesh. Considering a constant temperature in the fluid phase with $T_F = T_\infty$, the XFEM results agree well with the reference solutions. For the finest mesh the temperature difference is less than 0.015%. Using a diffusive fluid model with a large fluid diffusivity also converges well to the reference solution, within 0.08% difference. As the diffusivity in the fluid phase is decreased, however, the surface flux is under-predicted and the temperature at point B increases, yielding a 4% difference. As opposed to the material interpolation approaches, the error is small for the range of fluid diffusivities considered here. The relation between the error in the temperature solution and the problem parameters is simple and significantly less sensitive to mesh refinement.

Due to the inherent accuracy issues of the material interpolation schemes discussed above, only the XFEM approach will be considered in the following case studies.

4.2 Petal Geometry Optimization

To gain insight into the main characteristics of the class of optimization problems studied in this paper, we first restrict the design freedom and consider the arrangement of petals shown in Figure 10. A set of identical petals are uniformly placed around a circular base. The design variables are the petal width, $\tilde{w}$, the overall petal-base length, $\tilde{h}_t$, the radius of the petal base, $\tilde{h}_b$, and the amplitude of the curved petal edge, $\tilde{a}$. The number of petals is constant during the optimization process; configurations with different numbers of petals will be studied in the following. A level set field is constructed that describes the petal geometry as a function of the design parameters; see Appendix A.

The goal of the optimization problem is to minimize the temperature at point B at which a heat flux $\tilde{q}_B$ is applied. The lower edge is assumed adiabatic; along the other edges the temperature is set to the ambient temperature, i.e. $\tilde{T}_F = \tilde{T}_\infty$. The heat flux along the fluid-solid interface will be modeled by assuming a constant temperature in the fluid or considering the fluid phase a diffusive medium. The thermal model parameters and the mesh size are given in Table 2. Optimization results for a range of Biot numbers will be compared.

المنارة للاستشارات
www.manaraa.com

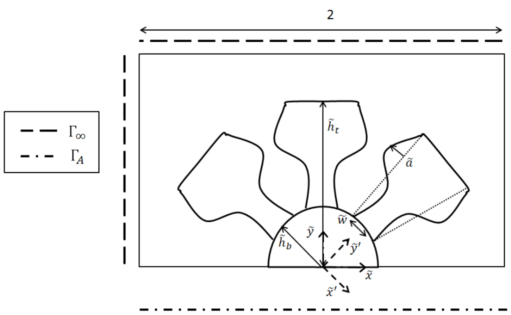

Fig. 10: Design parameterization for petal geometry optimization.

Initially we will study the characteristics of the problem without any constraint, i.e. $c_v = c_p = \infty$ in (2); later we will investigate the influence of constraints on the solid volume and the perimeter. For all examples in Subsection 4.2 there will be no constraint on the gradient measure, i.e. $c_g = \infty$. The upper and lower bounds on the optimization variable are shown in Table 3 and remain the same for all case studies in this subsection.

Table 2: Thermal model parameters of petal optimization problem.

Parameter	Value
Mesh size	100×200 elements
Ambient temperature	$\tilde{T}_\infty = 0$
Applied heat flux	$\tilde{q}_B = 1.0$
Solid conductivity	$\tilde{\kappa}_S = 1$

Table 3: Bounds of optimization variables for petal problem.

Parameter	Maximum	Minimum
Petal width, $\tilde{w}$	0.9	0
Total petal-base length, $\tilde{h}_t$	0.9	0.15
Base radius, $\tilde{h}_b$	0.25	0.15
Sine amplitude, $\tilde{a}$	0.4	-0.4

4.2.1 Unconstrained Optimization with Isothermal Fluid

Considering the unconstrained optimization problem and assuming an isothermal fluid phase, i.e. $\tilde{T}_F = \tilde{T}_\infty$, through numerical experiments we found this formulation to be non-convex, i.e. the optimization process

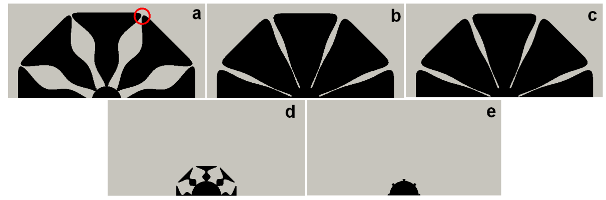

Fig. 11: Comparison of designs for varying Biot numbers: (a) $B = 0.01$, (b) $B = 0.1$, (c) $B = 1.0$, (d) $B = 10.0$, (e) $B = 100$.

stagnates prematurely in a weak local minimum. To mitigate this issue, we solve the optimization problem with different initial designs and only report on the designs with the lowest objective. The optimization variables of the 8 initial designs we considered are given in Table 4. In Figure 11 we show the optimum design with five prescribed petals for different Biot numbers: $[0.01, 0.1, 1.0, 10.0, 100]$. The index id of the initial configuration, the temperatures of the initial and optimized design, and the optimized values of the design variables are reported in Table 5.

Table 4: Initial Configurations (IC) for petal optimization study.

IC index	$\tilde{w}$	$\tilde{h}_t$	$\tilde{h}_b$	$\tilde{a}$
1	0.9	0.9	0.25	0.0
2	0.9	0.9	0.15	0.0
3	0.9	0.15	0.25	0.0
4	0.9	0.15	0.15	0.0
5	0.0	0.9	0.25	0.0
6	0.0	0.9	0.15	0.0
7	0.0	0.15	0.25	0.0
8	0.0	0.15	0.15	0.0

The optimized designs strongly depend on the Biot number. For large Biot numbers the problem is diffusion limited and therefore the conductive path between the fluid-solid interface and point B is minimized. The largest Biot number, $B = 100.0$, yields a design with small, almost vanishing petals. For small Biot numbers

Table 5: Optimized designs for varying Biot numbers.

Biot	IC Index	Initial Temp	Final Temp	$\tilde{w}$	$\tilde{h}_t$	$\tilde{h}_b$	$\tilde{a}$
0.01	6	14.188	12.305	0.126	0.900	0.150	-0.168
0.10	2	3.071	3.036	0.900	0.900	0.150	-0.032
1.00	2	1.964	1.958	0.900	0.900	0.150	-0.032
10.00	8	1.764	1.694	0.135	0.305	0.151	-0.400
100.00	7	1.727	1.572	0.126	0.169	0.150	0.015

www.manaraa.com

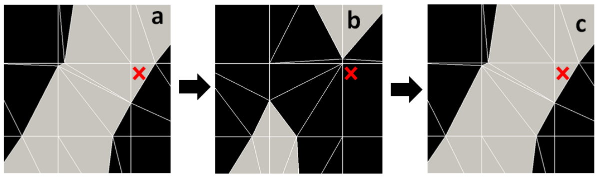

Fig. 12: Sequence of designs in the course of the optimization process.

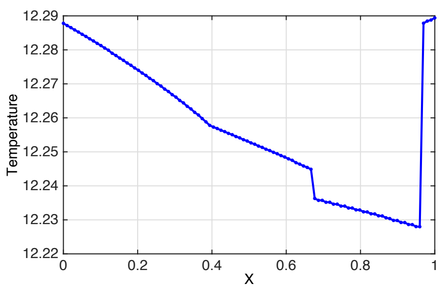

Fig. 13: Local minima as petals meet. $X = 0$: Figure 12 (a), $X = 1$: Figure 12 (b).

the problem is convection limited and the surface area of the fluid-solid interface is maximized, leading to thin fluid channels between the petals.

As the width of the fluid channels drops below the size of an element, the LSM-XFEM formulation used here creates a local discontinuous minimum and causes the optimization process to oscillate around this minimum. Figure 12 shows a magnified view of the area marked by the red circle in Figure 11 (a) in the course of three successive iterations as the optimization process oscillates.

The reasons for these oscillations are two-fold: Fundamentally, the LSM relies on shape sensitivities which do not capture the change in the thermal response as two solid domains merge and the convective surface flux vanishes. In addition, the interpolation of the level set field used here causes a potentially discontinuous evolution of the geometry as the feature size drops below the width of an element.

The latter issue is illustrated in Figure 13 where we plot the temperature at point B when linearly interpolating between the optimization parameters of the designs in Figure 12 (a) and (b). The primary jump in temperature coincides with the sign of the level set function at the node marked by a cross in Figure 12 flipping. Due to the linear interpolation of the level set function along element edges, the sign flip causes the gap between two petals to abruptly close which leads to a discontinuous change in the temperature field. The oscillatory behavior of the optimization process is due

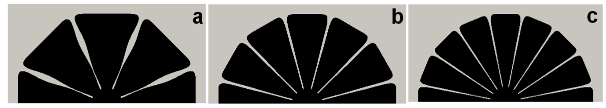

Fig. 14: Comparison of designs for varying numbers of petals at $B = 1.0$: (a) 5 petals, (b) 7 petals, (c) 9 petals.

Table 6: Optimized designs for varying number of petals.

Num petals	IC Index	Initial Temp	Final Temp	$\tilde{w}$	$\tilde{h}_t$	$\tilde{h}_b$	$\tilde{a}$
5.00	2	1.964	1.958	0.900	0.900	0.150	-0.032
7.00	1	1.999	1.902	0.842	0.900	0.150	-0.008
9.00	5	2.162	1.864	0.819	0.900	0.150	-0.007

the slope of the T_B-curve in temperature curve in Figure 13 which suggests that the optimum is "between" the two designs, i.e. it features a very thin fluid channel with a width below the size of an element. Note the oscillations in optimization process would likely remain even if the interpolation of the level set field allowed for a continuous geometry evolution and the formation of sub-element-size channels. The shape sensitivities are fundamentally unable to capture the strong discontinuity of this NLC model as solid domains merge.

The tendency of the NLC model with an isothermal fluid phase to promote the formation of thin fluid channels is also observed for higher Biot numbers. In Figure 14 we show the optimized designs for $B = 1.0$ as the number of petals increases from five to nine. The index id of the initial configuration, the temperatures of the initial and optimized designs, and the optimized values of the design variables are reported in Table 6. The width of the fluid channel decreases as the number of petals increases. Note we did not observe any oscillations in the optimization process for these results.

The numerical experiments discussed above suggest that the NLC model with an isothermal fluid phase promotes for low Biot numbers the formation of very thin fluid channels which cannot be resolved by the discretized level set field and lead to discontinuous local minima. Note that as this NLC model assumes a constant design independent Biot number and a constant fluid temperature, the energy transport in the fluid phase is over-predicted. In the following we will show that this problem cannot be overcome with volume and perimeter constraints, but requires some form of minimum feature size control. We will further study whether approximating the heat transport in the fluid phase via a diffusive model mitigates the issue of the NLC model with an isothermal fluid phase.

المنارة للاستشارات
www.manaraa.com

Fig. 15: Comparison of optimized designs for $B = 0.1$: (a) unconstrained, (b) perimeter constrained, and (c) volume constrained.

Table 7: Pedal optimization with varying geometric constraints.

Constraint	None	Perimeter	Volume
IC Index	2	2	6
Initial Temp	3.071	3.071	3.755
Final Temp	3.036	4.284	4.146
$\tilde{w}$	0.900	0.895	0.104
$\tilde{h}_t$	0.900	0.465	0.476
$\tilde{h}_p$	0.150	0.150	0.208
$\tilde{a}$	-0.032	-0.019	-0.394
Final Perimeter	8.96	4.00	5.16
Final Area Ratio	0.607	0.160	0.100

4.2.2 Area and Perimeter Constraints

If area and perimeter constraints are imposed, the emergence of thin fluid channel is still observed. Figure 15 shows the optimized designs for a Biot number of $B = 0.1$ considering (a) no constraint, (b) a perimeter constraint with $c_p = 4.0$, and (c), a constraint on the solid volume with $c_v = 0.1$, i.e. no more than 10 % of the computational domain can be occupied by solid. These design are the ones with the lowest objective while being feasible when starting from the initial configurations listed in Table 4. The index id of the initial configuration, the temperatures of the initial and optimized design, and the optimized values of the design variables are reported in Table 7.

This study suggests that imposing a perimeter constraint essentially shrinks the design without noticeably widening the fluid channels. Note that the temperature and the perimeter are strongly coupled in the NLC design problem considered here, as the total convective flux is a function of the surface area. Imposing a constraint on the maximum perimeter limits the total convective flux and thus the minimum objective temperature, which is seen in Table 7. The limitations of the perimeter constraint have also been noted by Villanueva and Maute (2014) in the context of structural topology optimization. Constraining the area is also ineffective in preventing a narrow gap between the petals at their tips as well as thin solid members at the circular base.

(a) $B = 0.01$ $\tilde{\kappa}_F = 0.1$ (b) $B = 0.01$ $\tilde{\kappa}_F = 1.0$ (c) $B = 0.01$ $\tilde{\kappa}_F = 5.0$

(d) $B = 0.1$ $\tilde{\kappa}_F = 0.1$ (e) $B = 0.1$ $\tilde{\kappa}_F = 1.0$ (f) $B = 0.1$ $\tilde{\kappa}_F = 5.0$

Fig. 16: Influence of fluid diffusivity on optimized design.

4.2.3 Diffusive Fluid Model

The NLC flux with isothermal fluid phase over-predicts the energy transport in the fluid. To mitigate the effect of this error on the optimized design, we model the fluid phase by a diffusive medium and study the influence of the fluid diffusivity on the optimized design for two Biot numbers: $B = [0.01, 0.1]$.

Figure 16 shows the optimized designs. The index id of the initial configuration, the temperatures of the initial and optimized design, and the optimized values of the design variables are reported in Table 8. These results suggest that reducing the fluid diffusivity promotes wider fluid channels. The smaller the fluid diffusivity, the more the fluid temperature at the fluid-solid interface deviates from the ambient temperature and the overall energy transport is limited by the diffusivity of the fluid.

While augmenting the NLC flux with a diffusive fluid model leads to a more realistic energy transport prediction and discourages the formation of thin fluid channels, it does not prevent thin solid members. This phenomenon is pronounced for low Biot numbers (see Figure 16 (a)-(c)) where the heat transfer is limited by either the surface convection or the energy transport in the fluid. These results suggest that the minimum feature size needs to be constrained even when the NLC model does not promote thin fluid channels.

4.3 2D Thick Topology Optimization

We increase the design freedom and investigate the behavior of the LSM-XFEM approach for topology optimization, where the level set function is parameterized by a finite element mesh; see Section 2.2. We study the 2D thick case of the design problem defined in Section 2.1 and depicted in Figure 2 (a). Note the height

www.manaraa.com

Table 8: Optimization results for NLC Model with diffusive fluid phase.

κ_f	Biot	IC	Initial Temp	Final Temp	$\tilde{w}$	$\tilde{h}_t$	$\tilde{h}_b$	$\tilde{a}$
0.10	0.01	5	17.802	16.303	0.081	0.900	0.250	-0.192
1.00	0.01	5	15.613	13.055	0.081	0.900	0.250	-0.264
5.00	0.01	6	14.263	12.491	0.135	0.900	0.150	-0.168
0.10	0.10	2	5.315	5.154	0.540	0.900	0.250	-0.056
1.00	0.10	6	4.160	3.599	0.520	0.900	0.204	-0.069
5.00	0.10	2	3.255	3.207	0.765	0.900	0.150	-0.048

and width of the design domain are non-dimensional. The symmetry of the problem is exploited such that optimization variables are only defined on half of the domain, their values reflected to the opposing half.

We consider the NLC flux model with a diffusive fluid phase and study the behavior of the optimization problem for different Biot numbers and conductivities in the fluid phase. The problem parameters are defined in Table 9. We investigate the need and influence of constraining the minimum feature size through the proposed gradient measure (10). If no constraint on the minimum feature size is imposed, the maximum allowable value of gradient measure is set to $c_g = \infty$. To prevent "trivial" solutions where the design domain is simply occupied by solid material, we also constrain the volume of the solid phase. To formally eliminate the perimeter constraint in (2), we set $c_p = \infty$ for selected examples.

The optimization process is started from one of two initial designs. To generate the first configuration, we place a semi-circle of solid material with radius $\tilde{r}_i = 0.9$ at the center of the bottom edge and then remove material corresponding to an evenly spaced grid of 10×5 cuboids of height and width 0.16; see Figure 17. The second configuration is a semi-circle of radius $\tilde{r}_i = 0.5$ at the center of the bottom edge; see Figure 2. The optimization variables are initialized by a corresponding signed-distance function which is truncated at the optimization variable bounds, $s_{min} = -0.01$ and $s_{max} = 0.01$. The mesh is composed of 100×50 elements. The initial and final values of the objective temperature, T_B, for each design are shown in Tables 10, 11, 12 & 14.

4.3.1 Area and Perimeter Constrained Optimization

First we minimize temperature T_B subject to only a volume constraint on solid material. The same difficulties are observed using a finite element discretization of the level set function as were found with the petal parameterization of Section 4.2. Figure 18 shows the final designs for a selection of Biot numbers and fluid diffusivities using the initial design with an array of inclusions. The cases with a high fluid diffusivity, (d) and (e), do not converge and the level set fields oscillate in regions with complex, fine features. For larger Biot numbers the design problem is more benign. As the fluid diffusivity decreases the designs reach out towards the far walls where the $\tilde{T}_F = \tilde{T}_\infty$ is applied.

Starting from the semi-circular initial design, significantly different designs are found; see Figure 19. The final designs show less geometric complexity, exemplified by (b), (c) and (f). These results suggest that the LSM designs may strongly depend on the initial design,

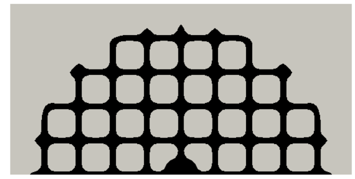

Fig. 17: Initial design with array of inclusions.

Table 9: Problem parameters of 2D thick topology optimization problem.

Parameter	Value
Ambient temperature	$\tilde{T}_\infty = 0.0$
Flux at point B	$\tilde{q}_B = 1.0$
Biot number	$B = \{0.01, 10.00\}$
Solid diffusivity	$\tilde{\kappa}_S = 1.0$
Fluid diffusivity	$\tilde{\kappa}_F = \{0.001, 0.1, 5.0\}$
Temperature scaling	$p_o = 10$
Perimeter constraint	$c_p = \infty$
Gradient measure constraint	$c_g = \{\infty, 0.04\}$
Material volume constraint	$c_v = 0.3$
Level set smoothing radius	$\tilde{r} = 0.048$
Gradient measure penalty	$e_p = 5$
Design domain radius	$\tilde{r}_d = 0.9$

(a) $B = 10.0$ $\tilde{\kappa}_F = 5.0$ (b) $B = 10.0$ $\tilde{\kappa}_F = 0.1$ (c) $B = 10.0$ $\tilde{\kappa}_F = 0.001$

(d) $B = 0.1$ $\tilde{\kappa}_F = 5.0$ (e) $B = 0.1$ $\tilde{\kappa}_F = 0.1$ (f) $B = 0.1$ $\tilde{\kappa}_F = 0.001$

Fig. 18: Final designs arriving from initial design of Figure 17 for varying Biot and fluid diffusivity.

www.manaraa.com

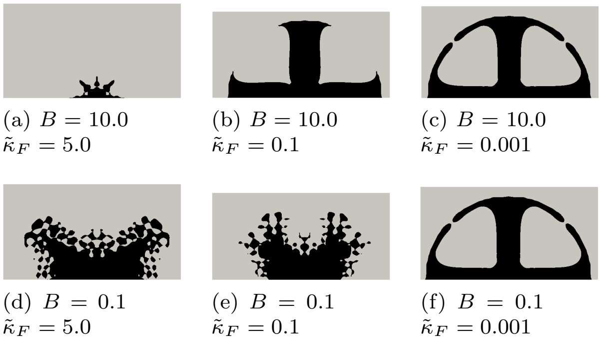

(a) $B = 10.0$ $\tilde{\kappa}_F = 5.0$ (b) $B = 10.0$ $\tilde{\kappa}_F = 0.1$ (c) $B = 10.0$ $\tilde{\kappa}_F = 0.001$

(d) $B = 0.1$ $\tilde{\kappa}_F = 5.0$ (e) $B = 0.1$ $\tilde{\kappa}_F = 0.1$ (f) $B = 0.1$ $\tilde{\kappa}_F = 0.001$

Fig. 19: Final designs arriving from circular initial design for varying Biot and fluid diffusivity.

in particular for problems that are dominated by surface phenomena.

Table 10: Figure 18 design parameters.

Value	(a)	(b)	(c)	(d)	(e)	(f)
Initial Design Temperature, T_B	2.15	4.21	72.8	7.11	7.92	77.2
Final Design Temperature, T_B	1.55	2.86	56.8	3.44	5.07	60.7
Final Volume Ratio, $\frac{V_S}{V_S+V_F}$	0.0212	0.300	0.300	0.277	0.251	0.300
Perimeter, P	1.81	13.7	16.4	17.1	12.0	16.2

Introducing a constraint on perimeter does not simply eliminate the difficulties due to small features. The final designs corresponding to a selection of perimeter constraint values are shown in Figure 20. As the allowable perimeter is decreased the complexity does appear to decrease, particularly in Figure 20 (d), however thin regions of fluid are still observed. These features continue to evolve, closing and reforming, failing to converge to a distinct design.

4.3.2 Gradient Measure Constraint

To prevent the formation of small features which are observed in particular for configurations with low Biot numbers and high fluid conductivities, see Figures 18 and 19 (d) and (e), we constrain the value of the level set gradient measure (10) in addition to the area constraint.

Imposing strict limits on the gradient measure throughout the optimization process may prevent the design

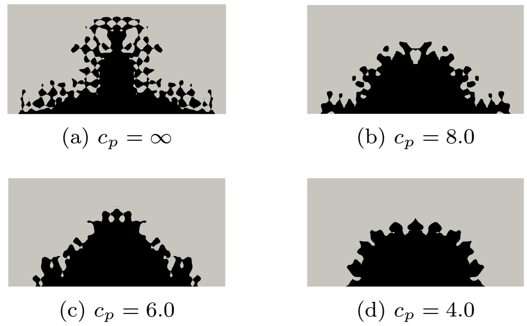

(a) $c_p = \infty$ (b) $c_p = 8.0$

(c) $c_p = 6.0$ (d) $c_p = 4.0$

Fig. 20: Final designs arriving from initial design of Figure 17, $B = 0.1$, $\tilde{\kappa}_F = 5.0$ for varying perimeter constraint values.

Table 11: Figure 19 design parameters.

Value	(a)	(b)	(c)	(d)	(e)	(f)
Initial Design Temperature, T_B	1.83	4.23	247	8.14	10.5	253
Final Design Temperature, T_B	1.58	2.93	57.1	3.30	4.74	60.9
Final Volume Ratio, $\frac{V_S}{V_S+V_F}$	0.0231	0.300	0.300	0.288	0.287	0.300
Perimeter, P	1.73	4.37	7.21	14.8	12.2	9.55

Table 12: Figure 20 design parameters.

Value	(a)	(b)	(c)	(d)
Initial Design Temperature, T_B	7.11	7.11	7.11	7.11
Final Design Temperature, T_B	2.86	3.93	3.76	4.27
Final Volume Ratio, $\frac{V_S}{V_S+V_F}$	0.287	0.299	0.299	0.279
Perimeter, P	17.4	7.85	6.20	4.06

from undergoing topological changes. In the process of inclusions merging, thin features are typically formed and their thickness is successively reduced until the feature vanishes and the inclusions merge. If the constraint limit for the gradient measure is too low, this process stagnates as the thickness of the feature approach the size of an element. To mitigate this issue, we adopt a continuation strategy, start with a large constraint limit, and successively lower the limit in the course of the optimization process. Note, whether or not a strict enforcement of the gradient measure constraint causes

المنارة للاستشارات
www.manaraa.com

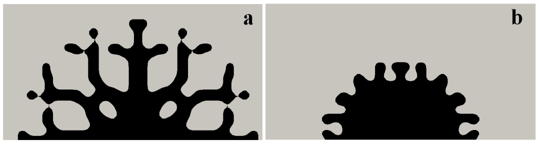

Fig. 21: Final designs for Biot = 0.1 and $\tilde{\kappa}_F = 5.0$ with constrained gradient measure (10) corresponding to (a) initial design with inclusions (Figure 17) and (b) circular initial design.

the design process to stagnate depends on the initial design and the evolution of the geometry in the optimization process.

The continuation approach described above is applied to the initial configuration of Figure 17. The optimized geometry is shown in Figure 21 (a). The number of optimization iterations at each constraint level is given in Table 13. Starting from semi-circular initial configuration yields the design in Figure 21 (b). Note in this case the continuation approach is not needed and a strict limit of the gradient constrained measure can be applied from the start of the optimization process.

As observed previously, the optimization results depend strongly on the initial designs. While the proposed gradient measure is effective in preventing the formation of small features, it does not guarantee that the optimization process converges to a unique solution. We also observe that the optimization results typically depend on the implementation of the continuation strategy. If the constraint limit is lowered too rapidly, isolated features of solid material may be prevented from vanishing; see 21(a). Finding an optimal control strategy for the continuation process needs to be developed in future studies.

Table 13: Continuation approach used in Figure 21 (a).

Gradient constraint, c_g	Corresponding number of optimization iterations
0.16	100
0.15	100
0.14	100
0.13	100
0.12	100
0.11	100
0.10	100
0.09	100
0.08	100
0.07	100
0.06	100
0.05	100
0.04	300

Table 14: Figure 21 design parameters.

Value	(a)	(b)
Initial Design Temperature, T_B	5.67	8.14
Final Design Temperature, T_B	3.14	4.50
Final Volume Ratio, $\frac{V_S}{V_S+V_F}$	0.299	0.219
Perimeter, P	10.8	3.70
Gradient Measure, G	0.102	0.0400

4.4 Three Dimensional Optimization Problem

To demonstrate the applicability of the proposed optimization method to three dimensional problems, we next study the problem depicted in Figure 2 and consider two configurations: (a) low Biot number with high fluid diffusivity ($B = 0.1, \tilde{\kappa}_F = 10$), and (b) low fluid conductivity ($B = 0.1, \tilde{\kappa}_F = 0.001$). The problem parameters are summarized in Table 15. The design domain is discretized by a $80 \times 80 \times 40$ element mesh, consisting of eight-node, hexahedral elements. The optimization variables are initialized with a signed-distance function corresponding to an initial half-sphere of radius $\tilde{r} = 0.457$ and truncated at $s_{min} = -0.01$ and $s_{max} = 0.01$. No symmetry is enforced with respect to the design.

The final designs are shown in Figure 22. Similarly to the 2D results above, the low Biot number with large fluid diffusivity yields a design with more compact features while the lowering the fluid diffusivity yields longer, finger-like structures. Objective temperatures, T_B, for the initial and final designs are shown in Table 16.

Table 15: 3D problem parameters.

Parameter	Value
Far-field fluid temp	$\tilde{T}_\infty = 0$
Flux at B	$\tilde{q}_B = 1$
Biot number	$B = [0.1]$
Solid diffusivity	$\tilde{\kappa}_S = 1$
Fluid diffusivity	$\tilde{\kappa}_F = [0.1, 10]$
Temperature scaling	$p_o = 0.1$
Perimeter constraint	$c_p = \infty$
Gradient measure constraint	$c_g = 0.06$
Material volume constraint	$c_v = 0.1$
Level set smoothing radius	$\tilde{r} = 0.048$
Gradient measure penalty	$e_p = 5$
Design domain radius	$\tilde{r}_d = 0.9$

المنارة للاستشارات
www.manaraa.com

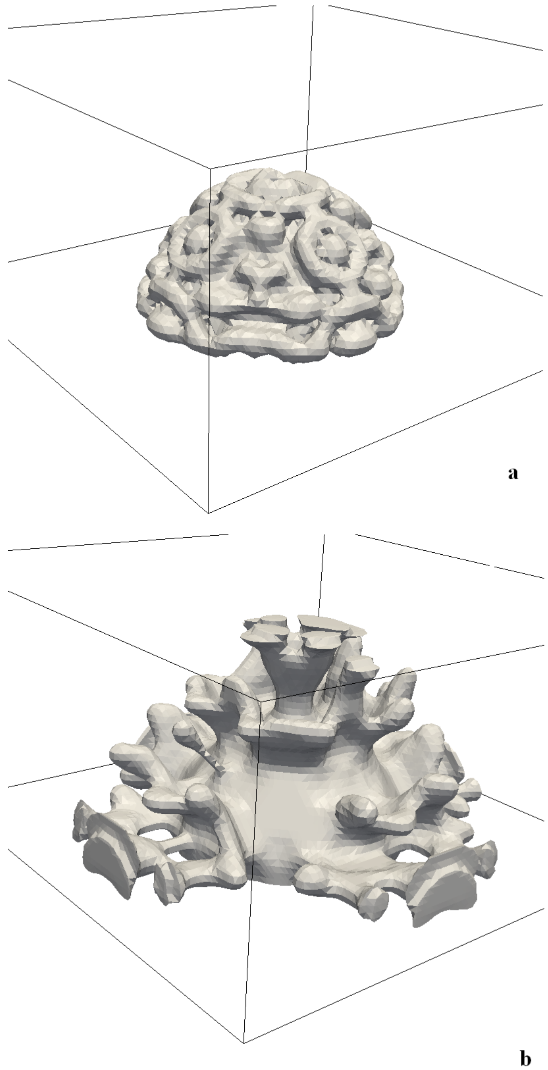

Fig. 22: 3D Designs with Biot = 0.1, $\tilde{\kappa}_F = 10$ (a) and $\tilde{\kappa}_F = 0.001$ (b).

Table 16: 3D topology optimization design temperatures.

Design	Initial Design Temperature, T_B	Final Design Temperature, T_B
Figure 22 (a)	42.3	37.1
Figure 22 (b)	63.3	48.5

5 Conclusions

This paper has presented an LSM-XFEM topology optimization approach for convective heat transfer problems. The flux along the fluid-solid interface is approximated by Newton's Law of Cooling, either considering an iso-thermal fluid phase or modeling the fluid as a diffusive material. The geometry is described by a level set method and the temperature field is predicted by the eXtended Finite Element Method. The study focused on 2D thick and 3D design problems.

The numerical experiments presented in this paper showed that the XFEM provides improved accuracy and reliability in predicting the temperature fields over previously studied density methods and LSMs using an Ersatz material model. Numerical studies of optimizing the shape of petals illustrated that the NLC model with an iso-thermal fluid phase over predicts the convective heat flux and thus promotes the formation of very thin fluid channels. This behavior is pronounced at low Biot numbers. Approximating the temperature field in the fluid phase by a diffusive model mitigates this issue but an explicit feature size control is still necessary to prevent the formation of small solid members, in particular at low Biot numbers.

Constraining the perimeter of the solid phase was shown to be inefficient to control the feature size. Therefore, a constraint on the spatial gradient of the level set field was introduced to penalize small, sub-element-size geometric features. To prevent the optimization process from stagnating as geometric features merge, the gradient measure constraint was applied via a continuation method, gradually lowering the constraint limit.

The main conclusions drawn from the numerical studies presented in this paper can be summarized as follows: While the NLC model provides a simple approach to consider convective fluxes in design optimization problems, it may significantly over predict the heat flux if an isothermal fluid phase is considered. This modeling error can significantly affect the optimized design by promoting the formation of thin fluid channels. While approximating the energy transport in the fluid phase via a diffusive model mitigates this issue, the validity of this model for a broad range of fluid problems is questionable. Therefore, we recommend modeling the fluid phase via an appropriate flow model.

The Biot number and the diffusivity of the fluid phase have a significant impact on the optimized designs. In particular considering low Biot numbers and high fluid conductivities leads to more complex design problems, which require some form of feature size control. Therefore we recommend studying a wide range of heat transfer and flow characteristics when introducing new topology optimization approaches for this class of optimization problems. Only considering benign problems at high Biot numbers and low flow conductivities is insufficient for demonstrating the robustness and applicability of optimization methods.

المنارة للاستشارات
www.manaraa.com

The proposed constraint on the spatial gradients of the level set functions is effective in suppressing subelement-size features. However, it lacks the flexibility to suppress feature of any user defined size. The reader is referred to Chen et al (2008) and Guo et al (2014) for alternative approaches which consider mesh-independent features sizes but are computationally more costly and may require the level set field to be a signed-distance function. More importantly, our study has shown that imposing feature size control in LSMs requires some form of continuation method. Finding an optimal continuation strategy was beyond the scope of this paper but deserves attention in future research.

Acknowledgements The authors acknowledge the support of the National Science Foundation under grant EFRI-SEED 1038305 and CBET 1246854. The opinions and conclusions presented in this paper are those of the authors and do not necessarily reflect the views of the sponsoring organization.

References

Alexandersen J (2011) Topology optimization for convection problems. Master's thesis, DTU Mekanik

Alexandersen J, Aage N, Andreasen CS, Sigmund O (2014) Topology optimisation for natural convection problems. International Journal for Numerical Methods in Fluids 76(10):699–721

Allaire G, Jouve F, Toader AM (2004) Structural optimization using sensitivity analysis and a level-set method. Journal of Computational Physics 194(1):363–393, DOI 10.1016/j.jcp.2003.09.032

Bendsøe M (1989) Optimal shape design as a material distribution problem. Structural and Multidisciplinary Optimization 1(4):193–202, DOI 10.1007/BF01650949

Bendsøe MP, Sigmund O (2003) Topology Optimization: Theory, Methods and Applications. Springer

Bourdin B (2001) Filters in topology optimization. International Journal for Numerical Methods in Engineering 50(9):2143–2158

Bruns T (2007) Topology optimization of convection-dominated, steady-state heat transfer problems. International Journal of Heat and Mass Transfer 50(15-16):2859 – 2873, DOI 10.1016/j.ijheatmasstransfer.2007.01.039

Bruns T, Tortorelli D (2001) Topology optimization of non-linear elastic structures and compliant mechanisms. Computer Methods in Applied Mechanics and Engineering 190(26-27):3443–3459

Burger M, Osher SJ (2005) A survey in mathematics for industry a survey on level set methods for inverse problems and optimal design. Euro Jnl of Applied Mathematics 16:263–301

Cengel YA, Klein S, Beckman W (1998) Heat transfer: a practical approach. WBC McGraw-Hill Boston

Chen S, Wang M, Liu A (2008) Shape feature control in structural topology optimization. Computer-Aided Design 40(9):951–962

Deaton JD, Grandhi RV (2014) A survey of structural and multidisciplinary continuum topology optimization: post 2000. Structural and Multidisciplinary Optimization 49(1):1–38

van Dijk N, Langelaar M, van Keulen F (2012) Explicit level-set-based topology optimization using an exact heaviside function and consistent sensitivity analysis. International Journal for Numerical Methods in Engineering 91(1):67–97, DOI 10.1002/nme.4258

van Dijk N, Maute K, Langelaar M, Keulen F (2013) Level-set methods for structural topology optimization: a review. Structural and Multidisciplinary Optimization 48(3):437–472, DOI 10.1007/s00158-013-0912-y

Fries TP, Belytschko T (2006) The intrinsic XFEM: A method for arbitrary discontinuities without additional unkowns. International Journal for Numerical Methods in Engineering 68:1358–1385, DOI 10.1002/nme.1761

Guo X, Zhang W, Zhong W (2014) Explicit feature control in structural topology optimization via level set method. Computer Methods in Applied Mechanics and Engineering 272:354–378

Iga A, Nishiwaki S, Izui K, Yoshimura M (2009) Topology optimization for thermal conductors considering design-dependent effects, including heat conduction and convection. International Journal of Heat and Mass Transfer 52(11-12):2721–2732

Koga AA, Lopes ECC, Villa Nova HF, Lima CRd, Silva ECN (2013) Development of heat sink device by using topology optimization. International Journal of Heat and Mass Transfer 64:759–772

Kreissl S, Maute K (2011) Topology optimization for unsteady flow. International Journal for Numerical Methods in Engineering 87:1229–1253

Kreissl S, Maute K (2012) Levelset based fluid topology optimization using the extended finite element method. Structural and Multidisciplinary Optimization 46(3):311–326

Lang C, Makhija D, Doostan A, Maute K (2014) A simple and efficient preconditioning scheme for heaviside enriched XFEM. Computational Mechanics 54(5):1357–1374, DOI 10.1007/s00466-014-1063-8

Lee K (2012) Topology optimization of convective cooling system designs. PhD thesis, The University of Michigan

المنارة للاستشارات
www.manaraa.com

Luo Z, Tong L, Wang MY, Wang S (2007) Shape and topology optimization of compliant mechanisms using a parameterization level set method. Journal of Computational Physics 227(1):680–705, DOI 10.1016/j.jcp.2007.08.011

Luo Z, Tong L, Luo J, Wei P, Wang M (2009) Design of piezoelectric actuators using a multiphase level set method of piecewise constants. Journal of Computational Physics 228(7):2643–2659

Makhija D, Maute K (2014a) Level set topology optimization of scalar transport problems. Structural and Multidisciplinary Optimization DOI 10.1007/s00158-014-1142-7

Makhija D, Maute K (2014b) Numerical instabilities in level set topology optimization with the extended finite element method. Structural and Multidisciplinary Optimization 49(2):185–197

Marck G, Nemer M, Harion JL (2013) Topology optimization of heat and mass transfer problems: laminar flow. Numerical Heat Transfer, Part B: Fundamentals 63(6):508–539

Matsumori T, Kondoh T, Kawamoto A, Nomura T (2013) Topology optimization for fluid–thermal interaction problems under constant input power. Structural and Multidisciplinary Optimization 47(4):571–581

Maute K (2014) Topology optimization of diffusive transport problems. In: Rozvany G, Lewiski T (eds) Topology Optimization in Structural and Continuum Mechanics, CISM International Centre for Mechanical Sciences, vol 549, Springer Vienna, pp 389–407

Maute K, Kreissl S, Makhija D, Yang R (2011) Topology optimization of heat conduction in nanocomposites. In: 9th World Congress on Structural and Multidisciplinary Optimization, Shizuoka, Japan

McConnell C, Pingen G (2012) Multi-layer, pseudo 3d thermal topology optimization of heat sinks. In: ASME 2012 International Mechanical Engineering Congress and Exposition, American Society of Mechanical Engineers, pp 2381–2392

van Miegroet L, Duysinx P (2007) Stress concentration minimization of 2d filets using X-FEM and level set description. Structural and Multidisciplinary Optimization 33(4-5):425–438, DOI 10.1007/s00158-006-0091-1

Mohamadian M, Shojaee S (2012) Binary level set method for structural topology optimization with MBO type of projection. International Journal for Numerical Methods in Engineering 89(5):658–670

Moon H, Kim C, Wang S (2004) Reliability-based topology optimization of thermal systems considering convection heat transfer. In: Tenth AIAA/ISSMO multidisciplinary analysis and optimization conference. Albany, New York

Osher S, Fedkiw R (2002) Level set methods and dynamic implicit surfaces, vol 153. Springer

Pingen G, Waidmann M, Evgrafov A, Maute K (2010) A parametric level-set approach for topology optimization of flow domains. Structural and Multidisciplinary Optimization 41(1):117–131, DOI 10.1007/s00158-009-0405-1

Rozvany G, Zhou M, Birker T (1992) Generalized shape optimization without homogenization. Structural and Multidisciplinary Optimization 4(3):250–252

Seo JH (2009) Optimal design of material microstructure for convective heat transfer in a solid-fluid mixture. PhD thesis, University of Michigan at Ann Arbor

Sigmund O, Maute K (2013) Topology optimization approaches: A comparative review. Structural and Multidisciplinary Optimization 48(6):1031–1055

Svanberg K (1995) A globally convergent version of MMA without linesearch. In: Proceedings of the First World Congress of Structural and Multidisciplinary Optimization, 28 May - 2 June 1995, Goslar, Germany, pp 9–16

Villanueva CH, Maute K (2014) Density and level set-XFEM schemes for topology optimization of 3-d structures. arXiv preprint arXiv:14016475

Wang M, Zhou S (2004) Phase field: a variational method for structural topology optimization. Computer Modeling in Engineering & Sciences 6(6):547–566

Wang MY, Wang X, Guo D (2003) A level set method for structural topology optimization. Computer Methods in Applied Mechanics and Engineering 192(1-2):227–246, DOI 10.1016/S0045-7825(02)00559-5

Wang S, Wang M (2006) Radial basis functions and level set method for structural topology optimization. International journal for numerical methods in engineering 65(12):2060–2090

Yaji K, Yamada T, Kubo S, Izui K, Nishiwaki S (2014) A topology optimization method for a coupled thermal–fluid problem using level set boundary expressions. International Journal of Heat and Mass Transfer

Yamada T, Izui K, Nishiwaki S (2011) A level set-based topology optimization method for maximizing thermal diffusivity in problems including design-dependent effects. Journal of Mechanical Design 133:031,011–1–031,011–9

Yamasaki S, Nomura T, Kawamoto A, Sato K, Nishiwaki S (2011) A level set-based topology optimization method targeting metallic waveguide design prob-

للاستشارات المنارة

www.manaraa.com

lems. International Journal for Numerical Methods in Engineering 87(9):844–868

Yin L, Ananthasuresh G (2002) A novel topology design scheme for the multi-physics problems of electro-thermally actuated compliant micromechanisms. Sensors and Actuators A: Physical 97:599–609

Yoon G, Kim Y (2005) The element connectivity parameterization formulation for the topology design optimization of multiphysics systems. International journal for numerical methods in engineering 64(12):1649–1677

Yoon GH (2010) Topological design of heat dissipating structure with forced convective heat transfer. Journal of Mechanical Science and Technology 24:1225–1233

Zhu B, Zhang X, Fatikow S (2015) Structural topology and shape optimization using a level set method with distance-suppression scheme. Computer Methods in Applied Mechanics and Engineering 283:1214–1239

A Parameterized Petal Geometry Level set Field

In the petal optimization study of Section 4.2 the level set field is constructed from an overlay of individual level set fields which define the semi-circular base and a sequence of petal shapes swept around the radius. The design variables are: the relative petal width, $\tilde{w}$, the combined petal and base length, $\tilde{h}_t$, the radius of the circular base, $\tilde{h}_b$, and the amplitude of the sinusoidal shaped petal sides, $\tilde{a}$. A single petal and base are depicted in Figure 10. The fields are combined as follows:

$$\phi(\tilde{\mathbf{x}}) = min(\phi_c(\tilde{\mathbf{x}}), \phi_p(\tilde{\mathbf{x}})), \tag{32}$$

where $\phi_c(\tilde{\mathbf{x}})$ is the level set field of the circular base:

$$\phi_c(\tilde{\mathbf{x}}) = |\tilde{\mathbf{x}}| - h_b. \tag{33}$$

The level set field for each petal is conveniently defined in a local coordinate system:

$$\begin{bmatrix} \tilde{x}' \\ \tilde{y}' \end{bmatrix} = \begin{bmatrix} cos\,(\theta) & -sin\,(\theta) \\ sin\,(\theta) & cos\,(\theta) \end{bmatrix} \begin{bmatrix} \tilde{x} \\ \tilde{y} \end{bmatrix}, \tag{34}$$

where the angle of the $j - th$ petal is:

$$\theta = -\frac{\pi}{2} + \frac{\pi}{n_p - 1} j \ , \tag{35}$$

assuming j to be a zero based index. The level set field of each petal describes a cuboid:

$$\phi_p(\tilde{\mathbf{x}}) = \left(\left[\frac{2\tilde{x}_x \tilde{h}_b}{\tilde{w}_w} \right]^p + \left[\frac{\tilde{y}_y \tilde{h}_b}{\tilde{h}_p} \right]^p \right)^{\frac{1}{p}}, \tag{36}$$

where p is the sharpness of the cuboid shape and $\tilde{h}_p$ is the petal length:

$$\tilde{h}_p = \tilde{h}_t - \tilde{h}_b \ . \tag{37}$$

The width, $\tilde{w}_w$, varies in radial direction, i.e. $\tilde{y}'$, and is defined as:

$$\tilde{w}_w = \frac{\pi}{n_p - 1} \left(\tilde{h}_b \,(\tilde{w} - 1) - \tilde{y}' \right). \tag{38}$$

Note the maximum width depends on the number of petals n_p. The axillary coordinates $\tilde{x}_x$ and $\tilde{y}_y$ are defined as functions of the local coordinates $\tilde{x}'$ and $\tilde{y}'$:

$$\tilde{x}_x = \tilde{x}' - sign\,(-\tilde{x}')\,\tilde{a}\tilde{w}_w sin \left(\frac{3}{2}\pi \frac{1}{\tilde{h}_p} \left(\tilde{y}' - \tilde{h}_b \right) \right), \tag{39}$$

$$\tilde{y}_y = \tilde{y}' - \tilde{h}_b \ . \tag{40}$$

www.manaraa.com

Appendix B

Publication [P2]: A Level-set Method for Steady-State and Transient Natural Convection Problems

www.manaraa.com

Structural and Multidisciplinary Optimization manuscript No.
(will be inserted by the editor)

A Level-set Method for Steady-State and Transient Natural Convection Problems

Peter Coffin · Kurt Maute

Received: date / Accepted: date

Abstract This paper introduces a topology optimization method for 2D and 3D, steady-state and transient heat transfer problems that are dominated by natural convection in the fluid phase and diffusion in the solid phase. The geometry of the fluid-solid interface is described by an explicit level set method which allows for both shape and topological changes in the optimization process. The heat transfer in the fluid is modeled by an advection-diffusion equation. The fluid velocity is described by the incompressible Navier-Stokes equations augmented by a Boussinesq approximation of the buoyancy forces. The temperature field in the solid is predicted by a linear diffusion model. The governing equations in both the fluid and solid phases are discretized in space by a generalized formulation of the extended finite element method which preserves the crisp geometry definition of the level set method. The interface conditions at the fluid-solid boundary are enforced by Nitsche's method. The proposed method is studied for problems optimizing the geometry of cooling devices. The numerical results demonstrate the applicability of the proposed method for a wide spectrum of problems. As the flow may exhibit dynamic instabilities, transient phenomena need to be considered when optimizing the geometry. However, the computational burden increases significantly when the time evolution of the flow fields needs to be resolved.

Keywords Topology Optimization · Level Set Methods · Heat Transfer · Incompressible Flow · eXtended Finite Element Method · Nitsche Method

Peter Coffin
Department of Aerospace Engineering,
University of Colorado at Boulder,
Boulder, CO 427 UCB, USA
e-mail: peter.coffin@colorado.edu

K. Maute
Department of Aerospace Engineering,
University of Colorado at Boulder,
Boulder, CO 427 UCB, USA
e-mail: maute@colorado.edu

www.manaraa.com

1 Introduction

Natural convection is the transport of heat via fluid motion driven by temperature dependent buoyancy forces. This mode of energy transport plays an important role in enclosed, sealed or vented systems, such as heat sinks and cooling devices in electronic systems. Heat transfer by natural convection is an attractive concept as it does not require additional mechanical devices, such as fans, and features robustness and simplicity (Baïri et al, 2014). As natural convection is dominated by the interplay of fluid motion and temperature evolution, the design of efficient heat transfer systems is challenging. Design decisions involve selecting a fluid with advantageous physical properties, placing heat sources, and determining the geometry of the enclosure and the internal structures, such as fins. This work presents a computational design optimization method for finding the geometry of thermal devices where the heat transport is dominated by natural convection.

The majority of work on optimizing natural convection systems has considered parametric geometry models with few design variables. For example, Morrison (1992) optimized the thickness and spacing of fins along with the thickness of a back-plane. Bahadur and Bar-Cohen (2005) treated the heat sink height and spacing of pin-fins as design variables. For such particular device geometries, the thermal performance can be approximated by either empirical relations or analytic models. To consider a larger design space and to allow for conceptual design changes in the optimization process, this work considers a topology optimization approach and predicts the thermal response of the system by numerically solving a set of governing partial differential equations.

Topology methods typically describe the geometry of a body and the spatial arrangement of distinct materials within a body via the spatial distribution of a fictitious material. The volume fraction, or density, of the fictitious material is defined as a continuous function of the optimization variables, with the extrema representing distinct material phases. Density-based topology optimization methods, such as the SIMP (Solid Isotropic Material with Penalization) method, interpolate material properties as functions of the density to model geometry changes in the physics model. These methods have been successfully applied to a broad range of problems (Sigmund and Maute, 2013; Deaton and Grandhi, 2014). However, as the optimization process converges to material distributions with intermediate densities, the geometry cannot be clearly identified and the physical behavior is not correctly predicted. The latter issue affects in particular problems where boundary layer phenomena play an important role, such as flows at high Reynolds numbers and convective heat transport. To mitigate these shortcomings of density methods, Level Set Methods (LSMs) have been introduced to topology optimization. Phase boundaries are defined by the iso-contours of one or more level set functions (LSFs) and the material phase is defined by signs of the LSFs. A recent review of LSMs in topology optimization is provided by van Dijk et al (2013). This work considers a LSM for the design of natural convection problems.

To overcome the limitations of empirical and analytical models for convective heat transfer, engineers often describe the heat transfer in the solid by a linear diffusion model and approximate the heat flux at the fluid-solid interface by Newton's Law of Cooling (NLC) which assumes a constant, typically design-independent temperature in the fluid. This model has been used in topology optimization with density methods, for example, by Yin and Ananthasuresh (2002),

المنارة للاستشارات
www.manaraa.com

Moon et al (2004), Yoon and Kim (2005), Bruns (2007), Iga et al (2009), Seo (2009) and Alexandersen (2011), and with LSMs by Yamada et al (2011) and Coffin and Maute (2015). To further improve the prediction of the fluid temperature at the fluid-solid interface, the transport of heat in the fluid by convection and diffusion needs be considered. For low Mach number applications, where compressibility effects in the fluid can be neglected, the fluid temperature field is typically predicted by an advection-diffusion model where the fluid is assumed incompressible and described either by the Navier-Stokes or hydrodynamic Boltzmann equations. For forced convection problems, this class of models has been considered for topology optimization with the density method, for example, by Yoon (2010), Lee (2012), McConnell and Pingen (2012), Matsumori et al (2013), Kontoleontos et al (2013) and Koga et al (2013). LSMs were studied for forced convection problems, for example, by Marck et al (2013), Makhija and Maute (2015) and Yaji et al (2015).

In contrast to forced convection problems, the work on topology optimization for natural convection problems is still in its infancy. Considering natural convection leads to a two-way coupled problem where fluid and thermal fields are interacting. Temperature dependent buoyancy forces drive the flow which in turn alters the temperature field. As the strength of the buoyancy forces and the flow velocities increase, this interaction causes dynamic instabilities in the flow. To date, Alexandersen et al (2014) and Alexandersen (2015) presented the first and only studies of topology optimization for natural convection design problems. They adopted a density method and modeled the thermal response by an advection-diffusion equation at steady-state in two dimensions. The flow is described by the incompressible Navier-Stokes equations with the Boussinesq approximation of the buoyancy forces. The stick condition at fluid-solid interface is enforced via Brinkman penalization and the thermal conductivity is defined as a function of the density. Alexandersen et al (2014) studied 2D problems and observed convergence issues in the flow analysis. This issue is likely due to the steady-state flow model being not able to capture transient flow phenomena. Furthermore, these authors found that intermediate densities may yield large flow velocities and convective fluxes which can be beneficial to the objective, making penalization of intermediate material difficult. Alexandersen (2015) expand this approach to 3D problems at steady-state.

The goal of this study is to mitigate the issues caused by intermediate densities and to expand the work of Alexandersen et al (2014) onto transient problems. Instead of a density method, this work adopts a LSM to provide a crisp representation of material boundaries. Traditionally the level set function is updated via the solution of the Hamilton-Jacobi equation; see, for example, Allaire et al (2002), Wang et al (2003), Allaire et al (2004) and Burger and Osher (2005). Here, parameters of the discretized LSF are defined by explicit functions of optimization variables and the resulting optimization problem is solved by a nonlinear programming (NLP) method. This approach is often referred to as explicit LSM and has been studied, for example, by Wang and Wang (2006), Luo et al (2007) and Pingen et al (2010). Explicit LSMs allow solving problems with multiple constraints by standard NLP schemes.

To consider a broad range of natural convection problems, the flow and temperature fields are considered transient. As the appearance of unsteady phenomena depends on the geometry, which changes in the optimization process, assuming a steady-state response may not be valid throughout the optimization process. Even

المنارة للاستشارات

www.manaraa.com

if the flow and temperature fields of the initial and optimized design converge to a steady-state, designs emerging in the optimization process may trigger unsteady phenomena, leading to convergence issues in the forward analysis. This work models natural convection problems with a transient diffusion model in the solid phase and a transient advection-diffusion model in the fluid phase in two and three dimensions. The flow is described by the transient incompressible Navier-Stokes equations augmented by buoyancy forces modeled by the Boussinesq approximation. To preserve the crispness of the level set geometry description in the coupled model, the governing equations are discretized in space by a generalized formulation of the extended finite element method (XFEM). For an introduction to the XFEM the reader is referred to Fries and Belytschko (2006) and Khoei (2015). The XFEM bypasses the need to introduce fictitious materials and allows enforcing the boundary conditions directly at the fluid-solid interface. The thermal and fluid fields are advanced in time by an implicit time stepping scheme. The unsteady system response is accounted for in the formulation of the optimization and the computation of the design sensitivities. We will study the main characteristics of this approach by numerical examples.

This work is proceeded by Coffin and Maute (2015) where a simplified convection model based on NLC was studied using the explicit LSM-XFEM. A key finding of Coffin and Maute (2015) is that the NLC approximation promotes unrealistically thin fluid channels, as the NLC model over predicts the convective flux. This finding motivates the present work where the temperature in the fluid is resolved. The same explicit LSM-XFEM scheme has been studied for a variety of physical models. Makhija and Maute (2014) study fundamental issues using XFEM in level set topology optimization. Makhija and Maute (2015) study forced convection using a hydrodynamic Boltzmann transport model and Jenkins and Maute (2015) study fluid-structure interaction problems.

The remainder of this paper is organized as follows: In Section 2, the characteristics and the formulation of the optimization problems considered in this study are described. Section 3 presents two approaches for parameterizing and discretizing the LSF. In Section 4, the natural convection model is described, including the XFEM discretization, the time stepping scheme and the associated adjoint sensitivity analysis. Numerical examples are studied in Section 5. The insight gained from these studies are presented in Section 6.

2 The Optimization Problem

Natural convection problems feature a rich set of physical phenomena which need to be accounted for in the formulation of the optimization problem. In this section, we first discuss approaches to characterize natural convection problems and then introduce the formulation of the optimization problem considered in this study.

2.1 Natural Convection Design Problems

The class of design problems considered in this work assumes a solid body immersed in fluid. An external heat flux is applied to the solid body and the fluid

المنارة للاستشارات

www.manaraa.com

is enclosed by walls which are either assumed adiabatic or at a prescribed temperature. This configuration idealizes a broad range of problems where natural convection plays an important role for heat transfer; see Section 1.

The energy transport in the solid phase is due to diffusion and in the fluid phase due to both, diffusion and convection. Diffusion is the process of heat transfer between neighboring material and convection being the heat transfer due to the motion of material. The Rayleigh number is a non-dimensional parameter that characterizes the relative strength of convective to conductive heat transport in natural convection flows and is defined as:

$$Ra = \frac{|\mathbf{g}| \;\; \beta_F \;\; \Delta T \;\; L_c^3}{\nu_F \;\; \alpha_F}, \quad \alpha_F = \frac{\kappa_F}{\rho_F \;\; c_{p,F}} \tag{1}$$

where $|\mathbf{g}|$ is the magnitude of the gravitational acceleration vector, β_F the fluid thermal expansion coefficient, ΔT the temperature difference between the fluid-solid interface and the far-field fluid, L_c the characteristic length, and ν_F the fluid kinematic viscosity. The fluid diffusivity, α_F, is the ratio of the fluid heat conductivity, κ_F, and the product of fluid density, ρ_F, and specific heat capacity, $c_{p,F}$. Large Ra values describe configurations dominated by convective energy transport.

For forced convection problems, the flow behavior is typically characterized by the Reynolds number, Re, that describes the ratio of inertial to viscous forces and is defined as:

$$Re = \frac{v_c L_c}{\nu_F}, \tag{2}$$

where v_c is the characteristic fluid velocity, such as the free-stream velocity or the fluid velocity at an inlet. In this work the characteristic fluid velocity will be taken as the maximum in the domain, defining a maximum local Reynolds number. The behavior of natural convection flows is better characterized by the Grashof number that describes the ratio of buoyancy to viscous forces and is defined as:

$$Gr = \frac{|\mathbf{g}| \, \beta \Delta T L_c^3}{\nu_F^2}. \tag{3}$$

Assuming temperature independent fluid properties, the Rayleigh number increases with Grashof number. For low Rayleigh and Grashof numbers and constant boundary conditions, the flow converges to a steady-state. As the Rayleigh number exceeds a critical value, thermal instabilities emerge and the flow exhibits an unsteady behavior. One example is the flow in a cylinder, its axis aligned with the gravity vector. Holding the top and bottom surfaces at fixed (different) temperatures and assuming adiabatic side walls, for an aspect ratio 1 the flow in the cylinder will exhibit unsteady behavior beginning at Rayleigh numbers of approximately 10^5 (Touihri et al, 1999).

The emergence of instabilities depends on the fluid properties, the boundary conditions, and the geometry of the enclosure as well as internal structures. As the latter evolves during the optimization process, the flow may become unsteady for an intermediate design in the course of the optimization process, while it is steady for the initial design. To consider design problems with a large range of Rayleigh and Reynolds' numbers, it is important to describe a potentially unsteady flow behavior and consider the transient response in the formulation of the optimization problem.

www.manaraa.com

2.2 Formulation of Design Optimization Problem

The design problems studied here have a state-dependent objective, such as minimizing the temperature at a given location in the design domain. As the state variables, i.e. temperature, fluid velocity and fluid pressure, may vary in time, the objective function is defined by an integral over a given time period. The design constraints considered in this work only depend on the LSF which is defined by an explicit function of the optimization variables; see Section 3. These constraints are used to regularize the optimization problem and are defined in Section 5 for the particular problems studied here. This class of optimization problems can be written as follows:

$$\begin{aligned} &min_{\mathbf{s}} \quad Z = \int_{t_1}^{t_2} z\left(\mathbf{s}, \mathbf{u}\left(t\right)\right) \ dt, \\ &\text{s.t.} \quad g_i(\mathbf{s}) \leq 0 \quad i = 1 \ldots N_g \ , \\ &\quad \mathbf{s} \in \mathbf{S} = \left\{ \mathbb{R}^{N_s} | s_i^L \leq s_i \leq s_i^U, \ i = 1 \ldots . N_s \right\} \ , \end{aligned} \tag{4}$$

where the objective Z is the integral of the time dependent function z over the time interval $[t_1, t_2]$. The instantaneous function z depends on the vector of optimization variables $\mathbf{s}$ and the vector of state variables $\mathbf{u}$, which may vary in time, t. The N_s optimization variables s_i are bounded by lower and upper limits, s_i^L and s_i^U. The state variables satisfy the governing equations of the natural convection problem which are described in Section 4.1. The number of inequality constraints is denoted by N_g.

3 Parametrization of Level Set Function

The geometry of a solid body immersed in fluid is defined by the LSF, $\phi(\mathbf{x})$, where $\mathbf{x}$ denotes the vector of spatial coordinates. Assuming that the body consists of one solid phase, a single LSF function is sufficient to describe the spatial distribution of the fluid and solid phases as follows:

$$\begin{aligned} \phi(\mathbf{x}) &< 0, \quad \forall \ \mathbf{x} \in \Omega_S, \\ \phi(\mathbf{x}) &> 0, \quad \forall \ \mathbf{x} \in \Omega_F, \\ \phi(\mathbf{x}) &= 0, \quad \forall \ \mathbf{x} \in \Gamma_{FS}, \end{aligned} \tag{5}$$

where Ω_S is the solid phase, Ω_F the fluid phase and Γ_{FS} the fluid-solid interface.

The level set function can be parametrized to describe a combination of geometric primitives or to allow for the evolution of geometries in the optimization process. Both approaches are used for studying numerical examples in Section 5 and described in the following subsections. In both cases, the LSF is mapped onto the XFEM mesh by evaluating the parametrized LSF at the nodes. Standard finite element shape functions are used to interpolate the LSF value at a point within an element. Here, bi-linear and tri-linear shape functions are used for 2D and 3D problems, respectively. These shape functions permit that an element edge can be intersected by the fluid-solid interface, i.e. $\phi = 0$, at most once. The lines (2D) and faces (3D) spanned by the edge intersection points, $\mathbf{x}_i^\Gamma$, define the fluid-solid interface within a finite element; see Figure 1. The phase, i.e. fluid or solid, of the

المنارة للاستشارات
www.manaraa.com

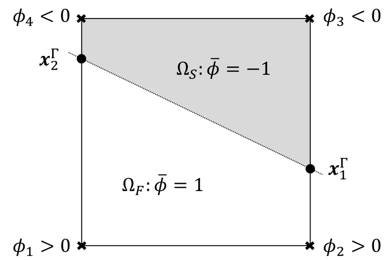

Fig. 1: Construction of interface geometry for intersected elements.

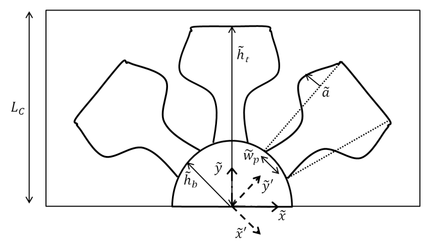

Fig. 2: Configuration of petal design with three petals

subdomains within the elements is determined by the sign of the level set values of the associated finite element nodes. To this end, we introduce an auxiliary level set function $\bar{\phi}$ such that $\bar{\phi} = -1$ in solid subdomains and $\bar{\phi} = 1$ in fluid subdomains. To avoid numerical issues due to the zero level set iso-contour intersecting finite element nodes, nodal level set values that are close to zero, i.e. $\|\phi_i\| \leq 10^{-8}\ h_e$, are set to $\phi_i = 10^{-8}\ h_e$, where h_e is the size of the finite element. Numerical experiments showed that the influence of this perturbation on the optimization results is imperceptible.

The linear interpolation scheme and the construction of the interfaces restrict the geometry resolution of the LSF to the size of a finite element and may cause convergence issues in the optimization process if sub-element-size features are advantageous. This issue has been discussed in Jenkins and Maute (2015) and Coffin and Maute (2015). A regularization scheme to discourage the formation of sub-element-size features has been recently proposed by the authors and is briefly outlined in Subsection 3.3.

3.1 Petal Geometry

To gain insight into the fundamental characteristics of the class of natural convection problems studied here, we first restrict the set of 2D geometries that can emerge in the optimization process. To this end, we parametrize the LSF such that it describes a radial arrangement of petal-like features. A configuration with three petals is depicted in Figure 2. The petals are evenly spaced around a center semicircle of radius $\tilde{h}_b$. The total petal length is defined by $\tilde{h}_t$ and the petal width

www.manaraa.com

by $\tilde{w}_p$, which varies sinusoidally in radial direction with an amplitude $\tilde{a}$. These parameters, i.e. $\tilde{h}_b$, $\tilde{h}_t$, $\tilde{w}_p$, and $\tilde{a}$, can be defined as the optimization variables, s_i, for either each petal individually or uniformly for a group of petals. Note that the petal geometry is defined in non-dimensional form with the height of the design domain being the reference length, i.e. $\mathbf{x} = L_c \tilde{\mathbf{x}}$, where $\tilde{\cdot}$ denotes a non-dimensional parameter.

The petal configuration is defined by the superposition of multiple LSFs, describing the individual petals and the circular base. Each petal is defined in a local coordinate system, $\tilde{\mathbf{x}}'$, that is aligned with the symmetry axis of the petal. The level set value, $\phi(\tilde{\mathbf{x}})$, is defined as:

$$\phi_i(\tilde{\mathbf{x}}) = min_{KS}(\phi_c(\tilde{\mathbf{x}}), \phi_{p,j}(\tilde{\mathbf{x}})), \tag{6}$$

where ϕ_c describes the circular base as:

$$\phi_c = \sqrt{\tilde{x}^2 + \tilde{y}^2} - \tilde{h}_b. \tag{7}$$

The Kreisselmeier-Steinhauser function, min_{KS}, is used to approximate the minimum level set value, ϕ_i, ensuring the differentiability of the formulation with respect to the petal parameters (Kreisselmeier and Steinhauser, 1979). This function is defined as:

$$min_{KS}(\phi) = \frac{-1}{\beta} ln \left(\sum_{k=1}^{N_{LS}} e^{-\beta \phi_k} \right), \tag{8}$$

where the minimum level set value of a set of N_{LS} values is computed with a sharpness parameter, β. The j-th petal is described by $\phi_{p,j}$ which defines a cuboid with curved edges:

$$\phi_{p,j} = \left(\left[\frac{2\tilde{x}_x \tilde{h}_b}{\tilde{w}_w} \right]^p + \left[\frac{\tilde{y}_y \tilde{h}_b}{\tilde{h}_p} \right]^p \right)^{\frac{1}{p}}. \tag{9}$$

The sharpness of the corners is controlled by the parameter p and set to 10 in this study. The petal length, $\tilde{h}_p$, is defined as:

$$\tilde{h}_p = \tilde{h}_t - \tilde{h}_b. \tag{10}$$

The width of the cuboid, $\tilde{w}_w$, varies in radial direction, i.e. $\tilde{y}'$, as follows:

$$\tilde{w}_w = \tilde{w}_p' + \frac{\pi}{N_p - 1} \left(\tilde{y}' - \tilde{h}_b \right). \tag{11}$$

Note that the maximum width depends on the number of petals N_p. The axillary coordinates $\tilde{x}_x$ and $\tilde{y}_y$ introduced in (9) are defined as functions of the local coordinates $\tilde{x}'$ and $\tilde{y}'$:

$$\tilde{x}_x = \tilde{x}' - sign\left(-\tilde{x}'\right)\ \tilde{a}\ \tilde{w}_w\ sin\left(\frac{3}{2}\pi \frac{1}{\tilde{h}_p} \left(\tilde{y}' - \tilde{h}_b \right) \right), \tag{12}$$

$$\tilde{y}_y = \tilde{y}' - \tilde{h}_b\ . \tag{13}$$

The sine function in (12) defines the curvature of the cuboid edges.

www.manaraa.com

3.2 Topology Optimization

To allow for the emergence of a larger set of geometries in the optimization process, the LSF is parametrized by local shape functions defined on a finite element mesh. While this mesh may differ from the XFEM mesh to predict the temperature and flow fields, for simplicity we use the XFEM mesh for parameterizing the LSF in this study.

We assign one optimization variable, $s_i,\ i = 1 \ldots N_n$ to each node of the XFEM mesh, where N_n is the number of nodes. The LSF value of the i-th node, ϕ_i, is defined by an explicit function of the optimization variables as follows:

$$\phi_i = \left(\sum_{j=1}^{N_n} w_{ij} \right)^{-1} \sum_{j=1}^{N_n} w_{ij} s_j, \tag{14}$$

where

$$w_{ij} = max\left(0, (r_f - |\mathbf{x}_i - \mathbf{x}_j|)\right), \tag{15}$$

and r_f is the prescribed filter radius. The filter (14) accelerates the convergence of geometry in the optimization process and may promote (but does not guarantee) smooth shapes of the phase boundaries; see, for example, Kreissl and Maute (2012). Numeric experiments have shown that filter radii of $2.0 - 4.0$ times the element width to yield an effective and efficient smoothing of nodal design variables. Within this range the optimization results do not depend noticeably on choice of r_f.

3.3 Feature Size Control

To discourage the formation of small, sub-element-size features and to control the slope of the LSF near the fluid-solid interface, we introduce the following measure of the spatial LSF gradients:

$$G = \int e^{-\alpha^2} \left(|\nabla\phi| - d\phi_p\right)^2 d\Omega \quad \text{with } \alpha = e_p \ \frac{\phi}{\Delta\phi}, \tag{16}$$

where e_p is the penalization parameter, $d\phi_p$ the desired level set gradient, and $\Delta\phi$ the range of the level values in the design domain, defined as:

$$\Delta\phi = \phi_{max} - \phi_{min}. \tag{17}$$

The gradient measure (16) consists of two terms: The first term becomes vanishingly small far from the zero level set contour and unity nearby; the second term is zero when the level set gradient is equal to the prescribed value. The combination of these two terms penalizes level set gradients that do not match the desired value, $d\phi_p$, along the fluid-solid interface. The value of $d\phi_p$ is typically set to unity to promote uniformly scaled shape sensitives along the phase boundaries; see, for example, Burger and Osher (2005) and van Dijk et al (2013). This functionality of the gradient measure is similar to the one of re-initialization schemes often used in traditional LSMs, which advance the design via the solution of the Hamilton-Jacobi equation.

The authors have recently shown that the gradient measure (16) can be also used to discourage the formation of sub-element-size featured when combined with

المنارة للاستشارات

www.manaraa.com

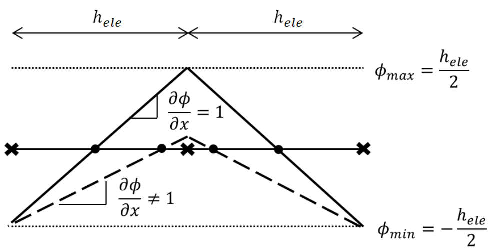

Fig. 3: LSF gradient measure concept, dotted line showing insufficient gradient.

properly selected upper and lower bounds on the optimization variables (Coffin and Maute, 2015). This concept is illustrated in Figure 3. Restricting the level set values to $\pm h_{ele}/2$, where h_{ele} is the element size, the minimum feature size is h if the gradient of the LSF is one. The reader is referred to Coffin and Maute (2015) for further details. In Section 5, an upper limit on the gradient measure (16) is imposed to regularize the optimization problems.

4 Analysis

The main challenge in optimizing the topology of natural convection problems is the modeling and numerical prediction of the temperature and flow fields. In this section, we present the weak form of the governing equations, outline the spatial and temporal discretization schemes, and summarize the main steps of the adjoint sensitivity analysis.

4.1 Governing Equations

In this study, we describe natural convection flows by coupling an advection-diffusion equation, which describes the transport of thermal energy, and the incompressible Navier-Stokes equations, which describe the transport of momentum. The buoyancy forces are modeled by the Boussinesq approximation. While this fluid model is only valid for low Mach number flows, it describes well a broad range of problems relevant for engineering design. The heat transfer in the solid phase is described by a linear diffusion model. Fluid and solid models are coupled at the fluid-solid interface through temperature and heat flux continuity conditions. The residual weak form of the governing equations in the fluid and solid phases are summarized subsequently.

4.1.1 Incompressible Navier-Stokes Equations

The residual of the weak form of the incompressible Navier-Stokes equations, R^F, is decomposed into volumetric and surface contributions:

$$R^F = R^F_{\Omega} + R^F_{stab} + R^F_{\Gamma_{ext}} + R^F_{\Gamma_F S} = 0 \, , \tag{18}$$

المنارة للاستشارات
www.manaraa.com

where R^F_Ω and R^F_{stab} are the residuals of the volumetric non-stabilized and stabilized contributions, $R^F_{\Gamma_{ext}}$ is the residual of contribution from external boundaries, and $R^F_{\Gamma_{FS}}$ is the residual of the fluid-solid interface conditions. The stabilization term, R^F_{stab}, depends on the discretization scheme and is defined in Section 4.2. For the problems considered in this study, the contributions form external boundaries vanish as the fluid velocities are set to zero along the walls enclosing the flow domain.

The non-stabilized volumetric contributions are:

$$\begin{aligned} R^F_\Omega = & \int_{\Omega_F} \Psi_i \ \rho_F \ \left(\frac{\partial v_i}{\partial t} + v_j \ \frac{\partial v_i}{\partial x_j} \right) \ d\Omega \\ & + \int_{\Omega_F} \frac{1}{2} \left(\frac{\partial \Psi_i}{\partial x_j} + \frac{\partial \Psi_j}{\partial x_i} \right) \ \sigma_{ij} \left(\mathbf{v}, p \right) \ d\Omega \\ & + \int_{\Omega_F} \Psi_i \ \rho_F \ g_i \ \left(1 - \beta_F \ \left[T_F - T_0 \right] \right) d\Omega \\ & + \int_{\Omega_F} \eta \ \frac{\partial v_i}{\partial x_i} \ d\Omega \ , \end{aligned} \tag{19}$$

where v_i is the velocity vector, p the pressure, T_F the temperature, and σ_{ij} the stress tensor of the fluid. The vector Ψ_i denotes admissible test functions for the momentum equations, and η is the test function of the incompressibility condition. The gravity acceleration vector is denoted by g_i and T_0 is the reference temperature. In this form the reference temperature drives the magnitude of buoyancy force through the entire domain. In a closed box, the magnitude of reference temperature will lead to changes in the magnitude of mean pressure in the domain and will not impact the fluid flow velocities. The fluid stress is defined as:

$$\sigma_{ij} \left(\mathbf{v}, p \right) = -p \delta_{ij} + \mu \ \left(\frac{\partial v_i}{\partial x_j} + \frac{\partial v_j}{\partial x_i} \right) \ , \tag{20}$$

where μ is the dynamic viscosity of the fluid.

We enforce weakly the stick condition at the fluid-solid interface by a Nitsche's method (Nitsche, 1975). The formulation adopted here is described by Schott et al (2014) and is written as:

$$\begin{aligned} R^F_{\Gamma_{FS}} = & - \int_{\Gamma_{FS}} \Psi_i \ \sigma_{ij} \left(\mathbf{v}, p \right) \ n^F_j \ d\Gamma \\ & - \int_{\Gamma_{FS}} \sigma_{ij} \left(\mathbf{\Psi}, \eta \right) \ v_i \ n^F_j \ d\Gamma \\ & + \gamma_F \ \int_{\Gamma_{FS}} \Psi_i \ v_i \ d\Gamma \ , \end{aligned} \tag{21}$$

where n^F_j is the normal on the interface pointing into the solid phase and γ^F is a penalty parameter.

4.1.2 Advection-Diffusion Equation

The energy transport in the fluid phase is described by an advection-diffusion equation. Setting the advective velocity to zero, this equation simplifies to a diffusion equation which is used to model the conduction in the solid phase. Similar to the Navier-Stokes equations discussed previously, the weak form of the advection-diffusion equation is decomposed into volumetric and surface contributions as follows:

$$R^{T_P} = R^{T_P}_\Omega + R^{T_P}_{stab} + R^{T_P}_{\Gamma_{ext}} + R^{T_P}_{\Gamma_{FS}} = 0 \ , \tag{22}$$

المنارة للاستشارات

www.manaraa.com

where P denotes the phase, i.e. fluid or solid. The stabilized volumetric contribution, $R^{T_P}_{stab}$, is discussed in Section 4.2. The non-stabilized volumetric contribution, $R^{T}_{k,\Omega}$, is:

$$\begin{aligned} R^{T_P}_{\Omega} = &\int_{\Omega_P} \zeta_P \; \rho_P \; c_{p,P} \; \left(\frac{\partial T_P}{\partial t} + v^P_j \frac{\partial T_P}{\partial x_j} \right) \; d\Omega \\ &+ \int_{\Omega_P} \frac{\partial \zeta_P}{\partial x_i} \; J^P_i \left(T_P \right) \; d\Omega \;, \end{aligned} \tag{23}$$

where ζ_P is an admissible test function and J^P_i the diffusive heat flux. Note the advective velocity v^P_i is the fluid velocity v_i in $\Omega_k = \Omega_F$ and vanishes in the solid phase. Assuming isotropic diffusion in both fluid and solid phase, the heat flux is:

$$J^P_i \left(T_P \right) = \kappa_P \; \frac{\partial T_P}{\partial x_i} \;. \tag{24}$$

The contribution from the external boundaries, $R^{T_P}_{\Gamma_{ext}}$, is due to applied heat surface fluxes and is defined as:

$$R^{T_P}_{\Gamma_{ext}} = \int_{\Gamma^q_P} \zeta_P \; q_P \; d\Gamma \;, \tag{25}$$

where Γ^q_P denotes the surface of phase P at which the surface flux q_P is applied.

The continuity of the temperature field and the surface fluxes at the fluid-solid interface is enforced weakly using Nitsche's method. Following the work of Dolbow and Harari (2009), the surface contributions R^{T_F} and R^{T_S} are defined through the following integrals:

$$\begin{aligned} R^{T_F} + R^{T_S} = &- \int_{\Gamma_{FS}} \langle \zeta \rangle \; \left\{ J_i \left(T_F, T_S \right) \right\} \; n^F_i \; d\Gamma \\ &- \int_{\Gamma_{FS}} \left\{ J_i \left(\zeta_F, \zeta_S \right) \right\} \; n^F_i \; \langle T \rangle \; d\Gamma \\ &+ \gamma_T \; \int_{\Gamma_{FS}} \langle \zeta \rangle \; \langle T \rangle \; d\Gamma, \end{aligned} \tag{26}$$

with

$$\langle z \rangle = z_F - z_S \qquad \text{and} \qquad \left\{ J_i \left(z_F, z_S \right) \right\} = w^F \; J^F_i \left(z_F \right) + w^S \; J^S_i \left(z_S \right) \;, \tag{27}$$

where γ_T is a penalty parameter and w^F and w^S are weights such that $w^F + w^S = 1$.

4.2 Spatial Discretization

The governing equations in the fluid and solid phase are discretized in space by the XFEM. The XFEM augments the standard finite element interpolation by additional enrichment functions to capture discontinuities in either the state variables or their spatial gradients within an element. Depending on the type of discontinuity, different enrichment schemes are applied (Fries and Belytschko, 2010). The particular approach used in this study is adopted from Makhija and Maute (2014), Kreissl and Maute (2012), Lang et al (2014), Makhija and Maute (2015), who considered linear elastic, incompressible Navier-Stokes, diffusion, and advection-diffusion problems, respectively.

The XFEM is used to approximate the fluid velocity and pressure fields as well as the temperature fields in the solid and fluid phases within finite elements that

المنارة للاستشارات
www.manaraa.com

are intersected by the fluid-solid interface, i.e. the zero level set iso-contour. With u representing one of these state variables, a Heaviside enrichment strategy is used to discretize the governing equations. The approximation of u within an element, $\hat{u}$, is defined as:

$$\hat{u}(\mathbf{x}) = \sum_{m=1}^{M} \Bigg(H(-\bar{\phi}(\mathbf{x})) \sum_{i \in I} N_i(\mathbf{x})\ \delta_{mk}^{i,F}\ u_{i,m}^{F} \\ + H(\bar{\phi}(\mathbf{x})) \sum_{i \in I} N_i(\mathbf{x})\ \delta_{mn}^{i,S}\ u_{i,m}^{S} \Bigg) \tag{28}$$

where I is the set of all elemental nodes, $N_i(\mathbf{x})$ the nodal basis functions, M the number of enrichment levels, and $u_{i,m}^F$ and $u_{i,m}^S$ are the degrees of freedom of enrichment level m at node i in the fluid and solid phases, respectively. To satisfy the partition of unity principle, no more than one degree of freedom per node is used to interpolate the solution at a point in the element. The active degrees of freedom at the i-th node are denoted by k and n in fluid and solid phases, respectively, and $\delta_{ab}^{i,P}$ for $P = [F, S]$ is the Kronecker delta. The Heaviside function, $H(z)$, turns on and off the interpolation for the particular phase and is defined as:

$$H(z) = \begin{cases} 1 & z > 0 \\ 0 & z \leq 0 \end{cases} . \tag{29}$$

For each phase, multiple enrichment levels, i.e. sets of shape functions, may be necessary to interpolate the state variables in multiple, physically disconnected regions of the same phase; see Makhija and Maute (2014), Terada et al (2003), and Tran et al (2011). This generalization prevents spurious coupling between disconnected regions of the same phase. The reader is referred to Makhija and Maute (2014) for details on the particular approach used here. To accurately integrate the weak form of the static equilibrium equations by Gauss quadrature, intersected elements are decomposed into triangles in 2D and tetrahedrons in 3D.

The convective terms in the incompressible Navier-Stokes and advection-diffusion equations may cause spurious node-to-node velocity oscillations. Furthermore, we interpolate both the fluid velocity and pressure by bi-linear shape functions in 2D and tri-linear shape functions in 3D. This equal-order interpolation gives rise to spurious pressure oscillations. To prevent these numerical instabilities, we augment the incompressible Navier-Stokes by the Streamline Upwind Petrov Galerkin (SUPG) and Pressure Stabilized Petrov Galerkin (PSPG) stabilization (Tezduyar et al, 1992), yielding the following volumetric contribution to (18):

$$R_{stab}^{F} = \sum_{e=1}^{N_e^F} \int_{\Omega_{F,e}} \left(\tau_{SUPG}^{v}\ v_j\ \frac{\partial \Psi_i}{\partial x_j} + \frac{1}{\rho_F}\ \tau_{PSPG}\ \frac{\partial \eta}{\partial x_i} \right) \\ \left(\rho_F \left(\frac{\partial v_i}{\partial t} + v_j\ \frac{\partial v_i}{\partial x_j} \right) - \frac{\partial \sigma_{ij}(\mathbf{v},p)}{\partial x_j} + \rho_F\ g_i\ \left(1 - \beta_F\ \left[T_F - T_0\right]\right) \right)\ d\Omega, \tag{30}$$

where N_e^F denotes the number of elements in the fluid phase. The stabilization parameters τ_{SUPG}^{v} and τ_{PSPG} are given by Tezduyar et al (1992). The advection-diffusion equation in the fluid phase is stabilized by the following SUPG term:

$$R_{stab}^{T_F} = \sum_{e=1}^{N_e^F} \int_{\Omega_{F,e}} \frac{\tau_{SUPG}^{T}}{\rho_F\ c_{p,F}}\ v_i \frac{\partial \zeta}{\partial x_i}\ \left(\rho_F\ c_{p,F}\ \left(\frac{\partial T_F}{\partial t} + v_i \frac{\partial T_F}{\partial x_i} \right) - \frac{\partial J_i^F}{\partial x_i} \right)\ d\Omega\ , \tag{31}$$

where the stabilization parameter τ_{SUPG}^{T} is defined in Franca et al (1992).

المنارة للاستشارات
www.manaraa.com

4.3 Time Integration Scheme

The XFEM discretization yields the following semi-discrete form of the governing equations:

$$\mathbf{R}_u\left(\mathbf{u},\dot{\mathbf{u}}\right)=\mathbf{0}\ , \tag{32}$$

where the vector $\mathbf{u}$ collects the degrees of freedom of the fluid velocity, pressure, and temperature fields, as well as the temperature field in the solid; its time derivative is denoted by $\dot{\mathbf{u}}$. We discretize the governing equations in time by an implicit Euler backward scheme:

$$\dot{\mathbf{u}}^{(n)}=\frac{\mathbf{u}^{(n)}-\mathbf{u}^{(n-1)}}{\Delta t^{(n)}},\quad n=1\ldots N_t\ , \tag{33}$$

where n is the time index, $\Delta t^{(n)}$ the time step size, and N_t the number of time steps.

At time step $n=0$, the initial conditions, $\mathbf{u}_0$, are satisfied for all state variables such that:

$$\mathbf{R}_u^{(0)}=\mathbf{u}^{(0)}-\mathbf{u}_0\ . \tag{34}$$

For all time steps $n>0$, the equilibrium at the time step (n) is satisfied by solving the nonlinear system $\mathbf{R}_u^{(n)}=\mathbf{0}$ via Newton's method. To this end the system is linearized at $\mathbf{u}^{(n)}$, yielding the following contributions to the Jacobian:

$$\mathbf{J}_{u^{(n)}}^{(n)}=\left.\frac{\partial\mathbf{R}_u^{(n)}}{\partial\mathbf{u}^{(n)}}\right|_{u^{(n)}}+\left.\frac{\partial\mathbf{R}_u^{(n)}}{\partial\dot{\mathbf{u}}^{(n)}}\right|_{u^{(n)}}\frac{1}{\Delta t^{(n)}} \tag{35}$$

Note that due to the SUPG and PSPG stabilization terms, the second term in the above equation depends on the solution $\mathbf{u}^{(n)}$. We compute derivatives in (35) based on the analytically differentiated finite element formulations.

4.4 Sensitivity Analysis

The objective functions considered in this study can be written in discretized form as:

$$Z=\sum_{n=N_t^1}^{N_t^2} z^{(n)}\left(\mathbf{s},\mathbf{u}^{(n)}\right), \tag{36}$$

where the time steps N_t^1 and N_t^2 correspond to the times interval $[t_1,t_2]$ defined in (4). The derivatives of the objective function with respect to the optimization variables are computed by the adjoint method. To this end, we adopt the discrete formulation for nonlinear fluid and coupled systems of Kreissl and Maute (2011) and Golmon et al (2012). The main steps of the computational procedure are summarized subsequently.

The derivative of the objective function with respect to the optimization variable s_i is decomposed into an explicit and an implicit term such that:

$$\frac{dZ}{ds_i}=\frac{\partial Z}{\partial s_i}+\sum_{n=N_t^1}^{N_t^2}\frac{\partial z^{(n)}}{\partial\mathbf{u}^{(n)}}^T\frac{\partial\mathbf{u}^{(n)}}{\partial s_i}\ . \tag{37}$$

www.manaraa.com

The explicit term is evaluated by differentiating Z first with respect to the nodal level set values, ϕ_j. For convenience these derivatives are evaluated by finite differences. The resulting vector, $(\partial Z/\partial \phi_j)$, is then post-multiplied by the derivative of the nodal level set values with respect to the optimization variables, $(\partial \phi_j/\partial s_i)$, differentiating the explicit expressions introduced in Sections 3.1 and 3.2. The same procedure is used to compute the derivatives of the constraints in (4), as they do not depend on the state variables in this study.

The implicit term in (37) is computed by the adjoint method as follows:

$$\sum_{n=N_t^1}^{N_t^2} \frac{\partial z^{(n)}}{\partial \mathbf{u}^{(n)}}^T \frac{\partial \mathbf{u}^{(n)}}{\partial s_i} = \sum_{n=0}^{N_t^2} \lambda^{(n)^T} \frac{\partial \mathbf{R}_u^{(n)}}{\partial s_i} , \tag{38}$$

where $\lambda^{(n)}$ are the adjoint states at time step n. Note that the scalar product of the adjoint vector and the derivative of the residual $\mathbf{R}_u^{(n)}$ is summed from the initial time step through $n = N_t^2$. The adjoint state are computed by integrating the adjoint equations backward in time as follows:

$$\begin{aligned} \left(\mathbf{J}_{u^{(n)}}^{(n)}\right)^T \lambda^{(n)} = &-\tfrac{\partial z^{(n)}}{\partial \mathbf{u}^{(n)}} \\ &+ \tfrac{1}{\Delta t^{(n+1)}} \left.\tfrac{\partial \mathbf{R}_u^{(n+1)}}{\partial \dot{\mathbf{u}}^{(n+1)}}\right|_{u^{(n+1)}}^T \lambda^{(n+1)} , \end{aligned} \tag{39}$$

for $n = N_t^2 \ldots 0$ and $\lambda^{(N_t^2+1)} = \mathbf{0}$. In this work, we compute the derivative of the objective function components with respect to the state variables, $\partial z^{(n)}/\partial \mathbf{u}^{(n)}$, analytically. The derivatives of the residual with respect to the design variables, $\partial \mathbf{R}_u^{(n)}/\partial s_i$, are computed by finite difference. Note that only the residuals of intersected elements need to be considered as the derivatives of non-intersected elements vanishes.

The differentiation of the residual of intersected elements with respect to the optimization variables deserves particular attention. The derivative of an elemental residual, R_e^n, at time step n can be conveniently decomposed as follows:

$$\frac{\partial R_e^n}{\partial s_i} = \sum_{j=1}^{N_n^e} \sum_{k=1}^{N_n^\Gamma} \frac{\partial R_e^n}{\partial \mathbf{x}_k^\Gamma} \frac{\partial \mathbf{x}_k^\Gamma}{\partial \phi_j} \frac{\partial \phi_j}{\partial s_i}, \tag{40}$$

where N_n^e is the number of nodes and N_n^Γ the number of intersection points per element. The first term in the double sum of (40) describes the change of the elemental residual due to a change in the interface geometry which is defined by the position, $\mathbf{x}_k^\Gamma$, of the intersection points along the element edges; see Section 3. The second term represents the dependence of $\mathbf{x}_k^\Gamma$ on the level set value, ϕ_j, at the finite element nodes. The last term captures the explicit dependence of ϕ_j on the optimization variables. The decomposition (40) illustrates clearly that the proposed LSM essentially uses shape derivatives to update the design in the optimization process.

Assuming that $\phi_j(s_i)$ is smooth, the partial derivatives in (40) exist for all values of s_i, except for $\phi_j = 0$. In this case, for an infinitesimal perturbation of ϕ_j, edge intersection points may emerge or vanish and a subset of degrees for freedom, $u_{i,m}^P$ with $P = [F, S]$, may become active or inactive, as defined by the Kronecker delta, $\delta_{ab}^{i,P}$, in (28). To mitigate these issues, we construct the nodal

www.manaraa.com

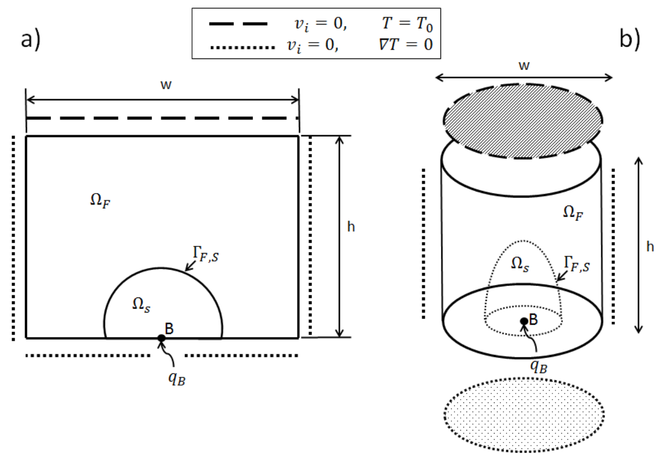

Fig. 4: Configurations of the design problem in (a) two and (b) three dimensions.

level set values such that $\|\phi_j\| > 0$; see Section 3. Furthermore, we evaluate the derivative $\left(\partial R_e^n / \partial \mathbf{x}_k^\Gamma \cdot \partial \mathbf{x}_k^\Gamma / \partial \phi_j\right)$ in the direction which does not alter the sign of ϕ_j. In this work, we compute $\left(\partial R_e^n / \partial \mathbf{x}_k^\Gamma \cdot \partial \mathbf{x}_k^\Gamma / \partial \phi_j\right)$ by a finite difference method. If the sign of a nodal level set value does change due to perturbation $\pm \Delta\phi_j$, a central difference scheme is chosen; otherwise a forward or backward difference scheme is used, depending on the perturbation direction that does not yield a sign change. Numerical studies for a broad range of problems rendered this finite differencing approach sufficiently accurate and computationally efficient.

5 Example Problems

In this work we study the characteristics of the proposed LSM approach for steady-state problems in 2D and 3D. A transient problem is studied in 2D only due to constraints on computational resources.

The configurations of the 2D and 3D design problems are shown in Figure 4. In 2D the design domain is a rectangle of width w and height h. In 3D a cylinder of diameter w and height h forms the design domain. In both configurations, a heat flux q_B is applied at point B which is guaranteed to be surrounded by a sphere of solid phase with radius r_{BS}. The temperature on the top surface of the design domains is fixed to T_0. The side and bottom walls are adiabatic. The fluid velocity at the walls and the fluid-solid interface is zero. We assume the properties of air for the fluid phase and the ones of aluminum for the solid phase. The material parameters are summarized in Table 1. The magnitude of the heat flux and the dimensions of the design domains are varied to yield either a steady-state or transient flow response.

The goal of the design problem is to find the geometry of an internal solid structure such that the average temperature at point B, T_B, within the time

www.manaraa.com

Table 1: Material properties for example problems.

	Value
Gravity	$g = 9.81 \frac{m}{s^2}$
Volumetric thermal expansion	$\alpha_{TE} = 3.43 \times 10^{-3} \frac{1}{K}$
Fluid dynamic viscosity	$\mu_F = 1.511 \times 10^{-5} Pa \cdot s$
Fluid density	$\rho_F = 1.205.0 \frac{kg}{m^3}$
Fluid specific heat	$c_{p,F} = 1005.0 \frac{J}{kgK}$
Fluid diffusivity	$\kappa_F = 0.0257.0 \frac{W}{mK}$
Solid density	$\rho_S = 2700.0 \frac{kg}{m^3}$
Solid specific heat	$c_{p,S} = 910.0 \frac{J}{kgK}$
Solid diffusivity	$\kappa_S = 237.0 \frac{W}{mK}$
Reference temperature	$T_0 = 1.0K$

$[t_1, t_2]$ is minimum. To prevent the trivial solution of an all solid design domain, the volume of the solid phase, V_S, is constrained to be less than or equal to a maximum volume, c_v. To promote smooth shapes and to discourage the formation of small geometric features, we impose a constrained on the perimeter, with c_{pe} denoting the maximum feasible perimeter. To suppress the formation of sub-element-size features, we also impose a constraint on the level set gradient measure described in Section 3.3, with c_g being the upper limit. This optimization problem can be written as follows:

$$
\begin{aligned}
min_{\mathbf{s}} \quad & Z = \frac{1}{N_t^{12}} \sum_{n=N_t^1}^{N_t^2} T_B^{(n)}, \\
\text{s.t.} \quad & V_S - c_v \leq 0 \\
& P - c_{pe} \leq 0 \\
& G - c_g \leq 0 \\
& \mathbf{s} \in \mathbf{S} = \left\{ \mathbb{R}^{N_s} | s_i^L \leq s_i \leq s_i^U, \; i = 1....N_s \right\} ,
\end{aligned}
\tag{41}
$$

where $N_t^{12} = N_t^2 - N_t^1$ is the number of time steps in the time interval of interest. For steady-state problem, $N_t^{12} = 1$. Numerical studies have shown that the constraint on the gradient measure is only needed for the 3D problem considered here. Therefore, this constraint is omitted for the 2D problems.

The design domains are discretized in space by bilinear quadrilateral elements (2D) and hexahedral, trilinear elements (3D). To enforce the stick condition at the fluid-solid interface we set the fluid penalty parameter to $\gamma_F = 10^4$; see (21). To enforce the temperature continuity the temperature penalty parameter is set to $\gamma_T = 100.0$ and the flux averaging weights to $w^S = w^F = 0.5$; see (26) and (27). For the transient case, the flow and temperature fields are advanced in time by an implicit Euler backward scheme; see Section 4.3. The resulting systems of nonlinear residual equations are solved by a damped Newton-Raphson method. The linear sub-problems of both the forward and the sensitivity analysis are solved

www.manaraa.com

by either a sequential or parallel direct solvers, depending on the problem size. We use UMFPACK for 2D problems and MUMPS for the 3D problem (Davis, 2004; Amestoy et al, 1998).

The Globally Convergent Method of Moving Asymptotes (GCMMA) of Svanberg (2002) is used to solve the optimization problem. The GCMMA parameters are: relative step size, 0.01; minimum asymptote adaptivity, 0.5; initial asymptote adaptivity, 0.7; maximum adaptivity, 1.43; and constraint penalty, 50. The optimization problem is considered converged if the change of the objective function relative to the initial objective value is less than 10^{-6} and the constraints are satisfied.

The numerical studies presented in the remainder of this section are organized as follows: First we study a steady-state configuration in 2D, restricting the design freedom to a petal geometry. This study illustrates the influence of imposing symmetry conditions on the design. The same configuration is considered with a finite element discretization of the level set function, illustrating the influence of the increased design freedom and the choice of the initial design. A 2D configuration yielding unsteady flow is then considered to understand the influence of a sup-critical Grashof number on the resulting design geometry. Finally, a 3D steady state design problem is considered.

To characterize the flow and temperature fields of the initial and optimized designs, we report on the Rayleigh and Grashof numbers as well as on the maximum local Reynolds number. The domain height is used as the characteristic length, L_c; the maximum difference between the temperature at the top surface and at point B, i.e. $T_B - T_0$, over all time steps is used as characteristic temperature difference, ΔT. The local Reynolds number is computed with respect to the maximum local fluid velocity, i.e. $v_c = max_{\Omega_F} |\mathbf{v}|$.

5.1 2D Petal Geometry Optimization

First, we restrict the design freedom to the petal geometry described in Subsection 3.1 and perform parametric optimization to understand the main characteristics of the design problem. In particular, we study the influence of imposing symmetry conditions on the design. To this end, we consider three variations of a 5-petal layout. In option O1, we enforce the same geometry for each individual petal yielding a total of four optimization variables: $\tilde{h}_b$, $\tilde{h}_t$, $\tilde{w}_p$ and $\tilde{a}$. For option O2, we only enforce symmetry about the vertical axis. Using a uniform base height for all petals, option O2 yields $1 + 3 \times 3$ optimization variables. Finally, in option O3, each petal is allowed a unique geometry, yielding $1 + 5 \times 3$ optimization variables. The initial design for all configurations is shown in Figure 5. The initial values and the upper and lower bounds of the design parameters are given in Table 2. Note that these bounds allow the petals to overlap and thus the topology to change in the optimization process.

The dimension of the design domain and the magnitude of the heat flux is chosen such that a stable steady-solution of the natural convection problem exists throughout the optimization process. At the initial design, the Rayleigh number is $Ra = 6,050$, the Grashof number $Gr = 10,200$, the maximum local Reynolds number $Re_{max} = 10.0$. The problem parameters are summarized in Table 3.

المنارة للاستشارات
www.manaraa.com

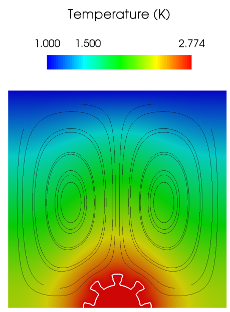

Fig. 5: Initial design for 2D petal geometry optimization.

Table 2: Initial values and bounds of design parameters for 2D petal geometry optimization.

Value	Initial	Minimum	Maximum
Base Length, $\tilde{h}_b$	0.21	0.15	0.25
Total Length, $\tilde{h}_t$	0.31	0.0	0.9
Petal Width, $\tilde{w}_p$	0.21	0.0	0.9
Side Variation, $\tilde{a}$	0.0	-0.4	0.4

Table 3: 2D optimization parameters.

Parameter	Value
Domain height	$h = 0.030m$
Domain width	$w = 0.030m$
Number of elements	$80 \times 80 = 6400$
Heat flux	$q_B = 5.000 \times 10^{-2}W$
Volume constraint	$c_v = 3.93 \times 10^{-5}m^3$
Perimeter constraint	$c_{pe} = 3.14 \times 10^{-2}m^2$

Temperature contour plots with stream lines of the final designs of the three options O1-3 are shown in Figure 6. The temperatures at point B, the volume, and the perimeter of the optimized designs are given in Table 4. The diffusive and convective contribution to the total heat transport are shown in Figure 7. The diffusive flux, J^{diff}, in the fluid domain is defined as:

$$J_i^{diff} = -\kappa_F \frac{\partial T}{\partial x_i}, \tag{42}$$

while the advective flux, q^{adv}, is defined as:

$$J_i^{adv} = c_{p,F} \rho_F \; \Delta T v_i, \tag{43}$$

المنارة للاستشارات

www.manaraa.com

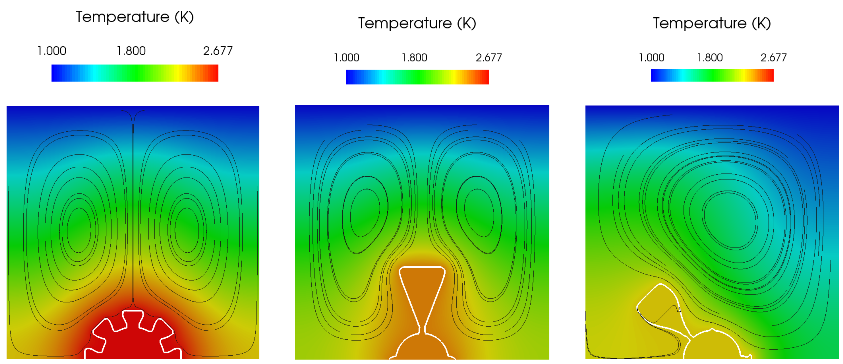

Fig. 6: Temperature contour plots with streamlines of the final designs for petal geometry optimization: option O1 (left), O2 (middle), O3 (right).

Table 4: 2D petal geometry optimization results.

Design	Initial Design	Option O1 - Final Design	Option 02 - Final Design	Option O3 - Final Design
T_B $[K]$	2.77	2.68	2.43	2.29
Volume $[m^3]$	2.22×10^{-5}	3.81×10^{-5}	3.93×10^{-5}	3.92×10^{-5}
Perimeter $[m^2]$	2.44×10^{-2}	3.14×10^{-2}	3.14×10^{-2}	3.12×10^{-2}
Rayleigh	6.05×10^{3}	5.72×10^{3}	4.89×10^{3}	4.39×10^{3}
Grashof	1.02×10^{4}	9.68×10^{3}	8.27×10^{3}	7.44×10^{3}
Local Reynolds	1.00×10^{1}	7.78	4.92	1.68×10^{1}

where ΔT is the difference between the local, T, and reference, T_0, temperatures.

Since the convective flux increases with the area of the fluid-solid interface, the perimeter of all designs is either equal or close to the maximum feasible value. Similarly, the designs take up (almost) all of the allowable solid volume in order to extend the solid phase toward the cold top surface. As expected, the objective improves, i.e. the temperature T_B decreases, with increasing design freedom. Option O3 takes advantage of the design freedom and yields an asymmetric design, although the setup of the design problem is symmetric. Comparing the heat flux contributions of the optimized designs suggests that the asymmetric design solution increases in particular the convective energy transport. The differences in convective flux are also reflected in the differences in the flow velocities shown in Figure 8. As the Rayleigh number of the problem is lowered the benefits from an asymmetric design decrease and the optimization process converges to a symmetric design. This tendency was observed when lowering the product $(\rho_F \; c_{p,F})$ by a factor 1000.0; the results of this study are not shown here as they do not provide fundamentally new insights.

المنارة للاستشارات
www.manaraa.com

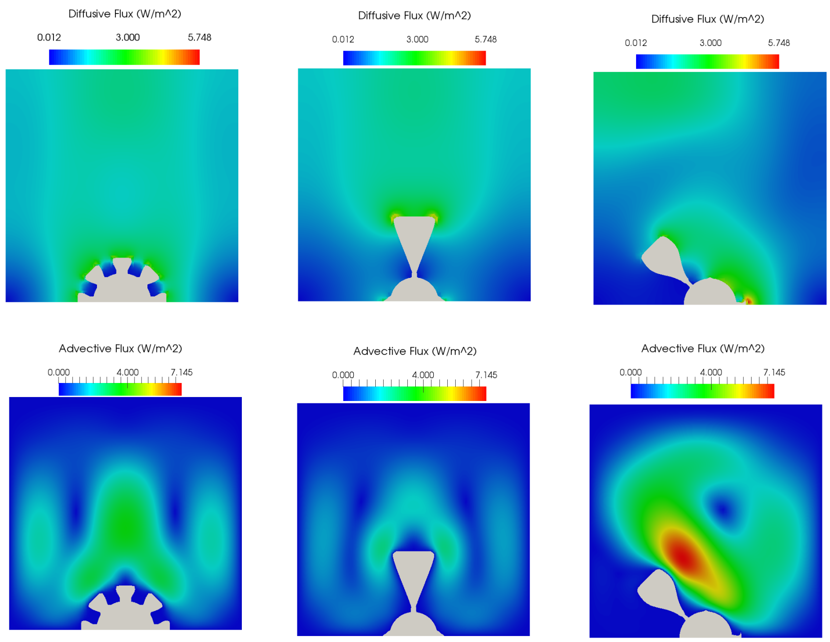

Fig. 7: Diffusive (top) and advective (bottom) fluxes for petal geometry optimization: option O1 (left), O2 (middle), O3 (right).

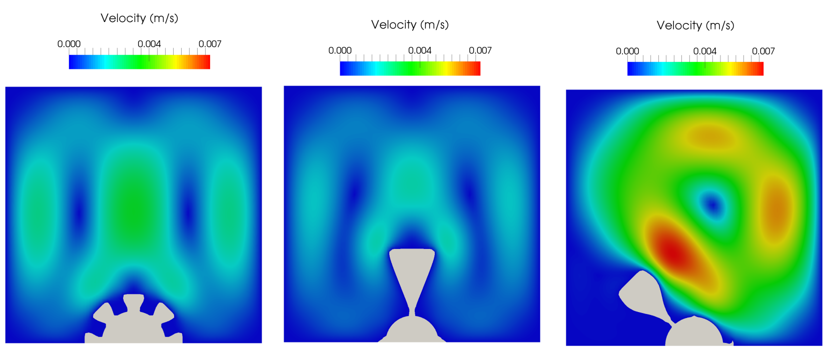

Fig. 8: Magnitude of fluid velocities for petal geometry optimization: option O1 (left), O2 (middle), O3 (right).

المنارة للاستشارات

www.manaraa.com

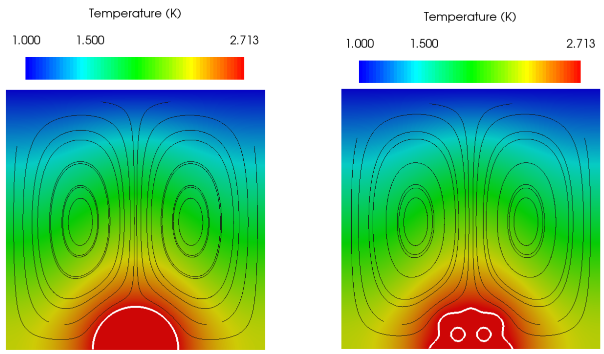

Fig. 9: Temperature contour plots with streamlines of initial designs for 2D steady-state topology optimization: circular (left) and inclusions (right).

614 5.2 2D Steady-State Topology Optimization

615 We consider the same steady-state configuration of Section 5.1 but now study 616 a finite element parameterization of the level set function; see Section 3.2. We 617 compare the optimization results for a symmetric and non-symmetric problem 618 setup. To study the influence of the initial design on the optimization results, we 619 consider the two initializations of the level set function shown in Figure 9: one 620 consisting of a simple half-circle of radius 0.005, the second imposing a grid of 621 cuboid fluid inclusions over the same solid circle.

622 The problems parameters are given in Table 3. The radius of the circle of solid 623 phase around point B is $r_{BS} = 10^{-3}\ m$. The smoothing radius of the linear filter 624 (15) is $r_f = 1.440 \times 10^{-3}\ m$. To enforce a symmetric design we define the nodal 625 level set functions at corresponding nodes by the same optimization variables.

626 For the initial half-circle design the Rayleigh number is $Ra = 5,900$, the 627 Grashof number $Gr = 9,900$, and the maximum local Reynolds number $Re_{max} =$ 628 9.0; for the the half-circle with inclusions the Rayleigh number is $Ra = 6,000$, 629 the Grashof number $Gr = 10,000$, and the maximum local Reynolds number 630 $Re_{max} = 9.6$. The values are indicative of a steady state flow for the initial de- 631 signs.

632 Figure 10 shows temperature contour plots with streamlines of the optimized 633 designs for the different initial designs and design symmetry conditions. Values 634 for the temperature T_B, solid volume, and perimeter are given in Tables 5 and 635 6. Independent of the initial design the optimization process converges to equiva- 636 lent solutions. Similar to the petal problem studied above, the asymmetric design 637 yields the lowest objective temperature. Again, the asymmetric design features 638 substantially higher advective heat transport due to large flow velocities above 639 the solid structure; see Figures 11 and 12.

المنارة للاستشارات
www.manaraa.com

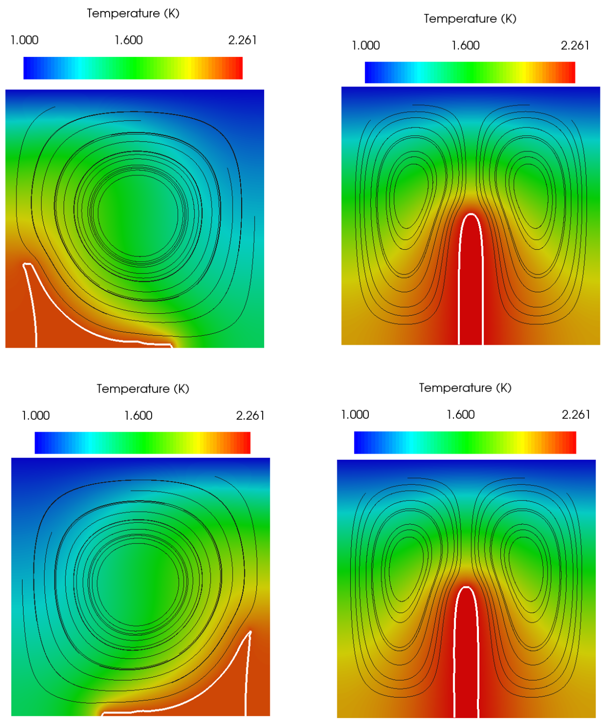

Fig. 10: Temperature contour plots with streamlines of the final designs for 2D steady-state topology optimization: circular initial design (top), inclusion initial design (bottom); free geometry (left), symmetric geometry (right).

Table 5: 2D steady-state topology optimization results for circular initial design.

Design	Initial Design	Final design (symmetric)	Final design (non-symmetric)
T_B $[K]$	2.71	2.26	2.16
Volume $[m^3]$	3.87×10^{-5}	3.93×10^{-5}	3.93×10^{-5}
Perimeter $[m^2]$	1.56×10^{-2}	3.14×10^{-2}	3.14×10^{-2}
Rayleigh	5.85×10^3	4.30×10^3	3.96×10^3
Grashof	9.90×10^3	7.27×10^3	6.70×10^3
Local Reynolds	8.99	5.27	1.85×10^1

المنارة للاستشارات
www.manaraa.com

Table 6: 2D steady-state topology optimization results for initial design with inclusions.

Design	Initial Design	Final design (symmetric)	Final design (non-symmetric)
T_B $[K]$	2.75	2.26	2.16
Volume $[m^3]$	2.84×10^{-5}	3.93×10^{-5}	3.92×10^{-5}
Perimeter $[m^2]$	2.52×10^{-2}	3.14×10^{-2}	3.14×10^{-2}
Rayleigh	5.99×10^3	4.30×10^3	3.95×10^3
Grashof	1.01×10^4	7.27×10^3	6.69×10^3
Local Reynolds	9.55	5.27	1.83×10^1

5.3 2D Transient Topology Optimization

Ensuring a steady-state flow for all designs throughout the optimization process imposes severe limitations on the class of optimization problems that can be considered. The proposed optimization framework allows for problems where the flow exhibits a transient response. To illustrate this capability, we consider a configuration similar to the one studied previously, but we increase the magnitude of the external heat flux by a factor $1,000$ and the dimensions of the design domain threefold. These modifications cause the flow to exhibit dynamic instabilities. Starting from a design domain of temperature T_0 and the fluid being at rest, the transient analysis is advanced in time until the temperature at point B reaches a quasi-steady-state, i.e. the temporal variations are much smaller than the average. Note the flow remains unstable and does not converge to a steady-state. The objective is the temperature averaged over the last N_t^{12} time steps.

We parameterize the level set function by the XFEM mesh and enforce a symmetric design by defining the nodal level set functions at corresponding nodes by the same optimization variables. The smoothing radius of the linear filter (15) is $r_f = 1.44 \times 10^{-3} m$. As in the previous topology optimization study, the radius of the circle of solid phase around point B is $r_{BS} = 10^{-3}\ m$. The upper limits for the volume and perimeter constraints also remain the same.

The problem parameters are summarized in Table 7. Note the large number of time steps needed to reach a quasi-steady-state response at point B. This is due to the significantly different time scales dominating the flow field and the thermal response in the solid. The time step size is driven by the requirement to resolve the transient fluid response while the total simulation time needs to be sufficiently large such that temperature field in the solid converges. The appropriate time steps size, Δt, the total number of time steps, N_t^2, and the number of time steps for averaging the objective temperature, N_t^{12}, were determined through numerical studies on the initial design.

To reduce the computational effort, we initialize the level set field with the symmetric design found for the steady-state case described previously. Snapshots of the temperature contours with stream lines of the initial and optimized designs

www.manaraa.com

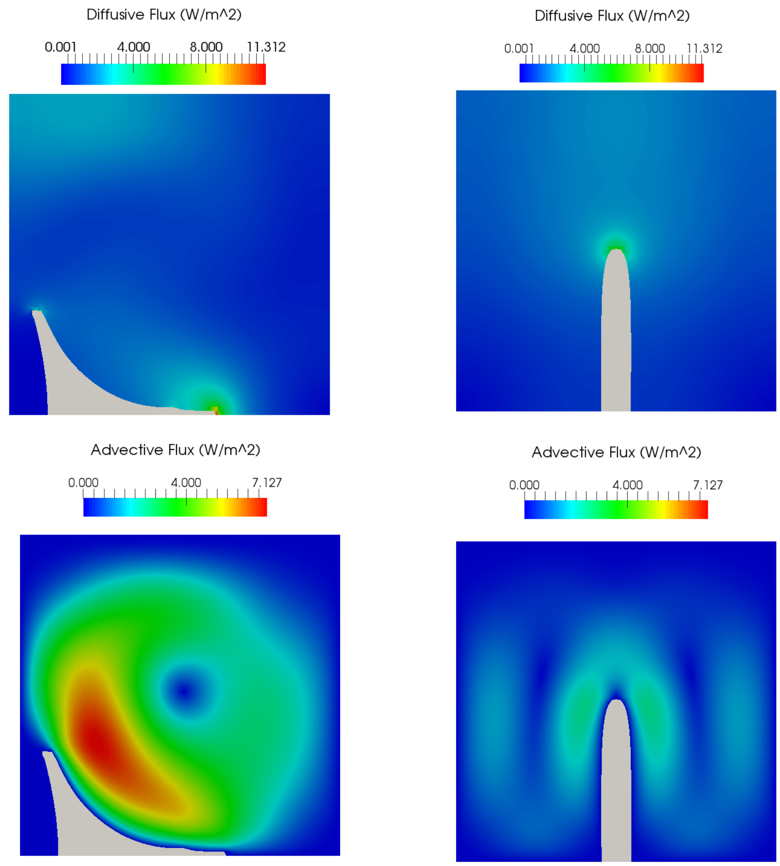

Fig. 11: Advective (bottom) and diffusive (top) of non-symmetric (left) and symmetric (right) designs.

are shown in Figure 13. For the both designs the flow develops a long, thin column that oscillates horizontally as the vortices at the top of the design domain move up and down. While the initial and optimized designs have the same topology, the transient optimum features a more bulbous tip compared to straight fin obtained for the low Grashof number, steady-state design.

The evolutions of the temperature at point B are shown in Figure 14 for the initial and final designs. For both configurations, the temperature reaches a quasi-steady-state. The average temperature at point B, the solid volume, the perimeter and the non-dimensional numbers characterizing the flow fields of the initial and final designs are given in Table 8. Note that the Rayleigh and Grashof numbers for the initial and optimized design are indicative of an unstable, transient flow.

المنارة للاستشارات
www.manaraa.com

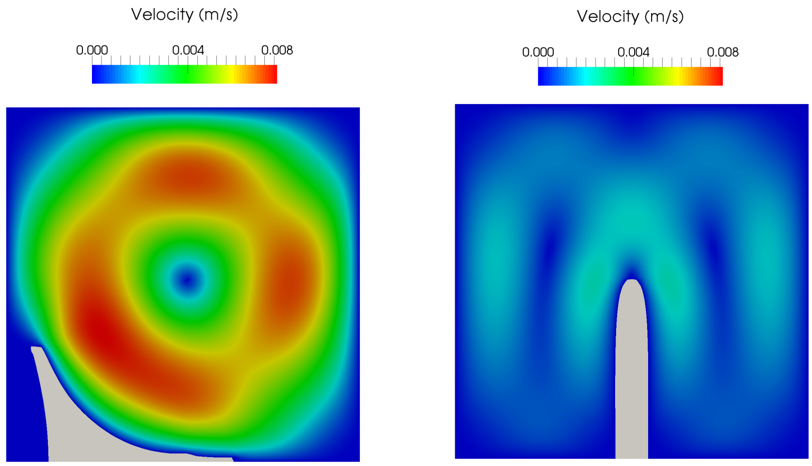

Fig. 12: Magnitude of fluid velocities of non-symmetric (left) and symmetric (right) designs.

Table 7: 2D transient topology optimization parameters.

Parameter	Value
Domain height	$h = 0.090m$
Domain width	$w = 0.090m$
Number of elements	6400
Heat flux	$q_B = 5.0 \times 10^1 W$
Volume constraint	$c_v = 3.93 \times 10^{-5} m^3$
Perimeter constraint	$c_{pe} = 3.14 \times 10^{-2} m^2$
Time step size	$\Delta t = 1.0s$
Total number of time steps	$N_t^2 = 2.5 \times 10^3$
Number of averaging time steps	$N_t^{12} = 100$

The transient optimum reduces the mean temperature by 7 % in comparison to the steady-state design which is optimized at much lower Grashof number. Analyzing the design optimized for the transient case at the configuration defined in Section 5.2, which yields a steady-state flow, the objective temperature is $T_B = 2.26\ K$ which is 0.2 % larger than the one of the symmetric steady-state design. This analysis illustrates the importance of optimizing the design for specific operating conditions and the resulting flow regimes.

Accounting for the (potentially) transient behavior of natural convection problems in the approach allows for the consideration of a larger range of Rayleigh and

www.manaraa.com

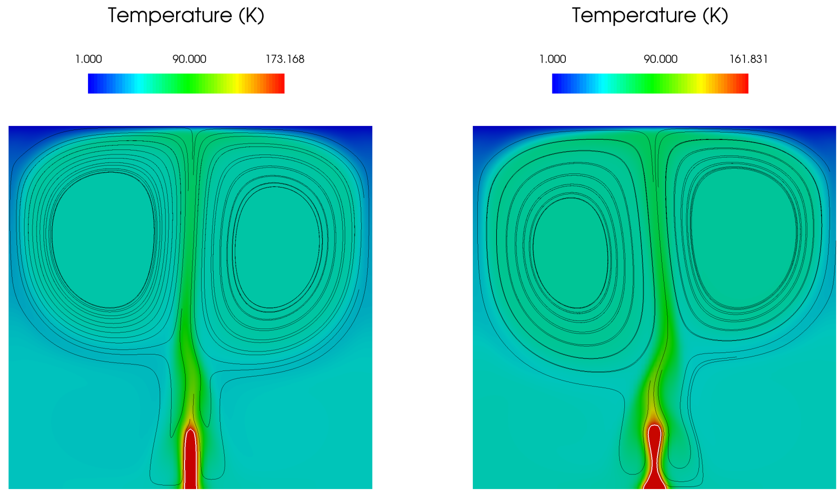

(a) Initial design (b) Final design

Fig. 13: Snapshot of temperature contours with streamlines for 2D transient topology optimization.

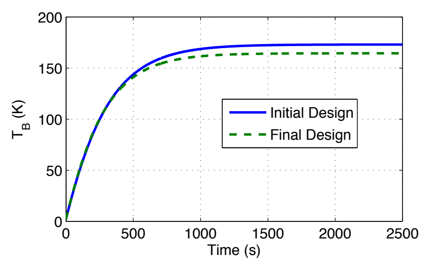

Fig. 14: Temperature T_B plotted over time for initial and final designs of 2D unsteady topology optimization problem.

Grashof numbers and increases confidence in the accuracy of the flow and thermal analysis. However, these advantages come at significant additional computational cost. Due to the serial nature of the time stepping schemes used in both the forward and sensitivity analyses, the computational cost per optimization iteration increases linearly with the number of time steps required. Owing to the time scales dominating the flow and thermal responses, a large number of time steps is needed to reach a quasi-steady-state response in the solid phase. In addition, a rather fine mesh is required to resolve spatially the flow. Here the XFEM model yields about 25,000 degrees of freedom; the exact number depends on the intersection configuration. The total time for a forward and sensitivity analysis was approximately 2

www.manaraa.com

Table 8: 2D unsteady topology optimization results.

Design	Initial Design	Final design
$mean(T_B)$ $[K]$	1.74×10^2	1.61×10^2
Volume $[m^3]$	3.83×10^{-5}	3.89×10^{-5}
Perimeter $[m^2]$	3.01×10^{-2}	3.46×10^{-2}
Rayleigh	1.60×10^7	1.48×10^7
Grashof	2.70×10^7	2.50×10^7
Local Reynolds	2.70×10^3	2.69×10^3

hours, using MUMPS for solving the linear sub-problems on a desktop computer with a six-core AMD Phenom II 1090T 3.2GHz processor and 8GB of RAM. For the total of 150 optimization iterations, 12 days' worth of computational time was required. To reduce the computational costs more advanced time integration approaches could be incorporated. Alternative spatial discretization schemes, such as finite volume or discontinuous Galerkin methods, may also increase the computational efficiency.

5.4 3D Steady-State Topology Optimization

Finally, we demonstrate that the proposed optimization framework is also applicable to natural convection problems in three dimensions. Due the significant computational costs of solving transient problems, we limit this study to a low-Grashof number configuration which guarantees steady-state solutions throughout the optimization process.

The natural convection problem of Section 5.2 is extended to three dimensions by rotating the design domain about the center as shown in Figure 4. The problem parameters are given in Table 9. The radius of the sphere of solid phase around point B is $r_{BS} = 2.5 \times 10^{-3}$ m. The smoothing radius of the linear filter (15) is $r_f = 1.069 \times 10^{-3}$ m. We enforce a double-symmetric design by defining the nodal level set functions at corresponding nodes by the same optimization variables. A layer of fluid material, 0.02 m thick, is prescribed at the top surface of the design domain to prevent the design from interacting with the boundary condition applied there.

As in the previous studies we impose constraints on the maximum solid volume and the perimeter. Numerical studies on the 3D configurations showed that small, sub-element-size features may emerge, causing the optimization process to stagnate. To suppress these features, we additionally impose a constraint on the level set gradient measure (16). The constraint limit is set initially to a rather large value which does not prohibit geometric features from merging. As the design converges the constraint values is lowered to remove sub-element-size features. A constraint of $c_g = 1.0 \times 10^{-7}$ is prescribed for 300 optimization iterations, then lowered to $c_g = 1.0 \times 10^{-9}$ for another 300 iterations.

المنارة للاستشارات
www.manaraa.com

Table 9: 3D box topology optimization parameters.

Parameter	Value
Domain height	$h = 0.030m$
Domain width	$w = 0.030m$
Number of elements	51680
Heat flux	$q_B = 3.333 \times 10^{-4}W$
Volume constraint	$c_v = 5.24 \times 10^{-7}m^3$
Perimeter constraint	$c_{pe} = 4.7 \times 10^{-4}m^2$
Gradient constraint	$c_g = [1.0 \times 10^{-7}, 1.0 \times 10^{-9}]m$

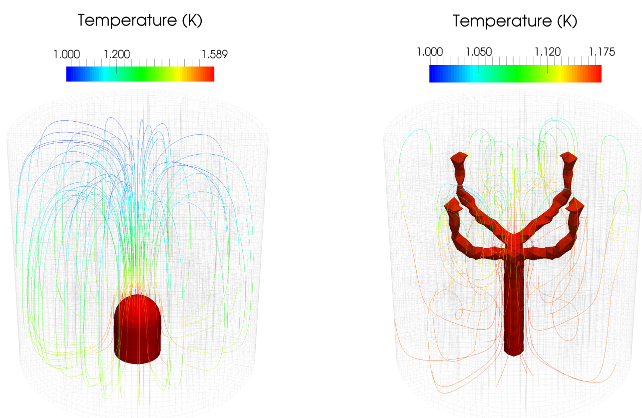

(a) Initial design (b) Final design

Fig. 15: Results for 3D box design problem.

We start the optimization process with a cylindrical solid phase of radius 0.003 m and height 0.005 m; a semi-sphere is placed at the top of the cylinder. The flow field of the initial design is characterized by a Rayleigh number of $Ra = 2000$, a Grashof number of $Gr = 3400$, and a maximum local Reynolds number of $Re_{max} = 5.0$. These numbers are similar to the ones of the configuration in Section 5.2 and indicative of a steady-state flow.

The streamlines for the initial and optimized designs are shown in Figure 15. The performance and flow characteristics are given in Table 10. The geometry of the 3D optimum deviates noticeably from the solution of the 2D steady state problem. While similar to the 2D solution the 3D design consists of a thin base, it splits into four branches in the top half, shown in Figure 15 (b). The 3D configuration appears to promote thinner features necessitating some form of feature size control; here implemented via a constraint on the level set gradient measure.

المنارة للاستشارات
www.manaraa.com

Table 10: 3D topology optimization results.

Design	Initial Design	Final design
T_B $[K]$	1.59	1.18
Volume $[m^3]$	1.89×10^{-7}	1.46×10^{-7}
Perimeter $[m^2]$	1.47×10^{-4}	3.81×10^{-4}
Rayleigh	2.01×10^{3}	5.99×10^{2}
Grashof	3.41×10^{3}	1.01×10^{3}
Local Reynolds	4.97	2.54×10^{-1}

This study demonstrates the applicability of the proposed optimization framework to 3D natural convection problems. However, we point out that the numerical and computationally complexity in solving the forward problem and the overall optimization problem is significantly increased over 2D problems. This includes the numerical stability of the XFEM formulation, in particular the treatment of the interface conditions, as well as the complexity of solving large nonlinear problems. The increased design freedom in 3D allows the emergence of complex geometries for which it is difficult to robustly compute flow solutions using uniformly refined meshes that are not altered in the optimization process.

6 Conclusions

This study presented an explicit LSM for optimizing the geometry of natural convection dominated flows. Our approach expands existing density methods onto transient problems. The energy transport is described by an advection-diffusion model. In the fluid phase, the advective velocity is modeled by the incompressible Navier-Stokes equations and the Boussinesq approximation of the buoyancy forces. In the solid phase, the advective velocity vanishes. The method relies on a XFEM discretization of the governing equations in the fluid and solid phase. The interface conditions are enforced weakly using Nitsche's method. To consider flows exhibiting dynamic instabilities, the flow and temperature fields are advanced in time by an implicit Euler backward time integration scheme. The design sensitivities of the steady-state and transient response are computed by an adjoint approach.

The main characteristics of the proposed method were studied with steady-state problems in 2D and 3D and a 2D transient problem. One of the main advantages of the LSM approach is that it provides a crisp geometry description throughout the optimization process and that it does not suffer from the presence of fictitious material in optimized material distribution, as Alexandersen et al (2014) reported for density methods. Studies on a 2D steady-state design problem illustrated that non-intuitive asymmetric designs feature improved cooling performance compared to optimized symmetric designs which converged to common fin-type shapes.

المنارة للاستشارات

www.manaraa.com

A study on a high-Grashof number configuration demonstrated the applicability of the proposed methods to problems where the flow exhibits dynamic instabilities and does not converge to a steady state. However, such problems are stymied by large computational costs as a fine mesh and small time steps are needed to resolve the transient flow and a large number of time steps is required to reach a quasi-steady-state thermal response in the solid. The applicability of the proposed method to 3D problems was illustrated with a low Grashof steady-state problem. For this problem, the need to control the size of geometric features was observed. To this end, a constraint on the gradients of the level set field was imposed, along with setting appropriate lower and upper bounds on the optimization variables. The application of the proposed method to 3D problems is hampered by large computational costs.

The numerical studies have demonstrated the applicability of the proposed method to a broad range of natural convection problems, including three-dimensional problems and problems with unstable, transient flows. Future studies should focus on reducing the computational costs, for example, via adaptive meshing techniques and adaptive time stepping schemes. Furthermore, robust and efficient schemes need to be developed to impose feature size constraints.

Acknowledgements The authors acknowledge the support of the National Science Foundation under grant EFRI-SEED 1038305 and CBET 1246854. The opinions and conclusions presented in this paper are those of the authors and do not necessarily reflect the views of the sponsoring organization.

References

Alexandersen J (2011) Topology optimization for convection problems. Bachelor thesis, DTU Mekanik

Alexandersen J (2015) Topology optimisation of passive coolers for light-emitting diode lamps. In: Proceedings of the 11th World Congress of Structural and Multidisciplinary Optimisation

Alexandersen J, Aage N, Andreasen CS, Sigmund O (2014) Topology optimisation for natural convection problems. International Journal for Numerical Methods in Fluids 76(10):699–721

Allaire G, Jouve F, Toader A (2002) A level-set method for shape optimization. Comptes Rendus Mathematique 334(12):1125–1130

Allaire G, Jouve F, Toader AM (2004) Structural optimization using sensitivity analysis and a level-set method. Journal of Computational Physics 194(1):363–393

Amestoy P, Duff I, LExcellent J (1998) MUMPS multifrontal massively parallel solver. Tech. rep., Version 2.0. Technical Report TR/PA/98/02. CERFACS, 42 Ave G. Coriolis, 31057 Toulouse Cedex, France

Bahadur R, Bar-Cohen A (2005) Thermal design and optimization of natural convection polymer pin fin heat sinks. Components and Packaging Technologies, IEEE Transactions on 28(2):238–246

Baïri A, Zarco-Pernia E, de María JMG (2014) A review on natural convection in enclosures for engineering applications. the particular case of the parallelogrammic diode cavity. Applied Thermal Engineering 63(1):304–322

www.manaraa.com

Bruns T (2007) Topology optimization of convection-dominated, steady-state heat transfer problems. International Journal of Heat and Mass Transfer 50(15-16):2859 – 2873

Burger M, Osher SJ (2005) A survey in mathematics for industry a survey on level set methods for inverse problems and optimal design. Euro Jnl of Applied Mathematics 16:263–301

Coffin P, Maute K (2015) Level set topology optimization of cooling and heating devices using a simplified convection model. under review in Structural and Multidisciplinary Optimization

Davis TA (2004) Algorithm 832: Umfpack v4. 3—an unsymmetric-pattern multifrontal method. ACM Transactions on Mathematical Software (TOMS) 30(2):196–199

Deaton JD, Grandhi RV (2014) A survey of structural and multidisciplinary continuum topology optimization: post 2000. Structural and Multidisciplinary Optimization 49(1):1–38

van Dijk N, Maute K, Langelaar M, Keulen F (2013) Level-set methods for structural topology optimization: a review. Structural and Multidisciplinary Optimization 48(3):437–472

Dolbow J, Harari I (2009) An efficient finite element method for embedded interface problems. Int J Numer Meth Engng 78:229–252

Franca LP, Frey SL, Hughes TJ (1992) Stabilized finite element methods: I. application to the advective-diffusive model. Computer Methods in Applied Mechanics and Engineering 95(2):253–276

Fries T, Belytschko T (2010) The extended/generalized finite element method: an overview of the method and its applications. International Journal for Numerical Methods in Engineering 84(3):253–304

Fries TP, Belytschko T (2006) The intrinsic XFEM: A method for arbitrary discontinuities without additional unkowns. International Journal for Numerical Methods in Engineering 68:1358–1385

Golmon S, Maute K, Dunn ML (2012) Multiscale design optimization of lithium ion batteries using adjoint sensitivity analysis. International Journal for Numerical Methods in Engineering 92(5):475–494

Iga A, Nishiwaki S, Izui K, Yoshimura M (2009) Topology optimization for thermal conductors considering design-dependent effects, including heat conduction and convection. International Journal of Heat and Mass Transfer 52(11-12):2721–2732

Jenkins N, Maute K (2015) Level set topology optimization of stationary fluid-structure interaction problems. Structural and Multidisciplinary Optimization pp 1–17, URL http://dx.doi.org/10.1007/s00158-015-1229-9

Khoei AR (2015) Extended finite element method: Theory and applications. Wiley

Koga AA, Lopes ECC, Villa Nova HF, Lima CRd, Silva ECN (2013) Development of heat sink device by using topology optimization. International Journal of Heat and Mass Transfer 64:759–772

Kontoleontos E, Papoutsis-Kiachagias E, Zymaris A, Papadimitriou D, Giannakoglou K (2013) Adjoint-based constrained topology optimization for viscous flows, including heat transfer. Engineering Optimization 45(8):941–961

Kreisselmeier G, Steinhauser R (1979) Systematic control design by optimizing a vector performance index. In: International Federation of Active Contrals Symposium on Computer Aided Design of Control Systems, Zurich, Switzerland

المنارة للاستشارات

www.manaraa.com

Kreissl S, Maute K (2011) Topology optimization for unsteady flow. International Journal for Numerical Methods in Engineering 87:1229–1253

Kreissl S, Maute K (2012) Levelset based fluid topology optimization using the extended finite element method. Structural and Multidisciplinary Optimization 46(3):311–326

Lang C, Makhija D, Doostan A, Maute K (2014) A simple and efficient preconditioning scheme for heaviside enriched XFEM. Computational Mechanics 54(5):1357–1374

Lee K (2012) Topology optimization of convective cooling system designs. PhD thesis, The University of Michigan

Luo Z, Tong L, Wang MY, Wang S (2007) Shape and topology optimization of compliant mechanisms using a parameterization level set method. Journal of Computational Physics 227(1):680–705

Makhija D, Maute K (2014) Numerical instabilities in level set topology optimization with the extended finite element method. Structural and Multidisciplinary Optimization 49(2):185–197

Makhija D, Maute K (2015) Level set topology optimization of scalar transport problems. Structural and Multidisciplinary Optimization 51(2):267–285

Marck G, Nemer M, Harion JL (2013) Topology optimization of heat and mass transfer problems: laminar flow. Numerical Heat Transfer, Part B: Fundamentals 63(6):508–539

Matsumori T, Kondoh T, Kawamoto A, Nomura T (2013) Topology optimization for fluid–thermal interaction problems under constant input power. Structural and Multidisciplinary Optimization 47(4):571–581

McConnell C, Pingen G (2012) Multi-layer, pseudo 3d thermal topology optimization of heat sinks. In: ASME 2012 International Mechanical Engineering Congress and Exposition, American Society of Mechanical Engineers, pp 2381–2392

Moon H, Kim C, Wang S (2004) Reliability-based topology optimization of thermal systems considering convection heat transfer. In: Proceedings of the 10th AIAA/ISSMO Multidisciplinary Analysis and Optimization Conference, August 30-September 1, Albany, NY

Morrison AT (1992) Optimization of heat sink fin geometries for heat sinks in natural convection. In: Thermal Phenomena in Electronic Systems, 1992. I-THERM III, InterSociety Conference on, IEEE, pp 145–148

Nitsche J (1975) Uber ein Variationsprinzip zur Loesung von Dirichlet-Problemen bei Verwendung von Teilraeumen, die keinen Randbedingungen unterworfen sind. Abhandlungen aus dem Mathematischen Seminar der Universitaet Hamburg 36:9–15

Pingen G, Waidmann M, Evgrafov A, Maute K (2010) A parametric level-set approach for topology optimization of flow domains. Structural and Multidisciplinary Optimization 41(1):117–131

Schott B, Rasthofer U, Gravemeier V, Wall W (2014) A face-oriented stabilized Nitsche-type extended variational multiscale method for incompressible two-phase flow. International Journal for Numerical Methods in Engineering URL http://dx.doi.org/10.1002/nme.4789

Seo JH (2009) Optimal design of material microstructure for convective heat transfer in a solid-fluid mixture. PhD thesis, University of Michigan at Ann Arbor

المنارة للاستشارات

www.manaraa.com

Sigmund O, Maute K (2013) Topology optimization approaches: A comparative review. Structural and Multidisciplinary Optimization 48(6):1031–1055

Svanberg K (2002) A class of globally convergent optimization methods based on conservative convex separable approximations. SIAM J on Optimization 12(2):555–573

Terada K, Asai M, Yamagishi M (2003) Finite cover method for linear and non-linear analyses of heterogeneous solids. International Journal for Numerical Methods in Engineering 58(9):1321–1346

Tezduyar TE, Mittal S, Ray SE, Shih R (1992) Incompressible flow computations with stabilized bilinear and linear equal-order-interpolation velocity-pressure elements. Computer Methods in Applied Mechanics and Engineering 95:221–242

Touihri R, Hadid HB, Henry D (1999) On the onset of convective instabilities in cylindrical cavities heated from below. i. pure thermal case. Physics of Fluids (1994-present) 11(8):2078–2088

Tran AB, Yvonnet J, He QC, Toulemonde C, Sanahuja J (2011) A multiple level set approach to prevent numerical artefacts in complex microstructures with nearby inclusions within xfem. International Journal for Numerical Methods in Engineering 85(11):1436–1459

Wang MY, Wang X, Guo D (2003) A level set method for structural topology optimization. Computer Methods in Applied Mechanics and Engineering 192(1-2):227–246

Wang S, Wang M (2006) Radial basis functions and level set method for structural topology optimization. International journal for numerical methods in engineering 65(12):2060–2090

Yaji K, Yamada T, Kubo S, Izui K, Nishiwaki S (2015) A topology optimization method for a coupled thermal–fluid problem using level set boundary expressions. International Journal of Heat and Mass Transfer 81:878–888

Yamada T, Izui K, Nishiwaki S (2011) A level set-based topology optimization method for maximizing thermal diffusivity in problems including design-dependent effects. Journal of Mechanical Design 133(3):031,011

Yin L, Ananthasuresh G (2002) A novel topology design scheme for the multi-physics problems of electro-thermally actuated compliant micromechanisms. Sensors and Actuators A: Physical 97:599–609

Yoon G, Kim Y (2005) The element connectivity parameterization formulation for the topology design optimization of multiphysics systems. International journal for numerical methods in engineering 64(12):1649–1677

Yoon GH (2010) Topological design of heat dissipating structure with forced convective heat transfer. Journal of Mechanical Science and Technology 24:1225–1233

www.manaraa.com

Appendix C

Manuscript [M1]: A Measure for Feature Size Control in Explicit Level Set eXtended Finite Element Method Topology Optimization

المنارة للاستشارات
www.manaraa.com

Structural and Multidisciplinary Optimization manuscript No.
(will be inserted by the editor)

A Measure for Feature Size Control in Explicit Level Set eXtended Finite Element Method Topology Optimization

Peter Coffin · Kurt Maute

Received: date / Accepted: date

Abstract In this paper we seek to control the minimum feature size in geometries during topology optimization. Control of minimum feature size is important to maintaining manufacturability of the geometry and accurate representation of it during analysis of the governing equations. The feature size control method presented in this work utilizes the eXtended Finite Element Method (XFEM) surface representation within a Level Set Method (LSM) and permits sharp corners. Some feature size control techniques for Level Set Methods (LSMs) rely on sign-distance-like features of the Level Set Field (LSF), which requires a refined mesh to ensure accurate geometry representation. Explicit LSMs also do not retain a sign-distance-like LSF, requiring reconstruction of the field, which may be expensive. The other feature size control technique for LSMs, the quadratic energy method, compares the interface's tangent vector at integration points, which may be misleading when considering discretized interfaces. The feature size control measure developed here identifies violations of a minimum feature size and can be incorporated as a penalty or constraint on the optimization problem. The XFEM provides a crisp representation of the level set geometry and integration along its interface. Two-phase problems are considered and the minimum feature size can be prescribed in a single or both material phases. The measure is demonstrated on structural and convective heat transfer topology optimization problems. When used as a constraint the measure is able to deter the formation of features smaller than the prescribed sized. To remove existing small features the constraint is re-

Peter Coffin
Department of Aerospace Engineering,
University of Colorado at Boulder,
Boulder, CO 427 UCB, USA
e-mail: peter.coffin@colorado.edu

K. Maute
Department of Aerospace Engineering,
University of Colorado at Boulder,
Boulder, CO 427 UCB, USA
e-mail: maute@colorado.edu

للاستشارات المنارة
www.manaraa.com

placed with a penalty that is applied over a series of steps with increasing feature size. The influence of a tuning parameter is demonstrated, changing the curvature of resulting designs.

Keywords Topology Optimization · Level Set Methods · Feature Size Control · eXtended Finite Element Method

1 Introduction

Topology optimization has gained traction as a computational design technique in recent decades. It is an appealing approach as it minimizes the influence of initial designs with its capability to represent large geometry changes in the optimization process. The control of "feature size" or "length scale" is important to ensure manufacturability and accurate analysis of functionality. Manufacturing methods have limitations on the length scales that they can accurately construct. Given these limitations, it may be necessary to incorporate controls on feature size to ensure ensure that designs are not overly difficult or costly to construct. To accurately predict design performance the mesh used for discretization must be sufficiently fine to accurately represent the behavior of all feature sizes of a given geometry. Given a particular mesh it is be necessary to control feature size to ensure that geometries are accurately represented. Adaptive mesh refinement is an alternative approach. As feature sizes approach zero, adaptive mesh refinement becomes impractical as well.

Feature size control techniques have been studied in both density topology optimization methods and Level Set Methods (LSMs). Density based topology optimization methods describe geometry via a fictitious material, whose density or volume fraction is a continuous function of the optimization variables. The extrema of the density (typically 0 and 1) represent distinct materials, such as void and solid. The mechanical models are then constructed such that material properties can be interpolated as a function of the density, the extrema mimicking the distinct materials and the intermediate values a mixture of the two.

Feature size control methods have been studied for density methods, for example: consideration of manufacturing processes (Zhou et al, 2014), projection schemes (Guest et al, 2004), local density variation (Poulsen, 2003), robust design formulations (Schevenels et al, 2011), medial surface reconstruction (Zhang et al, 2014) and three-field-schemes (Zhou et al, 2015).

An alternative approach to the density geometry description are LSMs, where the geometric boundaries are defined by the iso-contour of an auxiliary field. These methods are advantageous in problems where accurate representation of the interface is important to the physics modeling (Coffin and Maute, 2015). A recent review of LSMs for topology optimization is provided by van Dijk et al (2013).

Level Set Fields (LSFs) are commonly updated by solving the Hamilton-Jacobi equation or an augmentation of it. These are referred to as implicit methods. Explicit LSMs, considered here, define the LSF as explicit functions of the design variables, the update of the design variables is performed by NonLinear Programming methods (NLPs). In both methods the spatial gradients of the LSF near the material interface influence the scaling of the sensitivities. As the LSF becomes flat or steep near the interface the problem can become poorly scaled, leading to convergence difficulties (van Dijk et al, 2013). Implicit methods typically incorporate

المنارة للاستشارات
www.manaraa.com

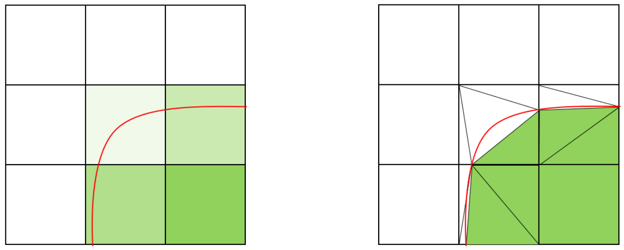

(a) Ersatz material representation

(b) XFEM representation showing decomposition for integration

Fig. 1: Comparison of smeared, ersatz material representation vs XFEM decomposition.

a reinitialization scheme to retain a sign-distance field. Explicit methods typically do not retain a sign-distance field but introduce alternative regularization methods to control the spatial gradients of the LSF. Tikhonov regularization or penalization of intermediate LSF fields are common approach for LSF regularization (van Dijk et al, 2013).

Physical models are often incorporated into LSMs in a similar fashion as density methods, through material property interpolation. Referred to as Ersatz material models, the material properties are interpolated as a function of the material volume fraction within a finite element. These methods can suffer from smeared interface phenomena or geometric artifacts that affect the resolution and accuracy of the finite element model, Figure 1 (a) (van Dijk et al, 2013).

In this work we consider the eXtended Finite Element (XFEM) to discretize the governing equations. This approach has been shown to preserve the crispness of the boundary definitions provided by the LSM. A feature of the XFEM is the decomposition of intersected elements for accurate integration of those elements and the material interface, Figure 1 (b). The decomposition of the element into triangular (2D) or tetrahedral (3D) subdomains yields a surface mesh that describes material interfaces via triangle edges (2D) or tetrahedra faces (3D).

Multiple approaches have been proposed for feature size identification and control in LSMs. These approaches vary in the information that is used to identify features. These approaches may take advantage of the existing sign-distance or nearly sign-distance function LSF to identify the skeleton of the geometry via its curvature (Guo et al, 2014; Xia and Shi, 2015; Allaire et al, 2014; Liu et al, 2015). The maintenance or construction of a sign-distance field increases the computational cost of these methods. Alternatively the discretized material interface itself can also be used to identify features (Chen et al, 2008). Chen et al (2008) and Luo et al (2008) compute a quadratic energy function, an integral over the interface. The form of this measure and a comparison of it to the measure we present in this work is provided in Section 3. All of the measures discussed in the previous paragraph are incorporated into the optimization problem as penalties on the objective function or constraints. Allaire et al (2014), Guo et al (2014) and Xia and

www.manaraa.com

Shi (2015) make clear that construct these scalar penalty or constraint values by integrating their point-wise measures of feature size.

In this work we develop an approach that directly utilizes the XFEM discretized interface to ensure a crisp representation of the boundary. This also bypasses the need for a sign-distance LSF. Utilizing the XFEM interface additionally allows the measure to directly identify the geometry as it is incorporated into the XFEM analysis of the governing physics. The measure is constructed to identify violations of a prescribed minimum feature size. The measure will be incorporated in the optimization problem as a penalty on the objective function or as an inequality constraint. This allows the optimization algorithm the most freedom to choose designs as compared to methods that incorporate minimum feature size into the parameterization of the geometry.

In Section 2 the LS-XEM that is used to describe geometry and discretize the governing equations is described. The minimum feature size measure and its incorporation as a constraint is outlined in Section 3. Finally, three design problems are studied using the minimum feature size constraint scheme in Section 4 and conclusions are presented in Section 5.

2 Level Set-XFEM

2.1 Parametrization of Level Set Function

The geometry of a two-phase design is defined by the LSF, $\phi(\mathbf{x})$, where $\mathbf{x}$ denotes the vector of spatial coordinates. In this work the two phases are either solid and void or two different diffusive materials. Considering only two-phase problems, only a single LSF function is necessary to describe the spatial distribution of the materials as follows:

$$\begin{aligned} \phi(\mathbf{x}) &< 0, \quad \forall\, \mathbf{x} \in \Omega_1, \\ \phi(\mathbf{x}) &> 0, \quad \forall\, \mathbf{x} \in \Omega_2, \\ \phi(\mathbf{x}) &= 0, \quad \forall\, \mathbf{x} \in \Gamma_{12}, \end{aligned} \tag{1}$$

where Ω_1 is the volume occupied by the first phase, Ω_2 the volume occupied by the second phase and Γ_{12} the interface between the two.

The level set function can be parameterized in a variety of ways for example, by finite element basis functions (Allaire et al, 2004), radial basis functions (Kreissl et al, 2011) or spectral basis functions (Gomes and Suleman, 2006). To allow for the emergence of a large set of geometries, here the LSF is parameterized by the shape functions defined on a finite element mesh. For simplicity we use the same mesh for the XFEM and the LSF parameterization, although this is not necessary in general.

Each design variable, $s_i,\ i = 1 \dots N_n$, is assigned to a corresponding node in the XFEM mesh, where N_n denotes the number of nodes. The optimization variables are smoothed so that the LSF value of the i-th node, ϕ_i, is explicitly defined by the optimization variables as follows:

$$\phi_i = \frac{1}{l_\phi} \left(\sum_{j=1}^{N_n} w_{ij} \right)^{-1} \sum_{j=1}^{N_n} w_{ij} s_j, \tag{2}$$

www.manaraa.com

where

$$w_{ij} = max\left(0, (r_f - |\mathbf{x}_i - \mathbf{x}_j|)\right), \tag{3}$$

and r_f is the prescribed filter radius. The value l_ϕ is a scaling to allow design variables to remain approximately in the range of $[-1, 1]$ when the LSF is well formed. We consider the LSF to be well formed when the magnitude of its gradient is approximately 1 near the zero-contour and 0 more than one or two elements away from the zero-contour. We set the value of l_ϕ equal to twice the width of an element.

Convergence during the optimization process is accelerated by the filter (2) and smoother shapes may be promoted; see, for example, Kreissl and Maute (2012). Filter radii of $2.0 - 4.0$ times the element width have shown to yield effective smoothing and efficient performance in numeric experiments.

Here, bi-linear and tri-linear shape functions are used for 2D and 3D problems to parameterize the LSF. By their construction, these shape functions only allow an element edge to be intersected by the phase interface, i.e. $\phi = 0$, at most once. This restriction due to parameterization can lead to convergence issues during the optimization process if sub-element-size features are desirable. This behavior has been discussed in Jenkins and Maute (2015) and Coffin and Maute (2015). A regularization scheme to discourage sub-element-size features has been utilized in Coffin and Maute (2015). As the scheme is not mesh independent a more advanced approach is desired and provides additional motivation for this work.

2.2 Spatial Discretization

The governing equations of the problem are discretized in space by the XFEM. Standard finite element interpolation is augmented with additional enrichment functions so that discontinuities at phase boundaries can be represented. A variety of enrichment schemes exist to handle different types of discontinuities, for example: discontinuities in the state variables or discontinuities in their spatial derivatives (Fries and Belytschko, 2010). The Heaviside enrichment scheme, used here, has been applied to a variety of problems; see for example, Gerstenberger and Wall (2008); Chahine et al (2008). The scheme has been studied in topology optimization by Kreissl and Maute (2012) for fluid problems, Lang et al (2014) for diffusive problems, and Villanueva and Maute (2014) for solid mechanics, among others.

The XFEM is used to discretize state fields within finite elements that are intersected by a phase interface, i.e. the zero level set iso-contour. Finite elements that do not contain a phase boundary are discretized using traditional finite element interpolation. Within intersected elements a Heaviside enrichment strategy is used. The discretized field, $\hat{u}$, is defined as:

$$\begin{aligned}\hat{u}(\mathbf{x}) = \sum_{m=1}^{M} \Bigg(& H(-\bar{\phi}(\mathbf{x})) \sum_{i \in I} N_i(\mathbf{x})\ \delta_{mk}^{i,F}\ u_{i,m}^{F} \\ & + H(\bar{\phi}(\mathbf{x})) \sum_{i \in I} N_i(\mathbf{x})\ \delta_{mn}^{i,S}\ u_{i,m}^{S} \Bigg)\end{aligned} \tag{4}$$

where I is the set of all elemental nodes, $N_i(\mathbf{x})$ the nodal basis functions, M the number of enrichment levels, and $u_{i,m}^1$ and $u_{i,m}^2$ are the degrees of freedom

www.manaraa.com

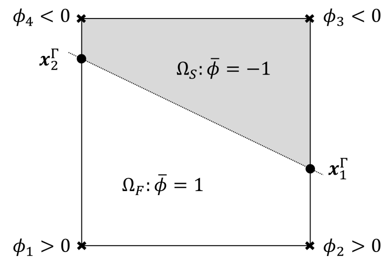

Fig. 2: Construction of interface geometry for intersected elements.

of enrichment level m at node i in the first and second phases, respectively. At any given point, only one degree of freedom per node is used to interpolation the solution, ensuring that the partition of unity is satisfied. The indices k and n denote the active degrees of freedom for the i-th nodes in the first and second phases, respectively. The Kronecker delta is $\delta_{ab}^{i,P}$, which selects the degrees of freedom for phases $P = [1, 2]$. The Heaviside function $H(z)$ determines the active interpolation for the particular phase and is defined as:

$$H(z) = \begin{cases} 1 & z > 0 \\ 0 & z \leq 0 \end{cases} . \tag{5}$$

To ensure that physically disconnected regions of the same phase are properly disconnected in the XFEM it is often necessary for multiple enrichment levels, i.e. sets of shape functions be used for each state variable. This approach as discussed in detail by Makhija and Maute (2014), Terada et al (2003), and Tran et al (2011), the particular approach used here being discussed by Makhija and Maute (2014).

Intersected elements are decomposed into triangles in 2D and tetrahedrons in 3D to allow for accurate integration of the weak form of governing equation by Gauss quadrature. The decomposition is formed by first identifying the intersection points $\mathbf{x}_i^{\Gamma}$ along element edges, that is where $\phi = 0$; see Figure 2. The position of the intersection points is defined by the level set value at the nodes on the edge.

In the rest of this work we will frequently operate on the XFEM interface, Γ. This is the set of edges (2D) or faces (3D) defined by the intersection points $\mathbf{x}_i^{\Gamma}$. The position of the XFEM interface Γ is related to the design variables by the positions of its nodes, the intersection points $\mathbf{x}_i^{\Gamma}$. The connection of these intersection points creates edges (2D) or faces (3D). To compute our feature size measure we operate on this mesh. The positions of the nodes (intersection points) of this surface mesh are functions of the design variables.

3 Feature Size Measure

Here we develop a measure of minimum feature size that operates on surface meshes such as those generated in topology optimization by LS-XFEMs. First, we seek to compute a scalar value that identifies whether a minimum feature size is

www.manaraa.com

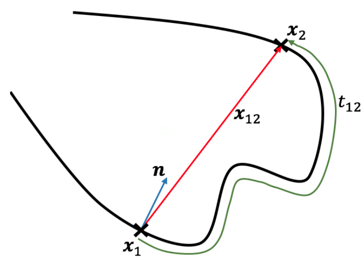

Fig. 3: Interface geometry for measure calculation.

violated. Using this geometry will ensure consistency between the XFEM analysis of the physics and the analysis of the feature size.

Our approach is closely related to the work of Chen et al (2008) uses a quadratic energy approach. Their work utilizes a double integral over the phase boundary. In practice the double integral is computed numerically using Gauss quadrature. At each set of comparison points the Euclidean distance and the tangent vectors are compared:

$$E_q = -\int_p \int_{p'} \mathbf{t}(p) \cdot \mathbf{t}(p') \psi(|\mathbf{x}(p) - \mathbf{x}(p')|) \; dp \; dp', \tag{6}$$

where p and p' are points along the phase interface, $\mathbf{t}$ is the tangent vector on the interface and $\mathbf{x}$ is the Euclidean position. This measure requires that tangent vectors are formed in a consistent direction along the interface. In 2D for arbitrary sets of surfaces this can be completed by computing the cross-product of the out-of-plane vector and the interface normal. The quadratic energy function E_q also may identify corners even if their radius is large. Corners on a surface mesh will be constructed of a series of line segments. Without additional smoothing the tangents will be discontinuous and may excite the measure. We seek to allow sharp corners in the surface as long as their angles are sufficiently large.

3.1 Measure Calculation

Similar to Chen et al (2008), the measure, M, is a double integral over the phase interface and the integrand is a product of two Heaviside functions, written as:

$$M = \int_{\Gamma_2} \int_{\Gamma_1} H\left(\frac{t_{12}(\mathbf{s})}{|\mathbf{x_{12}}(\mathbf{s})|} - r_{tx}\right) \cdot H\left(|\mathbf{x_{12}}(\mathbf{s})| - \mathbf{r_x}\right) d\Gamma_1 d\Gamma_2, \tag{7}$$

where

$$H(a) = \begin{cases} 0 & a \leq 0 \\ 1 & 0 < a \end{cases} \tag{8}$$

www.manaraa.com

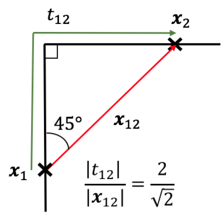

Fig. 4: Initial estimate for appropriate r_{tx} value with points equidistant about a right-angle corner.

A graphical representation of an interface and two comparison points is shown in Figure 3 where the Euclidean distance between the points $\mathbf{x_1}(\mathbf{s})$ and $\mathbf{x_2}(\mathbf{s})$ is written as:

$$|\mathbf{x_{12}}(\mathbf{s})| = \mathbf{x_1}(\mathbf{s}) - \mathbf{x_2}(\mathbf{s}), \tag{9}$$

while the distance along the interface between points is $t_{12}(\mathbf{s})$. The position of the interface is a function of the design variables.

The product of Heaviside functions identifies points that are close in Euclidean distance (second Heaviside function) and are relatively far in interface distance (first Heaviside function). The value of the first Heaviside function is restated as:

$$H\left(\frac{t_{12}(\mathbf{s})}{|\mathbf{x_{12}}(\mathbf{s})|} - r_{tx}\right) = \begin{cases} 0 & \frac{t_{12}(\mathbf{s})}{|\mathbf{x_{12}}(\mathbf{s})|} \leq r_{tx} \\ 1 & \frac{t_{12}(\mathbf{s})}{|\mathbf{x_{12}}(\mathbf{s})|} > r_{tx} \end{cases} \tag{10}$$

The second Heaviside function identifies points that are nearby in Euclidean distance, points that violate the feature size, r_x:

$$H\left(|\mathbf{x_{12}}(\mathbf{s})| - \mathbf{r_x}\right) = \begin{cases} 0 & |\mathbf{x_{12}}(\mathbf{s})| \geq \mathbf{r_x} \\ 1 & |\mathbf{x_{12}}(\mathbf{s})| < \mathbf{r_x} \end{cases} \tag{11}$$

The scaling r_{tx} that is found in the first Heaviside function is generally chosen to be:

$$r_{tx} = 2/\sqrt{(}2). \tag{12}$$

This ratio is the relative distance of an opposing point equidistant around a 90-degree corner, shown in Figure 4. The impact of this choice of scaling, r_{tx}, will be discussed later and studied in a numeric example.

The above measure does not distinguish between features of different phases. To allow the measure to identify features formed by a particular phase we modify it such that:

$$M = \int_{\Gamma_2}\int_{\Gamma_1} H\left(\frac{t_{12}(\mathbf{s})}{|\mathbf{x_{12}}(\mathbf{s})|} - r_{tx}\right) \cdot H\left(|\mathbf{x_{12}}(\mathbf{s})| - \mathbf{r_x}\right) \cdot H\left(P_S\left[\mathbf{x_{12}}(\mathbf{s})\right] \cdot \mathbf{n_1}(\mathbf{s})\right) d\Gamma_1 d\Gamma_2. \tag{13}$$

The additional, Heaviside function allows the measure to identify features that are formed by a phase. This identification is performed by comparing the vector

المنارة للاستشارات
www.manaraa.com

between the two points to the interface normal at the first point. The normal is constructed so that it points from the first phase into the second. If the dot product of the normal $\mathbf{n}$ and the vector $\mathbf{x_{12}}$ is positive the feature is identified as being formed by the second phase. If the value is negative the feature is formed by the first phase. To change which phase forms features that are identified, a switch value, P_S, is used so that:

$$P_S = \begin{cases} 1, & \text{Identify Phase 1 Features} \\ -1, & \text{Identify Phase 2 Features} \end{cases} . \tag{14}$$

The measure (13) will be incorporated into the optimization problem as either a penalty or inequality constraint. The penalty is used as a weaker form of enforcement as it allows the optimizer to violate the minimum feature size to produce better performance. This is useful as an initial step to allow designs some freedom to change topology.

A normalized constraint (15) is preferred to strictly enforce feature size. Normalizing the measure by perimeter allows the designer to choose a single value of allowable violation, c_{MN}, regardless of the problem perimeter. The constraint, $g_{FS,N}$, on feature size can be written as:

$$g_{FS,N} = \frac{M}{P^2} - c_{MN} \leq 0, \tag{15}$$

where the feature size measure, M, is normalized with the square of the perimeter, P, and bound by some small value, c_M. The smaller c_M, the more strongly the constraint is enforced. This form is useful where perimeter is constrained. For certain problems this approach may lead to geometric features that only act to increase the design's perimeter. The increase in perimeter allows for larger feature size violations in the normalized form of the constraint (15). A form of the constraint that does not incorporate the normalization (16) is used when necessary to bypass this difficulty. The constraint may also be written as:

$$g_{FS} = M - c_M \leq 0, \tag{16}$$

where the normalization by perimeter is removed. The allowable violation c_M in this form can be chosen as:

$$c_M = P^2 c_{MN}, \tag{17}$$

where the perimeter P is take from some characteristic design.

To ensure the differentiability of the measure with respect to the position of the interface nodes the Heaviside functions in (7) and (13) are relaxed with a smoothed Heaviside, $\hat{H}(a)$:

$$\hat{H}(a) = \begin{cases} a \leq -w_a & 0.0 \\ -w_a < a < w_a & \frac{1}{2} + \frac{a}{w_a}\left[\frac{15}{16} - \frac{a^2}{w_a^2}\left(\frac{5}{8} - \frac{3}{16}\frac{a^2}{w_a^2}\right)\right] \\ w_a \leq a & 1.0 \end{cases} \tag{18}$$

We set the width of the Heaviside, w_a, equal to a function of the feature size. Numerical experiments have shown that for the first and third Heaviside functions the width can be set to a small value, $w_a = r_x/10$. The second Heaviside, which drives our measure of feature size, should be set to a larger value: $w_a = r_x/2$.

المنارة للاستشارات

www.manaraa.com

4 Numeric Examples

In this section we examine the application of this measure to different design problems. It is important to note that to strictly enforce the feature size measure in both phases prevents the change of topology. In the LS-XFEM, creation, merging or removal of holes requires the formation of small features. If these small features are not allowed, changes in topology cannot happen and the variation of designs is severely limited. This consideration will be discussed in this section.

We first apply the the feature size measure to the well-known MBB design problem. This solid mechanics problem leads to the development of many thin, truss-like structures (Michell, 1904). The MBB problem will be studied to illustrate the differences between applying the measure to one or both phases. We also study the enforcement of the measure considering different minimum feature sizes.

We apply the feature size measure to the force inverter design problem (Bendsøe and Sigmund, 2003). In the LS-XFEM this problem is difficult to solve with a single material as the optimizer drives the connection towards a thin hinge that can disconnect leading towards discontinuous response of the performance with respect to the design variables.

Finally, a convective design problem is also studied. This class of problems also leads to thin geometric features but primarily seeks to maximize surface area of the interface. In this example an initial design of a semi-circle is used. The complex, wavy surface that is produced by this problem also provides a clear demonstration of the influence of varying the parameter r_{tx}.

4.1 Optimization Problem

The design problems studied here have a state-dependent objective. The inequality constraints in this work are not state dependent and only depend on the LSF, which is an explicit function of the optimization variables. The class of optimization problems considered here can be written as follows:

$$
\begin{aligned}
min_{\mathbf{s}} \quad & Z\left(\mathbf{s}, \mathbf{u}\left(\mathbf{s}\right)\right), \\
\text{s.t.} \quad & g_i(\mathbf{s}) \leq 0 \quad i = 1 \ldots N_g \ , \\
& \mathbf{s} \in \mathbf{S} = \left\{ \mathbb{R}^{N_s} | s_i^L \leq s_i \leq s_i^U \ , \ i = 1....N_s \right\} \ ,
\end{aligned}
\tag{19}
$$

where the objective Z is a function that depends on the vector of optimization variables $\mathbf{s}$ and the vector of state variables $\mathbf{u}$. N_s optimization variables s_i are bound by the lower and upper limits, s_i^L and s_i^U. The state variables satisfy the governing equations of the particular problem as described below. The system is constrained by N_g inequality constraints.

The Globally Convergent Method of Moving Asymptotes (GCMMA) of Svanberg (2002) is used to solve the optimization problem. The GCMMA parameters are: relative step size, 0.04; minimum asymptote adaptivity, 0.5; initial asymptote adaptivity, 0.7; maximum adaptivity, 1.43; and constraint penalty, 50. The optimization problem is considered converged if the change of the objective function relative to the initial objective value is less than 10^{-6} and the constraints are satisfied.

www.manaraa.com

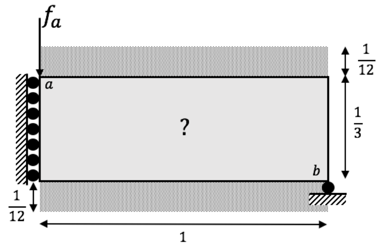

Fig. 5: Configuration of boundary conditions and design domain for MBB beam example.

4.2 MBB Beam

4.2.1 Setup

We demonstrate the basic functionality of the feature size measure using the well-known MBB beam design problem. The exact parameter set is taken from Sigmund (2009). The objective is to minimize strain energy of a beam by arranging a limited amount solid material in a domain, Figure 5. Optimal designs typically have many thin truss-like structures; see Michell (1904), making this a logical problem to apply a feature size constraint to.

Additional regions (shown in Figure 5 as dotted area), are included in the mesh above and below the design domain. In these regions, the design variables are fixed to +1, ensuring void. These additional regions are used to ensure that both edges of a feature that lies along the top of the design domain are part of the XFEM interface so they can be accounted for by the feature size measure.

The objective, $Z(\mathbf{s}, \mathbf{u})$, is written as:

$$Z(\mathbf{s}, \mathbf{u}) = \int_{\Omega_S} \frac{1}{2} \sigma_{ij} \epsilon_{ij} d\Omega_S + c_{MP} M, \tag{20}$$

where Ω_S is the domain of solid material, σ_{ij} the elastic stress and ϵ_{ij} the elastic strain. The factor c_{MP} is a scaling coefficient for a penalty on the feature size measure M. We assume a linear, elastic constitutive and kinematic models with an Elastic modulus of $E = 1.0$ and Poisson ratio of $\nu = 0.3$. The constraint, g_1, is written as:

$$g_1 = V_S - c_v V_T \leq 0, \tag{21}$$

where the solid material volume, V_S, should be less than some fraction, c_V, of the total design domain volume, V_T. In this example, c_v is set equal to 0.5. The second constraint is that of feature size; i.e. $g_2 = g_{FS,N}$, (15). The choice of c_{MN} and c_{MP} will be stated and discussed for each configuration.

The states are computed by solving the weak form of the governing equations, written as:

$$R = \int_{\Omega_S} \delta\epsilon_{ij} \sigma_{ij} d\Omega_S + \int_{\Gamma_N} \delta u_i F_i \ , \tag{22}$$

www.manaraa.com

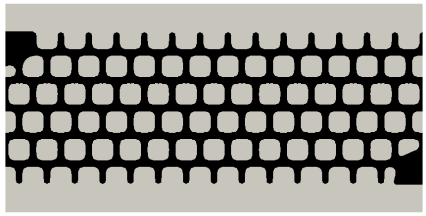

Fig. 6: Initial design for MBB beam optimization.

Table 1: MBB beam configuration parameters.

	Value
Elements	150×50
Filter Radius	$r_f = 0.016$
Number of design variables	$N_S = 7701$
Lower Bound	$s^L = -1$
Upper Bound	$s^U = 1$
Level Set Scaling	$l_\phi = \frac{1}{75}$

where Γ_N is the boundary where an external force, F_i is applied and u_i is the vector of displacements. The elastic strain is written as:

$$\epsilon_{ij} = \frac{1}{2}\left(\frac{\partial u_i}{\partial x_j} + \frac{\partial u_j}{\partial x_i}\right), \tag{23}$$

while the stress is written as:

$$\sigma_{ij} = \lambda \delta_{ij} \epsilon_{kk} + 2\mu\epsilon_{ij}, \tag{24}$$

where δ_{ij} is the Kronacker-Delta operator and λ and μ are the Lamé parameters:

$$\lambda = \frac{E\nu}{(1+\nu)(1-2\nu)}, \tag{25}$$

$$\mu = \frac{E}{2(1+\nu)}. \tag{26}$$

The test function is δu while $\delta\epsilon_{ij}$ is the elastic strain operating on the test function δu.

The initial design for performing the optimization consists of a series of 16×6 cuboid void inclusions of radius 0.025 and is shown in Figure 6. Other parameters are shown in Table 1. The design variables within a radius of 0.066 of points a and b are fixed to -1, ensuring a region of solid material around the points.

المنارة للاستشارات
www.manaraa.com

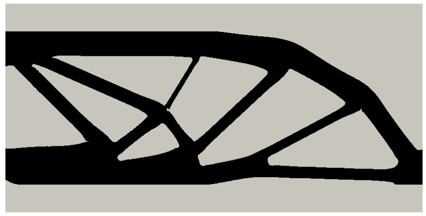

Fig. 7: Final design for MBB beam optimization with no feature size constraint ($c_{MN} = \infty$, $c_{MP} = 0$).

4.2.2 Enforcing Small Feature Size Changes

To enforce feature size we begin with an optimized design where feature size is omitted ($c_{MN} = \infty$, $c_{MP} = 0$). We take this approach to ensure that the most change in design topology is allowed before the enforcement of feature size. The design will first be optimized starting with the layout in Figure 6 ($c_{MN} = \infty$, $c_{MP} = 0$), then restarted with an additional constraint on the feature size ($c_{MN} << 1, c_{MP} = 0$).

The result of the initial optimization ($c_{MN} = \infty$, $c_{MP} = 0$) is shown in Figure 7. In addition to the thin truss-like features there are small, thin inclusions near some corners. We will now illustrate the influence of the feature size constraint on the geometry.

If we consider enforcing minimum feature sizes that are similar to the minimum feature size in Figure 7 we can restart the optimization from this design and activate the feature size constraint ($c_{MN} << 1$, $c_{MP} = 0$). We choose a feature size that is approximately one element width larger than features in the initial design, $r_x = 0.02$. Enforcing a feature size, $r_x = 0.02$, to both phases yields (7) the designs shown in Figure 8a and c. In Figure 8a the constraint is enforced strictly, setting $c_{MN} = 1 \times 10^{-4}$ while in Figure 8c it is enforced loosely with $c_{MN} = 1 \times 10^{-2}$. The resulting difference is most visible in void corners that become thin, where the angle is most acute. The beam-like structural feature that is most thin in Figure 7 is also thickened more in Figure 8a.

We also note here, as will be more obvious later, that the actual size that is visibly enforced is larger than the prescribed feature size. With closer examination, Figure 9, the resulting designs reflect a minimum feature size that is close to $(1.5 \times r_x)$. The increase in size corresponds to the smoothed Heaviside width added to the prescribed feature size. This simple relationship is an important consideration for use of this measure. Prescribing a smaller smoothed Heaviside width will allow for more exact representation of the feature size but less smooth response of the measure.

Enforcing the minimum feature size, $r_x = 0.02$ only in the solid material phase (13) results in the designs shown in Figure 8b and d, the former being a strict enforcement ($c_{MN} = 1 \times 10^{-4}$) and the latter a loose enforcement ($c_{MN} = 1 \times 10^{-2}$). In this example the differences between the two are less noticeable than in Figure 8a and c. They key difference here is that the one particularly thin

المنارة للاستشارات

www.manaraa.com

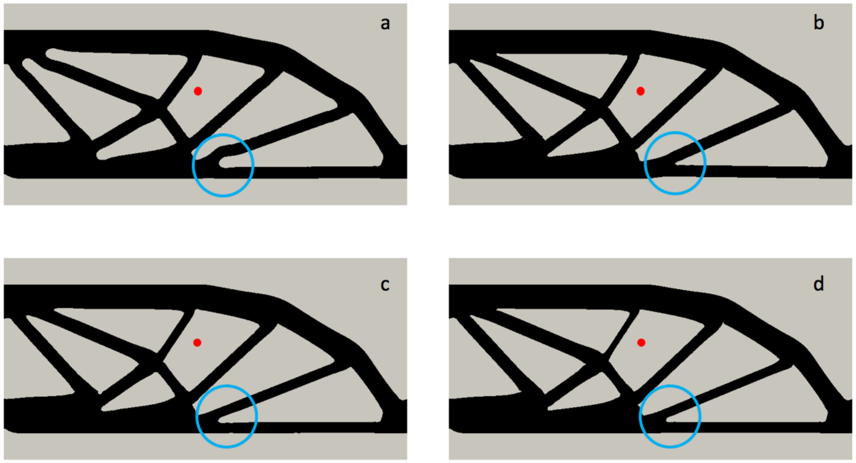

Fig. 8: Optimized designs after application of feature size constraint ($r_x = 0.02$) to (a) both phases with a strict constraint, $c_{MN} = 1 \times 10^{-4}$, (b) the solid material phase with a strict constraint, $c_{MN} = 1 \times 10^{-4}$, (c) both phases with a loose constraint $c_{MN} = 1 \times 10^{-2}$ or (d) the solid material phase with a loose constraint $c_{MN} = 1 \times 10^{-2}$. Blue circles identify regions that demonstrate differences in the designs. Red circle show the approximate size of the prescribed feature size. ($c_{MP} = 0$)

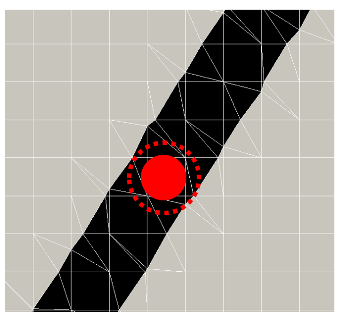

Fig. 9: Influence of smoothed Heaviside width on minimum feature size. Solid red circle radius is equal to the prescribed feature size. Dashed red circle is $1.5 \times r_x$, corresponding to sum of the effects of the feature size and the Heaviside width.

structural member from Figure 7 is more thickened in Figure 8b than Figure 8d. As shown in Table 2 we find that more strictly constrained designs have a larger strain energy than those that are loosely constrained. This holds for both allowable violation and when comparing enforcement in only a single phase to both. The unconstrained ($c_{MN} = \infty$, $c_{MP} = 0$) design appears to have stopped in a local minima that is a worse performing design than any of those found with additional feature size constraints.

المنارة للاستشارات
www.manaraa.com

Table 2: MBB Beam final strain energy values for Figures 6, 7 & 8.

	Comments	Strain Energy
Figure 6	Initial Design	2.51×10^{-2}
Figure 7	No Enforced Feature Size	7.94×10^{-3}
Figure 8a	Strictly Enforced Feature Size, Both Phases	8.01×10^{-3}
Figure 8b	Strictly Enforced Feature Size, Solid Phases	7.92×10^{-3}
Figure 8c	Weakly Enforced Feature Size, Both Phases	7.86×10^{-3}
Figure 8d	Weakly Enforced Feature Size, Solid Phases	7.85×10^{-3}

Table 3: MBB Beam final strain energy values for Figure 10, see Table 4 for more details.

	Comments	Strain Energy
Figure 10a	Step 1, No Enforced Feature Size	7.94×10^{-3}
Figure 10b	Step 2, $r_x = 0.01$ via penalty	7.87×10^{-3}
Figure 10c	Step 3, $r_x = 0.02$ via penalty	8.02×10^{-3}
Figure 10d	Step 4, $r_x = 0.03$ via penalty	9.12×10^{-3}
Figure 10e	Step 5, $r_x = 0.04$ via penalty	1.04×10^{-2}
Figure 10f	Step 6, $r_x = 0.05$ via penalty	1.20×10^{-2}
Figure 10g	Step 7, $r_x = 0.06$ via penalty	1.27×10^{-2}
Figure 10h	Step 8, $r_x = 0.06$ via constraint	1.47×10^{-2}

4.2.3 Enforcing Larger Minimum Feature Size

To enforce a larger feature size ($r_x = 0.06$) difficulties in utilizing only an inequality constraint are found. Enforcing the feature size using the strict value of allowable violation ($c_{MN} = 1 \times 10^{-4}$, $c_{MP} = 0$) results in little topology change. Allowing little topology change while substantially increasing the minimum feature size leads to poorly performing optimized designs. To overcome this we utilize a continuation approach. Increasingly larger values of feature size are enforced through a penalty over a number of steps until the prescribed value is reached ($c_{MN} = \infty$, $c_{MP} = 1$). Once the prescribed value is reached via penalty the penalty is removed and the constraint is applied to ensure strict enforcement ($c_{MN} << 1$, $c_{MP} = 0$).

Applying the continuation approach to enforce a minimum feature size in both phases results in the design sequence shown in Figure 10. In all of the designs shown it is clear that the minimum feature size is well-enforced in both phases. In Figure 10e and f all inclusions appear to be larger than the prescribed radius. The final design shown in Figure 10h depicts a problem with the approach, that is the small inclusion in the upper left corner. In this case the inclusion is largely ignored by the measure because of its small overall length and lack of closure.

المنارة للاستشارات

www.manaraa.com

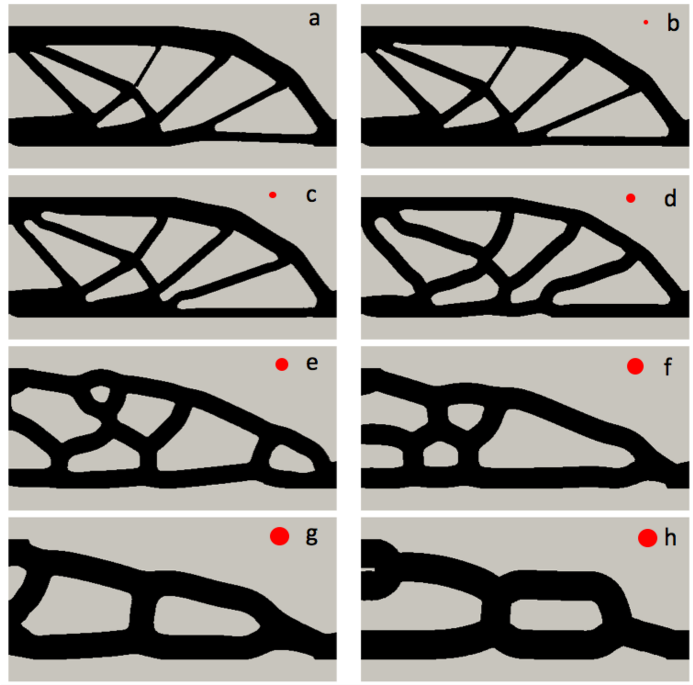

Fig. 10: Optimized designs at the end of each stage of the continuation approach described in Table 4 controlling minimum feature size in both phases. Red circles show size of prescribed minimum feature size.

For the continuation approach we find that as the minimum feature size radius increases, so does the strain energy (Table 3).

Figure 11 depicts the sequence of designs resulting from enforcement of minimum feature size in only the solid material phase. In this example we note that the inclusions are generally less smooth than those of Figure 10. The penalty on the resulting strain energy is less for all intermediate designs but the final (Table 5). It appears that the small inclusion seen in Figure 10h that is ignored by the measure is of substantial benefit to the structure. Due to the non-convex nature of the design problem, Figure 11 does not find this minima. We again note that the minimum feature size of the final design well-matches $1.5 \times r_x$ due to the width of the smoothed Heaviside function.

4.3 Force Inverter

Here we study the force inverter problem. A description of this problem can be found in Bendsøe and Sigmund (2003). The problem configuration is shown in Figure 12. The goal is to minimize the positive displacement in the x-direction at point b. We penalize the perimeter, volume fraction and feature size measure.

www.manaraa.com

Table 4: MBB beam continuation approach.

Stage	c_{MN}	c_{MP}	r_x	Number of Optimization Iterations
a	∞	0.0	0.0	500
b	∞	10.0	0.01	300
c	∞	10.0	0.02	100
d	∞	10.0	0.03	100
e	∞	10.0	0.04	100
f	∞	10.0	0.05	100
g	∞	10.0	0.06	100
h	1×10^{-4}	0.0	0.06	500

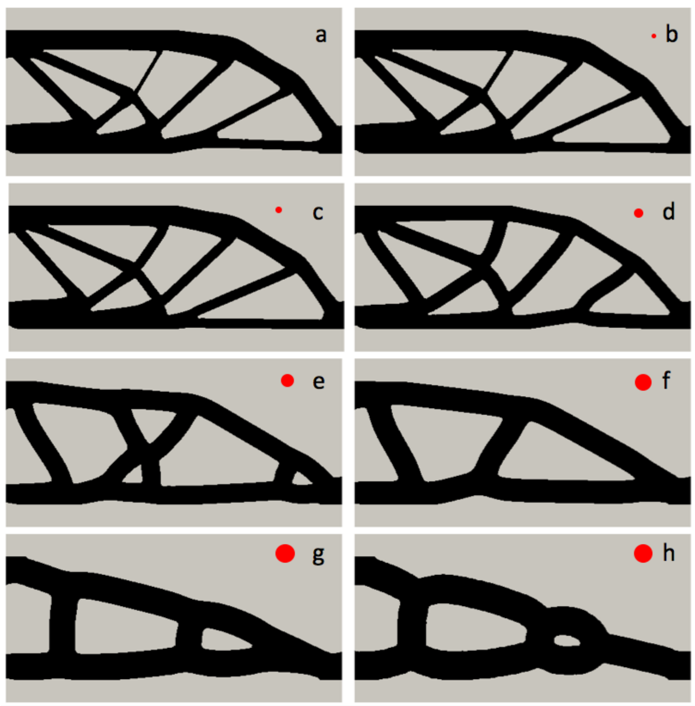

Fig. 11: Optimized designs at the end of each stage of the continuation approach described in Table 4 controlling minimum feature size in the solid material phase. Red circles show size of prescribed minimum feature size.

www.manaraa.com

Table 5: MBB Beam final strain energy values for Figure 11.

	Comments	Strain Energy
Figure 11a	Step 1, No Enforced Feature Size	7.94×10^{-3}
Figure 11b	Step 2, $r_x = 0.01$ via penalty	7.88×10^{-3}
Figure 11c	Step 3, $r_x = 0.02$ via penalty	7.93×10^{-3}
Figure 11d	Step 4, $r_x = 0.03$ via penalty	8.53×10^{-3}
Figure 11e	Step 5, $r_x = 0.04$ via penalty	9.35×10^{-3}
Figure 11f	Step 6, $r_x = 0.05$ via penalty	9.84×10^{-3}
Figure 11g	Step 7, $r_x = 0.06$ via penalty	1.22×10^{-2}
Figure 11h	Step 8, $r_x = 0.06$ via constraint	1.79×10^{-2}

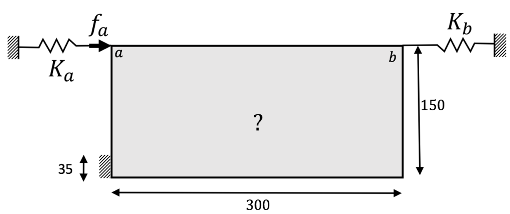

Fig. 12: Force inverter problem setup.

We introduce the volume penalty to weakly enforce a 20% volume constraint. The objective is written as:

$$Z(\mathbf{s}, \mathbf{u}) = u_b + c_{MP} M + c_{vol}\ min\left(0\ ,\ \left[\frac{V_S}{c_{vp} V_T} - 1\right]\right) + c_p P. \tag{27}$$

where we incorporate a penalty on feature size c_{MP}, perimeter c_p and on volume c_{vol}. The material parameters are presented in Table 6. The initial design, which is a series of cuboid inclusions is shown in Figure 12.

A continuation approach is used here to achieve a good design. First, a number of optimization stages are performed using a two-material problem. The void phase is modeled as a soft ($E_2 = 0.1\ E_1$) material. Once a reasonable design has been achieved with the two material configuration the soft void phase is removed. As the soft material is removed the constraint on feature size prevents the hinge from becoming overly thin and disconnecting. Here the non-normalized feature size constraint (16) is utilized. The approach discussed here is given in Table 7. The feature size that is enforced is $r_x = 5$.

The result of the continuation approach in Table 7 is shown in Figure 13. The designs at the end of each segment are shown. The first segment (a), obtains the general geometry of the design while allowing a larger amount of solid volume. Segment (b) uses a penalty to remove solid volume, driving towards the 20% value. Segment (c) introduces the feature size as a penalty and constrains the volume to

المنارة للاستشارات
www.manaraa.com

Table 6: Forcer inverter problem parameters.

Property	Value
Material Stiffness	$E_1 = 180 \times 10^3$
Void Material Stiffness	$E_2 = 180 \times 10^2$
Poisson Ratio	$\nu = 0.3$
Input load	$f_a = 1.45 \times 10^5$
Input Spring Stiffness	$K_a = 4000$
Output Spring Stiffness	$K_b = 1000$
Final Allowable Volume Fraction	$c_v = 0.2$

Table 7: Forcer inverter problem continuation approach.

Step	Perimeter Penalty c_p	Optimization Iterations	Volume Penalty c_{vol}	Feature Size Penalty c_{MP}	Feature Size Constraint c_M	Constrained Volume c_v	Penalized Volume c_{vp}	Soft or Void Second Phase
a	500	1×10^{-4}	0	0	∞	0.4	0.2	Soft
b	200	1×10^{-4}	100	0	∞	0.4	0.2	Soft
c	100	1×10^{-4}	0	1	∞	0.2	0.2	Soft
d	35	0	0	0	∞	0.2	0.2	Soft
e	100	1×10^{-4}	0	0	50.0	0.2	0.2	Soft
f	200	1×10^{-4}	0	0	50.0	0.2	0.2	Void

20%. Segment (d) relaxes the feature size and perimeter penalties in an effort to remove extraneous material. Segment (e) introduces the feature size enforcement via constraint so that the soft material can then be removed in segment (f). The enforcement of feature size allows for the retention of the hinge even when the optimizer drives towards removing it. The side affect of this strict enforcement is that extraneous feature may be retained and require care to remove.

4.4 Convective Design

4.4.1 Setup

To study the feature size measure for another physical problem, we take the heat conduction problem with edge convection of Coffin and Maute (2015). The objective of this problem is to minimize the temperature where heat is applied by arranging a limited amount of diffusive material. The in-plane boundaries of the diffusive material are subject to a simplified convection boundary condition. This

www.manaraa.com

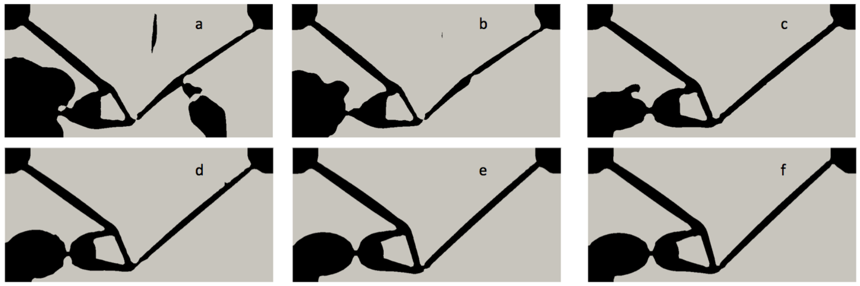

Fig. 13: Force inverter design progression. See Table 7 for details.

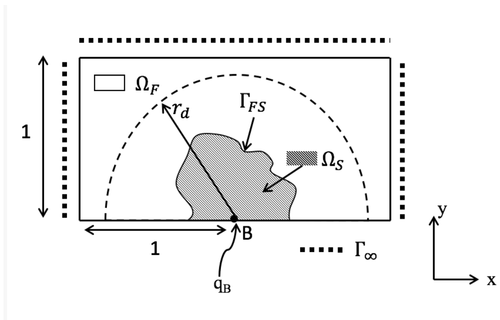

Fig. 14: Convective design problem setup.

class of problems leads very thin solid and void features that can hamper design convergence.

The problem setup is shown in Figure 14. A heat flux q_B is applied at point B and at the far field, Γ_∞, the temperature is fixed, $T_F = T_\infty$. The objective Z is written as:

$$Z\left(\mathbf{s},\mathbf{u}\right) = T_B. \tag{28}$$

In a classical Newton's Law of Cooling formulation a single diffusive material would be used. The temperature in the fluid (or void) domain would be prescribed to be the far-field temperature. To deter the formation of disconnected fluid inclusions we utilize two diffusive materials, one for the solid and one for a fictitious fluid. The conductivity in the fictitious fluid is set to be large relative to the solid $\kappa_F >> \kappa_S$ so that on the fluid-solid interface the temperature is nearly the far-field value $T_F \approx T_\infty$. The residual form of the governing equations (Coffin and Maute, 2015) is written as:

$$\begin{aligned}\tilde{R}_T = &\int_{\tilde{\Omega}_S} \frac{\partial \delta \tilde{T}_S}{\partial \tilde{x}_i}\ \delta_{ij}\ \frac{\partial \tilde{T}_S}{\partial \tilde{x}_j}\ d\Omega + \int_{\tilde{\Omega}_F} \frac{\partial \delta \tilde{T}_F}{\partial \tilde{x}_i}\ \frac{\kappa_F}{\kappa_S}\delta_{ij}\ \frac{\partial \tilde{T}_F}{\partial \tilde{x}_j}\ d\Omega \\ &- \int_{\tilde{\Gamma}_q} \delta \tilde{T}_S \frac{L_C q_q}{\kappa_S T_{ref}}\ d\Gamma - \int_{\tilde{\Gamma}_{FS}} \delta \tilde{T}_F\ \frac{h L_c}{\kappa_S}\left(\tilde{T}_S - \tilde{T}_F\right)\ d\Gamma = 0,\end{aligned} \tag{29}$$

المنارة للاستشارات
www.manaraa.com

Table 8: Convective design problem parameters.

Property	Value
Applied Heat	$q_B = 1.0$
Solid Diffusivity	$\kappa_S = 1.0$
Fluid Diffusivity	$\kappa_F = 5.0$
Convection Coefficient	$h = 0.1$
Characteristic Length	$L_C = 1.0$
Far Field Temperature	$T_\infty = 0.0$
Reference Temperature	$T_{ref} = 0.0$

Table 9: MBB beam configuration parameters.

	Value
Elements	100×50
Filter Radius	$r_f = 0.048$
Number of design variables	$N_S = 2601$
Lower Bound	$s^L = -0.02$
Upper Bound	$s^U = 0.02$
Level Set Scaling	$l_\phi = 1.0$
Outer Design Radius	$r_d = 0.8$

where $\tilde{T}_S$ and $\tilde{T}_F$ are the non-dimensional solid and fluid temperatures. The solid and fluid diffusivities are κ_S and κ_F, h the convection coefficient, L_C the characteristic length and q_q the boundary heat flux. The material properties are described in Table 8.

The optimization parameters are given in Table 9. In this problem the design is prescribed to be symmetric, that is that design variables are only defined on nodes in the left half of the mesh. Level set values at nodes on the right half of the mesh are set equal to those on the left. An outer design radius is also specified, r_d, beyond which the design variables are set equal to the upper bound.

4.4.2 Results

To simplify the initial design of the convective problem we choose a semi-circle, $r = 0.5$; see Figure 15. As observed in previous studies (Coffin and Maute, 2015; Bruns, 2007), the design is expected to grow branches out from the initial circle. While the geometry changes are radical there is little change in topology. This particular evolution of geometry in the design process ensures that for all values of minimum feature size less than the initial circle radius, there will be no initial violation of the feature size constraint. With no continuation approach the constraint can be

www.manaraa.com

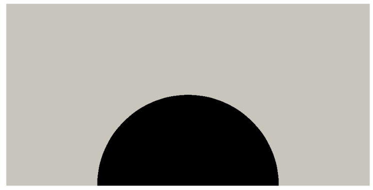

Fig. 15: Initial design for convective design problem.

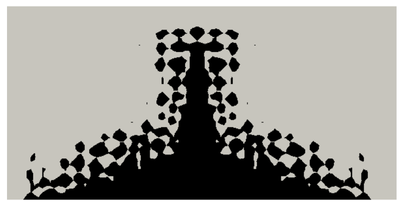

Fig. 16: Convective design resulting from no feature size enforcement ($c_{MN} = \infty$).

enforced strictly, $c_{MN} = 1 \times 10^{-4}$. Table 10 shows the final objective temperatures from the examples in this section.

Figure 16 shows the result of not enforcing any minimum feature size. This optimization does not yield a converged design. Branches are formed from the circular base, their connection to the base grows thin and eventually they disconnect and are removed from the design. After the branches disconnect from the base, new branches form. Without additional regularization this leads to a continuous morphing of the geometry. More details on this issue and the need for regularization is provided in Coffin and Maute (2015).

Optimizing for a selection of minimum feature sizes a series of complicated geometric structures emerge; see Figure 17. The nature of the design problem leads to these complicated shapes. This design problem is also strongly non-convex.

This design problem drives to increasing surface area and wavy boundaries (Figure 17) making it a good example for demonstrating the influence of r_{tx}. The parameter r_{tx} is an important scaling in (7) and (13). It determines regions of nearby points that are excluded as their interface distance is small relative to their Euclidean distance. Selecting the configuration of Figure 17c, the scaling is varied and the resulting designs are shown in Figure 18. Note: Figure 17c and 18c are identical. For small values of scaling, $r_{tx} < 1.2$ little feature development occurs because the measure identifies nearly all curvature as violations. As values of the scaling increase, more features and oscillations are allowed. The choice of $r_{tx} = 2/\sqrt{2}$ (Figure 18c) allows a visually appealing degree of feature development while $r_{tx} = 1.2$ (Figure 18b) may be a good choice to promote smooth designs.

5 Conclusions

This paper presented a novel measure to identify and control minimum feature size in Level Set (LS) eXtended Finite Element Method (XFEM) topology optimiza-

المنارة للاستشارات
www.manaraa.com

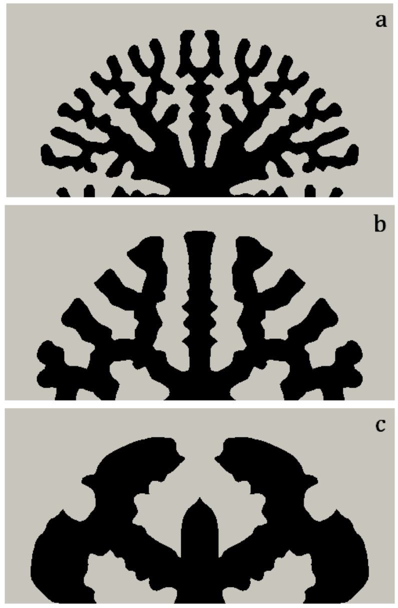

Fig. 17: Final convective designs with varying minimum feature size: a, $r_x = 0.04$; b, $r_x = 0.08$; c, $r_x = 0.16$.

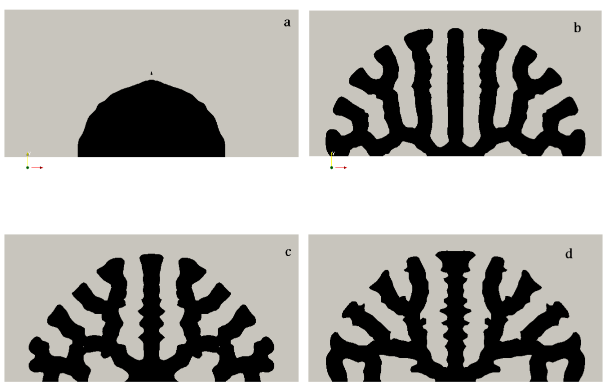

Fig. 18: Final convective designs with varying exclude ratio, r_{tx}, minimum feature size, $r_x = 0.08$: a, $r_{tx} = 1.0$; b, $r_{tx} = 1.2$; c, $r_{tx} = 2/\sqrt{2}$; d, $r_{tx} = 1.9$.

www.manaraa.com

Table 10: Convective design objective temperatures.

	Temperature at B
Figure 15	8.14
Figure 17a	2.67
Figure 17b	3.40
Figure 17c	4.14
Figure 18a	8.00
Figure 18b	3.30
Figure 18c	3.40
Figure 18d	3.20

tion. The scalar measure identified features using the discretized surface geometry of the XFEM model. This differentiates it from existing methods that directly utilize the LSF. The measure differs from the quadratic energy approach in that it does not use surface tangent information. This allows it to permit sharp corners found on a discretized surface.

The measure was demonstrated via numerical experiments using three design problems: the MBB beam, force inverter and a heat transfer device with edge convection. The measure was incorporated both as a constraint and as a penalty. In cases where the feature size could be enforced strictly the constraint was used. In cases where a strict enforcement overly restricted design changes the measure was enforced with the penalty.

The measure was shown to be effective in identifying and enforcing a minimum feature size when utilized as an inequality constraint. In application to the MBB beam it was shown that the minimum feature size can be strongly enforced in either a single material phase or both. Used as a constraint, enforcing a minimum feature size much larger than the current geometry can be problematic. For larger changes it is necessary to use a continuation approach, using a penalty to enforce increasingly large feature sizes.

The forcer inverter required a careful continuation approach to ensure that extraneous geometric features were removed while not disconnecting the hinge. Once a good initial design was achieved via a two material problem fine tuning could be performed in the solid-void configuration. The enforcement of the minimum feature size enabled this fine tuning to occur, preventing the hinge from disconnecting.

Application of the measure to the convective design problem was shown to be simpler due to the simple initial design. The use of a simple initial design also ensured that the constraint was satisfied initially. The scaling of the feature sensing within the measure was also explored with the problem and a range of baseline values were found.

The key conclusions drawn from this study are summarized as: The measure as presented allows flexible and strict enforcement of a minimum feature size. The construction makes deterring the formation of small features convenient. Removing

المنارة للاستشارات

www.manaraa.com

existing small features requires more care. Incorporation of the measure into an inequality constraint also allows for strict enforcement but is a difficult approach when initial designs violate the constraint. Finally, the parameter of the measure allows for some control over surface roughness-like features.

This measure provides a robust tool for identifying violations of a minimum feature size to the designer using LS-XFEM topology optimization. The measure also allows some control over surface roughness or curvature via its scaling parameter. It requires care to use the measure to produce large changes in feature size however. It also, by construction can be difficult to develop a continuation approach to allow feature development and topology change while enforcing a minimum feature size on the final design. Future work is necessary to develop robust continuation schemes or formulations to balance feature development and minimum feature size constraint.

Acknowledgements The authors acknowledge the support of the National Science Foundation under grant EFRI-ODISSEI 1240374 and CBET 1246854. The opinions and conclusions presented in this paper are those of the authors and do not necessarily reflect the views of the sponsoring organization.

References

Allaire G, Jouve F, Toader AM (2004) Structural optimization using sensitivity analysis and a level-set method. Journal of Computational Physics 194(1):363–393

Allaire G, Jouve F, Michailidis G (2014) Thickness control in structural optimization via a level set method, URL https://hal.archives-ouvertes.fr/hal-00985000

Bendsøe MP, Sigmund O (2003) Topology Optimization: Theory, Methods and Applications. Springer

Bruns T (2007) Topology optimization of convection-dominated, steady-state heat transfer problems. International Journal of Heat and Mass Transfer 50(15-16):2859 – 2873

Chahine E, Laborde P, Renard Y (2008) Crack tip enrichment in the xfem using a cutoff function. International Journal for Numerical Methods in Engineering 75(6):629–646, URL http://dx.doi.org/10.1002/nme.2265

Chen S, Wang M, Liu A (2008) Shape feature control in structural topology optimization. Computer-Aided Design 40(9):951–962

Coffin P, Maute K (2015) Level set topology optimization of cooling and heating devices using a simplified convection model. Structural and Multidisciplinary Optimization

van Dijk N, Maute K, Langelaar M, Keulen F (2013) Level-set methods for structural topology optimization: a review. Structural and Multidisciplinary Optimization 48(3):437–472

Fries T, Belytschko T (2010) The extended/generalized finite element method: an overview of the method and its applications. International Journal for Numerical Methods in Engineering 84(3):253–304

Gerstenberger A, Wall WA (2008) Enhancement of fixed-grid methods towards complex fluid-structure interaction applications. Int J Numer Meth Fluids 57(9):1227–1248

المنارة للاستشارات

www.manaraa.com

Gomes A, Suleman A (2006) Application of spectral level set methodology in topology optimization. Structural and Multidisciplinary Optimization 31(6):430–443

Guest J, Prévost J, Belytschko T (2004) Achieving minimum length scale in topology optimization using nodal design variables and projection functions. International Journal for Numerical Methods in Engineering 61(2):238–254

Guo X, Zhang W, Zhong W (2014) Explicit feature control in structural topology optimization via level set method. Computer Methods in Applied Mechanics and Engineering 272:354–378

Jenkins N, Maute K (2015) Level set topology optimization of stationary fluid-structure interaction problems. Structural and Multidisciplinary Optimization 52(1):179–195

Kreissl S, Maute K (2012) Levelset based fluid topology optimization using the extended finite element method. Structural and Multidisciplinary Optimization 46(3):311–326

Kreissl S, Pingen G, Maute K (2011) An explicit level set approach for generalized shape optimization of fluids with the lattice boltzmann method. International Journal for Numerical Methods in Fluids 65(5):496–519

Lang C, Makhija D, Doostan A, Maute K (2014) A simple and efficient preconditioning scheme for heaviside enriched XFEM. Computational Mechanics 54(5):1357–1374

Liu J, Ma Y, Fu J, Duke K (2015) A novel cacd/cad/cae integrated design framework for fiber-reinforced plastic parts. Advances in Engineering Software 87:13 – 29

Luo J, Luo Z, Chen S, Tong L, Wang M (2008) A new level set method for systematic design of hinge-free compliant mechanisms. Computer Methods in Applied Mechanics and Engineering 198(2):318–331

Makhija D, Maute K (2014) Numerical instabilities in level set topology optimization with the extended finite element method. Structural and Multidisciplinary Optimization 49(2):185–197

Michell AGM (1904) The limits of economy of material in frame-structures. Philos Magazine S6 8(47):589–597

Poulsen TA (2003) A new scheme for imposing a minimum length scale in topology optimization. International Journal for Numerical Methods in Engineering 57(6):741–760

Schevenels M, Lazarov BS, Sigmund O (2011) Robust topology optimization accounting for spatially varying manufacturing errors. Computer Methods in Applied Mechanics and Engineering 200(49):3613–3627

Sigmund O (2009) Manufacturing tolerant topology optimization. Acta Mechanica Sinica/Lixue Xuebao 25(2):227–239

Svanberg K (2002) A class of globally convergent optimization methods based on conservative convex separable approximations. SIAM J on Optimization 12(2):555–573

Terada K, Asai M, Yamagishi M (2003) Finite cover method for linear and nonlinear analyses of heterogeneous solids. International Journal for Numerical Methods in Engineering 58(9):1321–1346

Tran AB, Yvonnet J, He QC, Toulemonde C, Sanahuja J (2011) A multiple level set approach to prevent numerical artefacts in complex microstructures with nearby inclusions within xfem. International Journal for Numerical Methods in Engineering 85(11):1436–1459

المنارة للاستشارات
www.manaraa.com

Villanueva CH, Maute K (2014) Density and level set-xfem schemes for topology optimization of 3-d structures. arXiv preprint arXiv:14016475

Xia Q, Shi T (2015) Constraints of distance from boundary to skeleton: For the control of length scale in level set based structural topology optimization. Computer Methods in Applied Mechanics and Engineering 295:525–542

Zhang W, Zhong W, Guo X (2014) An explicit length scale control approach in simp-based topology optimization. Computer Methods in Applied Mechanics and Engineering 282:71 – 86

Zhou M, Lazarov BS, Sigmund O (2014) Topology optimization for optical projection lithography with manufacturing uncertainties. Appl Opt 53(12):2720–2729

Zhou M, Lazarov BS, Wang F, Sigmund O (2015) Minimum length scale in topology optimization by geometric constraints. Computer Methods in Applied Mechanics and Engineering 293:266–282

المنارة للاستشارات

www.manaraa.com